Cerenkov emission in radiotherapy

By

Yusuf Helo

A THESIS SUBMITTED TO THE UNIVERSITY OF LONDON
FOR THE DEGREE OF DOCTOR OF PHILOSOPHY

DEPARTMENT OF MEDICAL PHYSICS AND BIOMEDICAL ENGINEERING
UNIVERSITY COLLEGE LONDON

2015

Declaration

I, Yusuf Helo confirm that the work presented in this thesis is my own. Where information has been derived from other sources, I confirm that this has been indicated in the thesis.

Yusuf Helo

Abstract

A new potential quality assurance (QA) method is explored for clinical electron beams and clinical proton beams based on imaging and measuring Cerenkov light.

A simulation was performed of the deposited energy and of Cerenkov production in water using Geant4. Monte Carlo simulation was used to predict the measured light distribution around the water phantom, to reproduce Cerenkov images and to find the relation between deposited energy and Cerenkov production. The camera was modelled as a pinhole camera in Geant4, to attempt to reproduce Cerenkov images.

The potential of using a standard commercial camera to image Cerenkov light generated from electrons in water for fast QA measurement of a clinical electron beam was explored and compared to ionization chamber measurements. The new method was found to be linear with dose and independent of dose rate (to within 3%). The uncorrected practical range measured using Cerenkov images was found to overestimate the actual value by 3 mm in the worst case. The field size measurements underestimated the field sizes at the edges by 5% without applying any correction factor. Still, the measured field size could be used to monitor relative changes in the beam profile. Finally, the beam-direction profile measurements were independent of the field size within 2%.

We found that imaging Cerenkov emission from a breast phantom during electron irradiation could be a suitable tool to monitor the dose and the dose rate consistency with high precision and short-term repeatability better than 3% except when measuring very low doses. Cerenkov light measurements were linear with dose and independent of dose rate. The maximum light intensity occurred at an angle of 45.0°. We were unable to identify the regions of the phantom with higher scattering and absorption properties, designed to mimic diseased tissues using images of Cerenkov emission of an optical breast phantom.

We found that the Cerenkov light emissions in proton therapy can be divided into two

distinct mechanisms: a fast component due to prompt gamma interactions (99.13%) and neutron interactions (0.87%), and a slow component due to radioactive decay. The simulated depth distribution of the Cerenkov emission shows a strong relation with the depth distribution of the induced radioactive isotopes, which emit positrons. The fast component was found to be linear with dose and independent of dose rate, while the slow component increases non- linearly with dose and is highly dependent on dose rate.

Imaging Cerenkov light during electron radiotherapy or proton therapy could be used as a very quick routine QA tool.

Novel Work Undertaken

The potential of using a standard commercial camera to image Cerenkov light generated from electrons in water for fast QA measurement of a clinical electron beam was explored for the first time. During the preparations of this work, Zhang et al (2013) imaged Cerenkov emission from the surface of a flat tissue phantom and compared it with the estimated superficial dose deposited by electron beam in that phantom measured by diode. They tested the dose linearity of Cerenkov measurement along with the crossbeam profile, while in our study we extend their work to include the dose rate dependence, the field size dependence and the depth profile of Cerenkov images for the first time. My results were presented in the IOP conference 'Novel methods for the detection of nuclear and radioactive materials, 2012', and published in Physics in Medicine and Biology in 2014 (Helo et al., 2014d).

Eye cancer patients frequently report seeing flashes of light during proton therapy (Khan et al., 2010; Newman et al., 2008). Despite the fact that Cerenkov light production is known to occur during conventional radiotherapy (Helo et al., 2014d; Newman et al., 2008), little work has been done to verify and quantify Cerenkov production in proton therapy and to determine whether it is responsible for creating the light sensation seen by some patients. The potential of using Cerenkov emissions in proton therapy for dosimetry was explored for the first time. My results were presented in the NPL workshop "Proton physics research and implementation group, 2014", and presented in the Biomedical Optics conference (Florida 2014) (Helo et al., 2014e). A paper on this work was accepted for publication in the physics in medicine and biology (Helo et al., 2014a).

Acknowledgments

I would like to thank my wife and daughter in United Kingdom and my family in Syria for unlimited support and love.

I would like to thank University College London Hospitals for their support and for letting us using their facility, especially Prof Ivan Rosenberg for his assistance and guidance.

I would like to thank the staff of the Douglas Cyclotron at the Clatterbridge Cancer Centre, for their support and use of their facility.

Last but not least, I would like to deeply thank all my colleagues in medical physics department and my supervisors Dr Adam Gibson and Prof Gary Royle.

Symbols and abbreviations

n	refractive index
c	speed of light in vacuum(2.9979 x 10^8 m/sec)
v	particle velocity
β	relative velocity ($\frac{c}{v}$)
t	time
Z	atomic number or nuclear charge
ε_0	permittivity of free space
e^-	electron
e^+	positron
ħ	Planck's constant/2 π ($1.0551 \times 10^{-34}\ m^2\ kg\ /\ s$)
α	fine structure constant ($\frac{1}{137} = 7.29735257 \times 10^{-3}$)
m_0	particle rest mass
E_{th}	threshold energy
E_{max}	maximum energy
E_{min}	minimum energy
λ	wavelength, decay constant
γ	gamma radiation
μ	linear attenuation coefficient
μ_m	mass attenuation coefficient
β^+	beta plus decay
β^-	beta minus decay
x-axis	the horizontal axis of a system of coordinates
z-axis	the third axis in a 3-D coordinate system

cm	centimetre (10^{-2} m)
mm	millimetre (10^{-3} m)
b	barn (10^{-24} cm^2)
J	joule
eV	electron volt (1.602 x 10^{-19} J)
MeV	mega electron volts (10^6 eV)
Gy	gray (J/kg)
s	seconds
ms	millisecond
ns	nanosecond

R_p	practical range for electron and proton
d_{max}	depth of maximum dose
R_{90}	depth of 90% dose
R_{50}	depth of 50% dose
PDD	Percentage Depth Dose
SSD	Source Surface Distance
SCD	Source Chamber Distance
$TPR_{20,10}$	Tissue phantom Ratio in water at depths of 20 and 10 cm
MU	Monitor Unit
QA	Quality Assurance
CLT	Cerenkov Luminescence Tomography
SOBP	Spread Out Bragg Peak
FWHM	Full Width at Half Maximum
MC	Monte Carlo
VMAT	Volumetric Modulated Arc Therapy
IMRT	Intensity Modulated Radiation Therapy

PET	Positron emission Tomography
IAEA	International Atomic Energy Agency, Vienna
ICRU	International Commission on Radiation Units and Measurements
ENDF	Evaluated Nuclear Data File
UCLH	University College London Hospital
PMB	Physics in Medicine and Biology

Contents

Declaration 2

Abstract 3

Novel Work Undertaken 5

Acknowledgments 6

Symbols and abbreviations 7

Contents 10

Chapter 1 14

BACKGROUND AND THEORETICAL APPROCH 14

1.1 Historical 14
1.2 Cerenkov radiation 14
1.2.1 Classical theory of Frank and Tamm 17
1.2.2 Radiation yield and spectral distribution 18
1.2.3 Duration of Cerenkov light flash 20
1.2.4 Charged particles and Cerenkov emissions 20
1.2.4.1 Cerenkov radiation from protons 21
1.2.5 Uncharged particles and Cerenkov emissions 23
1.2.5.1 Cerenkov radiation from gamma photon 23
1.2.5.2 Cerenkov radiation from neutrons 26
1.3 Radiotherapy 27
1.3.1 Dose distribution and quality assurance 28
1.3.1.1 Central axis depth dose distributions 28
1.3.1.2 Cross axis dose distributions 29
1.3.1.3 Film 30
1.3.1.4 Gel 31
1.3.1.5 Thermoluminescent dosimeter (TLD) 31
1.3.1.6 Modern dosimeters 31
1.4 Proton therapy 32
1.4.1 Dose distribution and quality assurance 33
1.4.1.1 Central axis depth dose distributions 34
1.4.1.2 Lateral depth dose distributions 35
1.4.1.3 Positron emission tomography (PET) 36
1.4.1.4 Proton therapy and eye cancer 39
1.5 Cerenkov emission in radiotherapy 40
1.5.1 Cerenkov luminescence tomography 40
1.5.2 Cerenkov fibre dosimetry 41
1.5.3 Tissue oxygenation and Cerenkov emissions 41
1.5.4 Imaging Cerenkov emission during radiotherapy 42
1.6 Light emissions seen by patients during radiotherapy 42
1.7 The objectives of the work 43

Chapter 2 45

MONTE CARLO SIMULATION 45

2.1 Background 45

2.2 Electron beam simulation 47

2.2.1 Monte Carlo code validation 47

2.2.1.1 Depth dose distribution and cross beam profile simulations 47

2.2.1.2 Justification of the customised energy spectra 52

2.2.1.3 Cerenkov implementation verification 54

2.2.2 Secondary emission in electron therapy and Cerenkov emission 55

2.2.3 Cerenkov light distribution 57

2.2.4 Cerenkov production profile 58

2.2.5 An investigation of the discrepancy between the simulated Cerenkov profiles and depth dose profiles found in Figures 2.11 and 2.12 60

2.2.6 Pinhole code 63

2.2.6.1 Magnification effect simulation 66

2.3 Proton beam simulation 68

2.3.1 Monte Carlo code validation 69

2.3.1.1 Pristine Bragg peak and spread out Bragg peak (SOBP) simulations 69

2.3.1.2 Lateral profile simulation 72

2.3.1.3 Nuclear cross-section verification 73

2.3.1.4 Radioactivity implementation 74

2.3.2 The secondary emissions in proton therapy 75

2.3.2.1 Secondary proton spectrum 75

2.3.2.2 Secondary electron spectrum 76

2.3.2.3 Secondary gamma emission spectrum 77

2.3.2.4 Secondary neutron emission spectrum 78

2.3.2.5 Radioactivity and secondary positron spectrum 79

2.3.3 Cerenkov light distribution 80

2.3.4 Cerenkov production profile 82

2.3.4.1 Cerenkov production in the fast component 82

2.3.4.2 Cerenkov production in the slow component 83

2.3.5 Linearity between Cerenkov emissions and dose or dose rate 85

2.3.5.1 Fast component 85

2.3.5.2 Slow component 86

2.3.6 Eyeball and retina simulation 87

2.3.6.1 The total number of photons generated in the human eye by the fast and slow components of Cerenkov production 88

Chapter 3 89

EXPERIMENTAL RESULTS AND DISCUSSION 89

3.1 Imaging Cerenkov emission as a quality assurance tool in electron radiotherapy 89

3.1.1 Objectives 89

3.1.2 Materials and methods 89

3.1.2.1 Dose linearity 91

3.1.2.2 Dose rate dependence 91

3.1.2.3 Beam-direction profiles and electron range measurements 92

3.1.2.4 Field size 92

3.1.2.5 Field size dependence 93

3.1.2.6 Field depth and vignetting problem 93
3.1.3 Results and discussion 94
3.1.3.1 Linearity between Cerenkov measurements and dose 94
3.1.3.2 Dependence of Cerenkov measurements on dose rate 95
3.1.3.3 Range measurements 96
3.1.3.4 Field size 97
3.1.3.5 Field dependence 98
3.2 Imaging Cerenkov emission in a conical phantom with tissue-equivalent optical properties 99
3.2.1 Objective 99
3.2.2 Material and methods 100
3.2.2.1 Dose linearity 101
3.2.2.2 Dose rate dependence 102
3.2.2.3 Beam-direction profiles 102
3.2.2.4 Angular dependence 102
3.2.2.5 Imaging phantom with different optical properties 102
3.2.3 Results and discussion 103
3.2.3.1 Linearity between Cerenkov measurements and dose 103
3.2.3.2 Dependence of Cerenkov measurements on dose rate 103
3.2.3.3 Beam-direction profiles 104
3.2.3.4 Angular dependence 105
3.2.3.5 Imaging phantom with different optical properties 106
3.3 Cerenkov light production during proton therapy 107
3.3.1 Objectives 107
3.3.2 Material and methods 107
3.3.2.1 Time scale of slow component 108
3.3.2.2 Dose linearity 108
3.3.2.3 Dose rate dependence 109
3.3.3 Results and discussion 109
3.3.3.1 Time scale of slow component 109
3.3.3.2 Linearity between Cerenkov measurements and dose 110
3.3.3.3 Dependence of Cerenkov measurements on dose rate 111

Chapter 4 114

CONCLUSION 114

4.1 Imaging Cerenkov emission as a quality assurance tool in electron radiotherapy 114
4.2 Imaging Cerenkov emission in conical phantom with tissue-equivalent optical properties
4.3 Cerenkov light production during proton therapy and its potential application as a quality assurance tool 115
4.3.1 Potential applications 116
4.3.1.1 Quality assurance 116
4.3.1.2 Treatment verifications 116

Appendices 118

Appendix 1: Maximum energy lost by protons in Coulomb interactions 118
Appendix 2: β^+ decay 120
Appendix 3: Radiation damage in CCD camera 122

References 123

This Page Intentionally Left Blank.

Chapter 1

BACKGROUND AND THEORETICAL APPROCH

1.1 Historical

Many workers in the field of radioactivity had observed a bluish-white light from transparent materials placed close to strong radioactive sources, without understanding of its origin. Cerenkov, a Russian scientist, was the first to conduct a series of experiments to explain the origin of the light and his results agreed with Frank and Tamm's theory (Jelley, 1958) which was proposed at the same time. Then in 1940 Ginsburg developed a quantum theory of the phenomenon, which was known ever since as Cerenkov radiation (Jelley, 1958).

Radiotherapy has been used for more than 100 years in treating cancer patients particularly since Nobel Prize winning Marie Curie discovered radium, which was used to treat patients. In the middle of the twentieth century, cobalt and caesium units replaced radium for medical purposes. Three-dimensional (3D) planning became available in the 1970s, which eventually transferred radiation delivery from 2D to 3D. The invention of new technology like magnetic resonance imaging (MRI), positron emission tomography, multi-leaf collimation (MLC) and portal imaging has shifted some of the 3D conformal radiation therapy to intensity modulated radiation therapy (IMRT), which has resulted in enhanced treatment outcomes and fewer side effects (Boggula et al., 2010; Lederman, 1981).

Recently, proton therapy has been used to treat some types of cancer. Proton therapy allows more precise delivery of dose to the tumour while avoiding or reducing dose to the surrounding tissue due to the sharp distal fall-off in dose at the Bragg peak (Brada et al., 2007; Levin et al., 2005). The treatment of eye cancer is a particular example of the superiority of proton therapy above other types of radiotherapy (Bonnett et al., 1993; Kacperek, 2009).

1.2 Cerenkov radiation

Consider a charged particle moving fast through a transparent medium. The electric field of the particle distorts the atoms so that the medium becomes polarized along the axis of the particle

track, each resultant dipole will then radiate a brief electromagnetic pulse. The radiation will range over a band of frequencies corresponding to the various Fourier components of this pulse. In general, the radiated wavelets from all parts of the track interfere destructively so that the resultant intensity is zero. If the velocity of the particle is higher than the phase velocity of the light in the medium, it is possible for the wavelets from all portions of the track to be in phase so there will be a resultant field (Green, 2000; Jelley, 1958). The phase velocity of a wave is the speed of a single frequency component of the wave propagates through space, while the group velocity of a wave is the speed at which the pulse of light, or the envelope of the wave, propagates through space. The phase velocity cannot carry any information while the group velocity is used in communications (L'Annunziata, 2012).

Cerenkov photons are released on the surface of a cone, whose opening angle with respect to the particle direction decreases as the particle slows down. Simultaneously, the frequency of the photons emitted increases, and the number of produced photons drops. Cerenkov emission is decreased and the cone angle drops to zero when the particle velocity declines below the local speed of light. Cerenkov photon has inherent polarization perpendicular to the cone's surface at production (Green, 2000; Jelley, 1958).

If a particle traverses across a track AR in the same time that the light travels from A to B as shown in Figure 1.1, the angle θ between the particle track and the light track could be easily calculated as shown in equations 1.1 and 1.2,

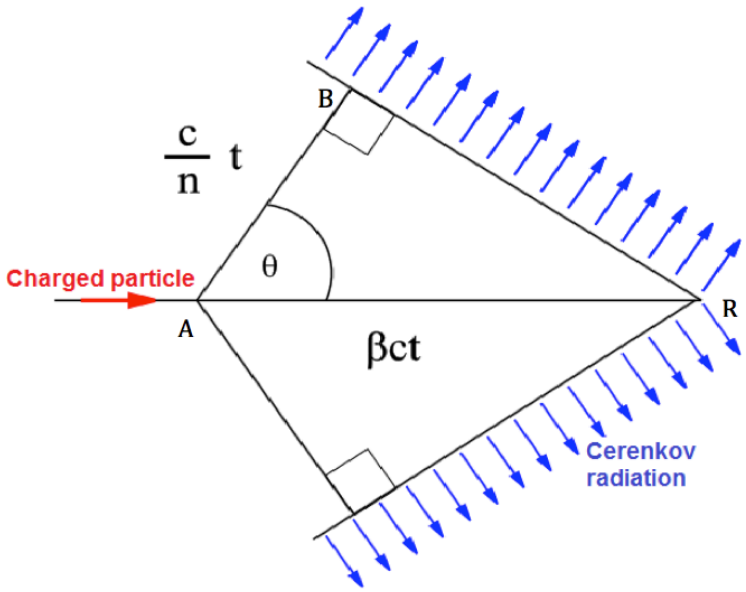

Figure 1.1 Cerenkov emission of a charged particle travel inside a medium at an angle θ.

$$\cos\theta = \frac{v.t}{\beta.c.t} \qquad (1.1)$$

$$\cos\theta = \frac{1}{\beta n} \qquad (1.2)$$

where,

n : Refractive index of the medium (the refractive index measures the phase velocity of light).

β : The ratio of the particle velocity in the medium (v) to the velocity of light in a vacuum (c). ($\beta = \frac{v}{c}$).

c : The velocity of light in a vacuum.

When the velocity of the particle is $\beta_{min} = \frac{1}{n}$, where β and n are as defined in equation 1.2, the direction of the radiation coincides with that of the particle. Below β_{min}, there will be no Cerenkov production. The maximum angle of emission occurs when $\beta = 1$ (for electron travels in water as an example, the maximum angle of emission occurs at 41.4° (Axelsson et al., 2011). In theory the Cerenkov radiation wavelength range is infinite (Jelley, 1958), but in practice the measureable Cerenkov emission happens mainly in the visible and near-visible regions of the spectrum because

of the absorption bands of the transparent material (see Figure 1.2). In the x-ray region the refractive index (n) is always less than 1 therefore Cerenkov radiation is forbidden (Jelley, 1958). Figure 1.2 shows the theoretical Cerenkov light spectrum with and without the absorption effect of 25 cm of water.

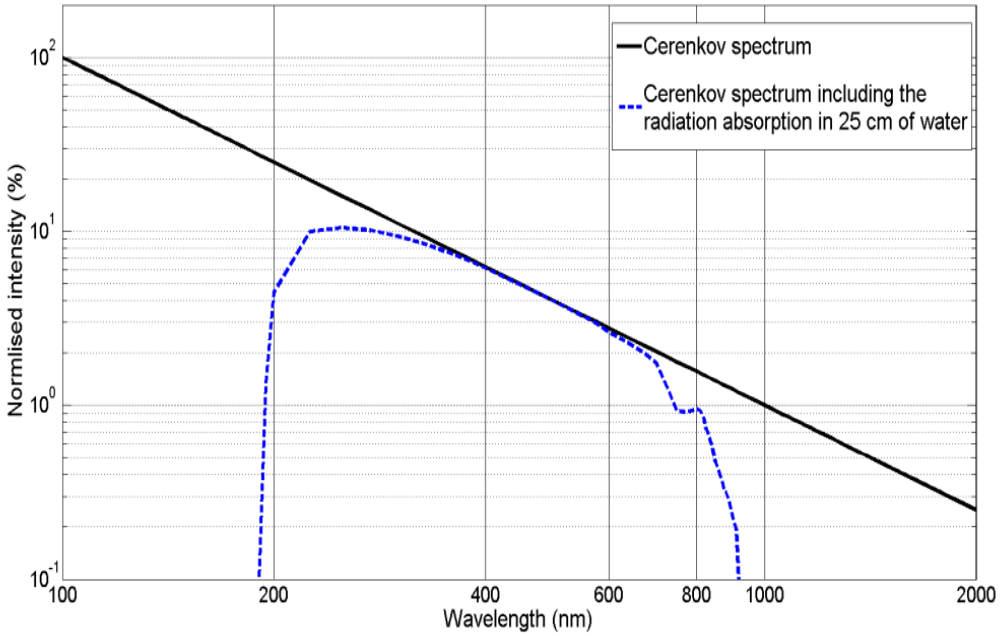

Figure 1.2 Theoretical Cerenkov light spectrum considering the absorption effect of 25 cm of water. Drawn using the Cerenkov equation and the Beer-Lambert law in Matlab 7.12.0 (The MathWorks Inc., Natick, MA). Water absorption coefficient was taken from (Hale, 1973). (Helo et al., 2014d)

1.2.1 Classical theory of Frank and Tamm

Frank and Tamm (1937) analysed Cerenkov emission and made the following simplifying assumptions:

1. The medium is unbounded and the track length infinite.
2. Dispersion (the dependence of the phase velocity of the wave on its frequency) is ignored.
3. The electron is assumed to move at constant velocity (i.e. the slowing down due to ionization and multiple Coulomb scattering are not taken into account).
4. The medium is assumed to be a perfect isotropic dielectric, thus the conductivity is zero, the magnetic permeability is equal to 1, and there is no absorption of radiation.

With the above assumptions, the fundamental equation for the output of Cerenkov radiation is given in equation 1.3,

$$\frac{d^2N}{dEdx} = \frac{\alpha Z^2}{\hbar c}\left(1 - \frac{1}{\beta^2 n^2}\right) = \frac{\alpha Z^2}{\hbar c}\sin^2\theta \qquad (1.3)$$

where,

N: the number of photons produced per unit path length *dx* of a particle with charge *Z* and energy interval *dE* of the photons.

$\alpha = \frac{e^2}{4\pi\epsilon_0 \hbar c}$: The fine structure constant (characterizing the strength of the electromagnetic interaction).

$\hbar = 1.0551 \times 10^{-34}\ m^2\ kg\ /\ s$: Planck's constant/2π.

Equation 1.3 can be expressed in different units as shown in equation 1.4.

$$\frac{d^2N}{dEdx} \approx 370Z^2\frac{photons}{eVcm}\left(1 - \frac{1}{\beta^2 n^2}\right) \qquad (1.4)$$

1.2.2 Radiation yield and spectral distribution

We may calculate the radiation intensity in terms of the number of photons from equation 1.3 in the following way. The number of photons *N* generated by a beta particle along a distance x within a spectral region defined by wavelengths $\lambda_1$and λ_2 is given by equation 1.5,

$$N = 2\pi\alpha x\left(\frac{1}{\lambda_2} - \frac{1}{\lambda_1}\right)\left(1 - \frac{1}{\beta^2 n^2}\right) = \quad 2\pi\alpha x\left(\frac{1}{\lambda_2} - \frac{1}{\lambda_1}\right)\ \sin^2\theta \qquad (1.5)$$

by considering the dispersion (i.e. the wavelength dependence of the refractive index) in the medium in equation 1.5, the number of photons generated per unit track length is expressed in equation 1.6,

$$\frac{dN}{dx} = \frac{\alpha Z^2}{\hbar c}\int_{E_{min}}^{E_{max}}\left(1-\frac{1}{\beta^2 n^2}\right)dE = \frac{\alpha Z^2}{\hbar c}\left[E_{max} - E_{min} - \frac{1}{\beta^2}\int_{E_{min}}^{E_{max}}\frac{dE}{n^2(E)}\right] \quad (1.6)$$

furthermore, as the speed of the charged particle is not constant, the number of photons generated by a charged particle is shown in equation 1.7.

$$N = \frac{\alpha Z^2}{\hbar c}\int_{n\beta>1}\left[E_{max} - E_{min} - \frac{1}{\beta^2}\int_{E_{min}}^{E_{max}}\frac{dE}{n^2(E)}\right] \quad (1.7)$$

As an example, let us consider a 0.96 MeV positron (the maximum energy of ^{11}C positron as shown in Table 1.2) moving through 1 mm of water. The positron velocity could be calculated from the special relativity theory shown in equation 1.8,

$$E_{Kinetic} = E_{Total} - E_{restmass} = m_0c^2\left[-1 + \frac{1}{\sqrt{1-\beta^2}}\right] \quad (1.8)$$

where,

m_0: the particle rest mass.

If we insert the rest mass of a positron $m_0c^2 = 511\ keV$, we can calculate the relative velocity $\beta = 0.94$. Then, the number of photons emitted from the movement of the positron can be calculated from equation 1.5,

N = 27.63 considering Z = 1, $\alpha = \frac{1}{137}$, $n = 1.33$, region of interest (ROI) is $\lambda_2 = 350$ and $\lambda_1 = 850$ nm. ROI is chosen where the light absorption in water is negligible.

By considering the dispersion of the medium, the number of photons emitted as a positron travels through 1 mm of water can be calculated from equation 1.6,

N = 28.42 considering ROI: $\lambda_2 = 350$ and $\lambda_1 = 850\ nm$. Thus $E_{max} = h\gamma = \frac{hc}{\lambda} = 3.543\ eV$, $E_{min} = 1.459$ eV, $\int_{1.459}^{3.543} \frac{dE}{n^2(E)} = 1.1626$ eV.

1.2.3 Duration of Cerenkov light flash

The Cerenkov effect is the result of a charged particle moving fast through a transparent medium and disturbing the electric field of the atoms. A pulse of electromagnetic radiation is emitted as a result of the atoms re-orientation to their original random charge distributions simultaneously. The duration of the Cerenkov pulse depends on the spread of the Cerenkov wave front and the position of the observer with respect to the particle trajectory. Burden and Hieftje (1998) calculated the Cerenkov pulse duration $\Delta t = 0.326 \times 10^{-12}$ sec for a light flash observed between the wavelengths of 300 and 350 nm at distance 1 cm away from the particle axis for a 1 MeV electron in water.

1.2.4 Charged particles and Cerenkov emissions

Charged particles in a medium will emit Cerenkov radiation when their velocity is greater than the speed of light in that medium. The threshold energy of the particle to emit Cerenkov emission as a function of the refractive index of the medium can be calculated according to equation 1.9,

$$E_{th} = m_0 c^2 \left[-1 + \frac{1}{\sqrt{1 - \frac{1}{n^2}}} \right] \qquad (1.9)$$

the threshold energy required for the production of Cerenkov photons in any specific medium increases proportionally with the mass of the particle, and decreases with increasing the refractive index of the media. Table 1.1 lists the calculated threshold energies of particles of different mass in

water (refractive index equal to 1.333 (Hale, 1973)), tissue (refractive index equal to 1.412 (Tearney et al., 1995)), and Perspex (refractive index equal to 1.52 (L'Annunziata, 2007)).

Table 1.1 Cerenkov threshold energies in MeV of different particles in water, tissue and Perspex.

Particle	Rest mass (MeV)	Threshold energy (MeV) In water	Threshold energy (MeV) In tissue	Threshold energy (MeV) In Perspex
Electron	0.511	0.262	0.213	0.167
Muon	105.6	54.1	43.98	34.62
Proton	938.3	480.7	390.7	307.6
Deuteron	1875.6	960.9	781.1	614.9
Alpha	3727.3	1909.7	1552.2	1221.9

1.2.4.1 Cerenkov radiation from protons

Protons may produce Cerenkov emission directly by disturbing the electric field of the atom. The threshold energy of a proton beam in order for it to produce Cerenkov light is 481 MeV in water (Table 1.1). Below the threshold there are no direct emissions of Cerenkov photons.

A proton beam loses its energy mainly by Coulomb interactions. The maximum energy transferred to a free electron by Coulomb interaction can be calculated via energy and momentum conservation laws (equation 1.10 and equation 1.11 respectively),

$$\frac{1}{2}MV^2 + \frac{1}{2}mv^2 = \frac{1}{2}MV_1^2 + \frac{1}{2}mv_1^2 \qquad (1.10)$$

$$MV + mv = MV_1 + mv_1 \qquad (1.11)$$

where M: mass of proton, V: velocity of proton before collision, V_1= velocity of proton after collision, m: mass of electron, v_1: velocity of electron after collision and v: electron binding energy.

By solving the energy and momentum conservation equations, the maximum transferred energy to the electron is equal to the proton energy divided by 459 (more information about the calculations can be found in appendix 1). If these electrons have energy greater than 0.262 MeV (assuming the refractive index of water is 1.333), then their speed will exceed the speed of light in water and they will emit Cerenkov radiation. A proton beam with energy at least 120 MeV is needed in order for secondary Coulomb electrons to exceed this threshold. A 60 MeV beam can produce only 140 keV electrons, which will not emit Cerenkov light in water.

Protons may also lose energy by non-elastic nuclear interactions (in non-elastic reaction, the total kinetic energy is not conserved), in which the proton is absorbed by a nucleus and the energy is transferred to either uncharged particles (neutrons or photons, which might cause further secondary ionizations, which may yield Cerenkov emissions) or heavy charged particles (like deuterons and alphas) which may cause Cerenkov emissions directly or via further ionization depending on their energy (Table 1.1).

Radioactive nuclei are produced along the beam path due to non-elastic interactions, which usually undergo beta plus decay (β^+). A positron travels a short distance in the medium (less than 1 mm in living tissue)(Levin and Hoffman, 1999) before it annihilates with an electron and produces two or more gamma ray photons (more information about β^+ decay can be found in appendix 2). Positrons with energy higher than 0.262 MeV will emit Cerenkov light (Jelley, 1958). All possible Cerenkov emission sources from proton interaction are stated in Figure 1.3.

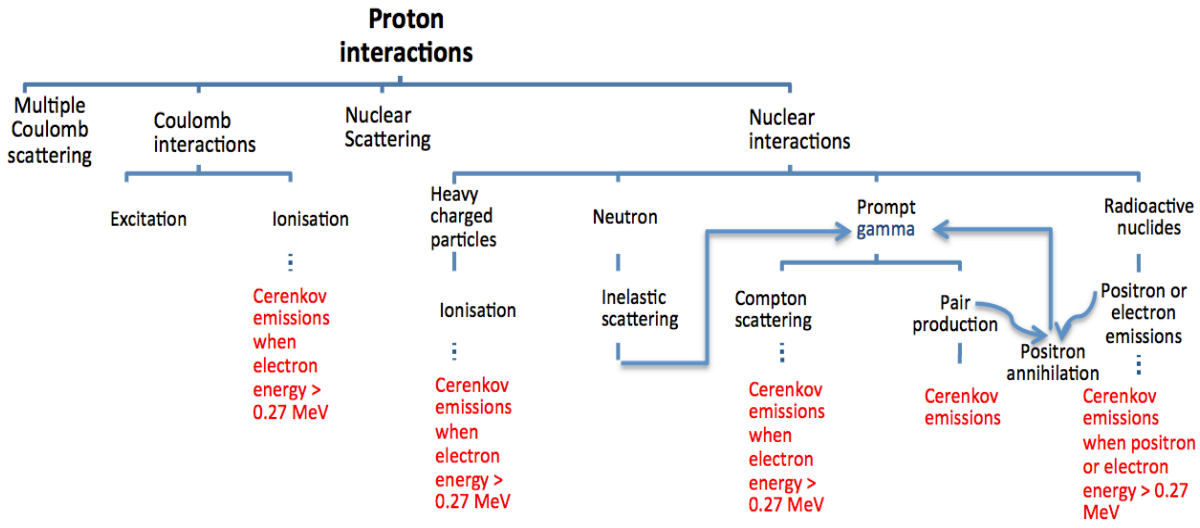

Figure 1.3 Proton interaction with matter and Cerenkov production. (Helo et al., 2014a)

1.2.5 Uncharged particles and Cerenkov emissions

Neutral particles like gammas and neutrons do not generate Cerenkov emission in media directly, because they don't possess a charge to disturb the atom's electric field. However, gamma radiation, as an example, produces Cerenkov light indirectly through pair production and Compton interactions.

1.2.5.1 Cerenkov radiation from gamma photon

A gamma beam loses its energy mainly by: (i) photoelectric absorption, (ii) pair production, (iii) Compton scattering. As gamma photons have no electric charge or rest mass, gamma radiation has high penetration power in material. The attenuation of gamma radiation in matter is defined as

$$I = I_0 \mathrm{e}^{-\mu x} \qquad (1.12)$$

where I: gamma ray intensity behind a given material of thickness x, I_0: initial gamma ray intensity, μ: the linear attenuation coefficient (cm^{-1}). The linear attenuation coefficient depends on the energy of the photons and the properties of a specific material. Mass attenuation coefficient is equal to the linear attenuation coefficient divided by the density of the absorber (g/cm^3). Figure 1.4 shows the total mass attenuation coefficient for photons in water as a function of photon energy, and includes contributions from the photoelectric effect, Compton effect and pair production in the total coefficient (Khan, 2012).

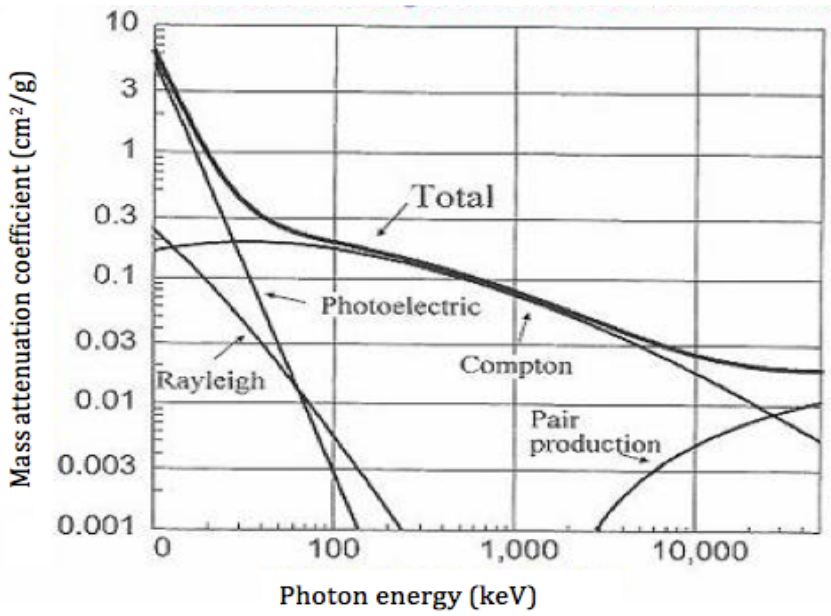

Figure 1.4 Energy dependence of the different gamma ray interaction processes in water. The total attenuation is marked, which is the sum of the partial attenuations due to the photoelectric effect, Compton effect and pair production (Khan, 2012).

The photoelectric effect is the absorption of a gamma ray by *K* or *L* shell electrons, and results in the release of an electron with kinetic energy equal to the incident gamma energy minus the binding energy of the electron. The probability of the photoelectric interaction is inversely proportional to approximately the third power of the photon's energy (Halperin et al., 2013). Photons with energy higher than 0.2 MeV in water are more likely to lose energy by the Compton effect and pair production (as seen in Figure 1.4). Photons with energy less than 0.2 MeV may be absorbed in the atom. However, the resulted photoelectrons will not have enough energy (0.262 MeV) to emit Cerenkov light in water.

Pair production is the interaction of gamma radiation with the field of a nucleus, and results in the creation of charged particles (i.e. electrons and positrons) from the gamma energy. Pair production creates electrons and positrons with energy equal to at least 0.511 MeV, which is enough to produce Cerenkov light in water.

In the Compton effect, the photon transfers a small fraction of its energy (E_γ) to an atomic electron and is deflected with less energy (E'_γ) in a certain angle (ϑ). The energy of the Compton scattered photon (E'_γ) is calculated according to equation 1.13.

$$E'_\gamma = \frac{E_\gamma}{1 + (\frac{E_\gamma}{mc^2})(1 - cos\vartheta)} \quad (1.13)$$

And the energy of Compton electron (E_e) can be expressed as,

$$E_e = E_\gamma - E'_\gamma - \varphi \quad (1.14)$$

where,

φ : The binding energy of the electron (usually assumed to be negligible compared to the photon energies).

Thus, Compton electron energy becomes,

$$E_e = E_\gamma - \frac{E_\gamma}{1 + (\frac{E_\gamma}{mc^2})(1 - cos\vartheta)} \quad (1.15)$$

the Compton electron energy spectrum extends from zero when $\vartheta = 0^\circ$ to its maximum value when $\vartheta = 180^\circ$. As an example, let us consider a gamma radiation with 6 MeV. Then, the spectrum of Compton electron energy (E_e) as a function of Compton angle (ϑ) is expressed in Figure 1.5.

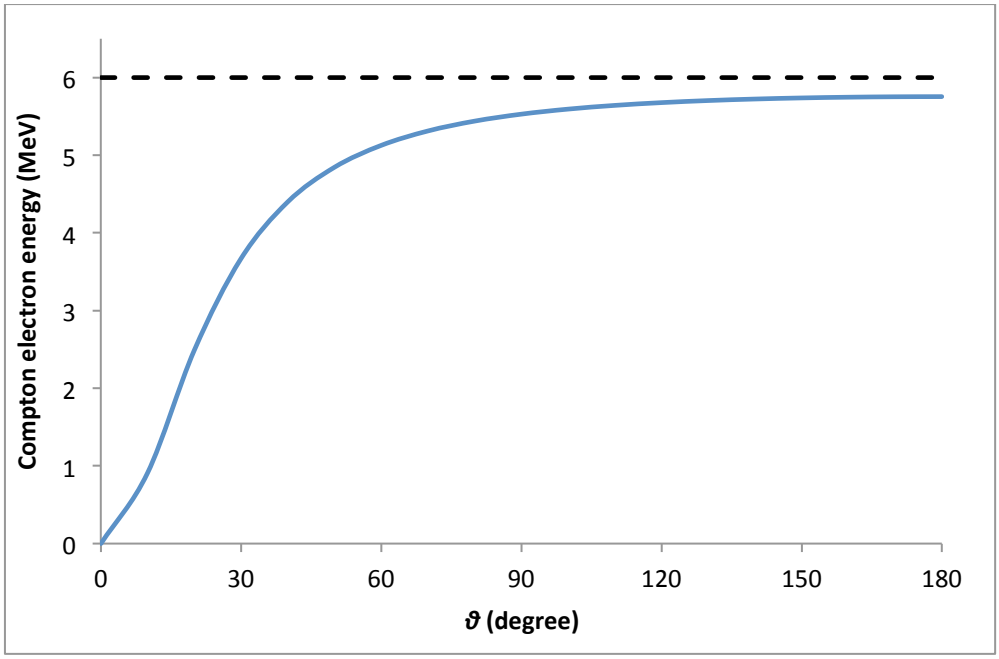

Figure 1.5 Compton electron energies as a function of the Compton angle for 6 MeV gamma rays.

For 6 MeV gamma radiation, Compton electrons exceed the Cerenkov threshold energy (0.262 MeV) when the Compton angle (ϑ) is greater than 3.1°. Hence, if we consider 180-deg Compton scatter, in which the maximum energy is transferred to Compton electrons, the gamma ray energy should be greater than 0.422 MeV in order for Compton electrons to pass the Cerenkov threshold energy (0.262 MeV) in water.

1.2.5.2 Cerenkov radiation from neutrons

Neutrons are another example of uncharged particles, which may motivate Cerenkov emission in a medium. Neutron particles collide only with nuclei of the atoms, and as a result of the collision [1] neutrons scatter elastically (elastic reaction: the total kinetic energy is conserved) or scatter inelastically (inelastic reaction: the total kinetic energy is not conserved, but the final nucleus is the same as the bombarded nucleus), [2] the neutron is captured by the nucleus and replaced by one or more secondary radiation emissions (Knoll, 2010; L'Annunziata, 2007). Figure 1.6 shows the total neutron cross-section curves for hydrogen-1 and oxygen-16, calculated from ENDF[1] nuclear database library (Chadwick et al., 2011).

[1] ENDF: database contains recommended, evaluated cross-sections of different nuclear interactions.

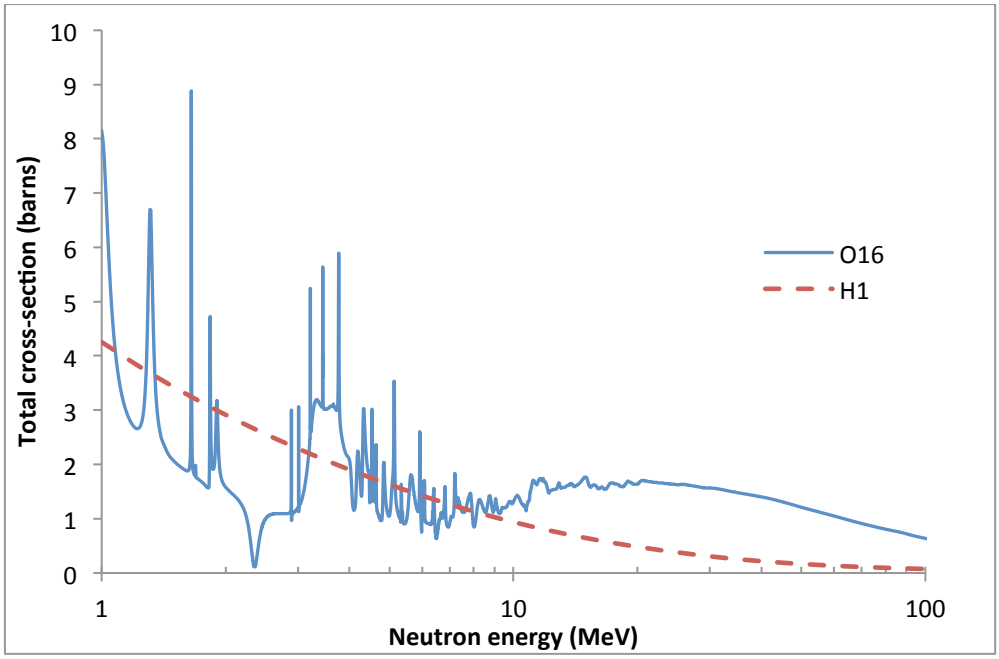

Figure 1.6 Total cross-section curves for hydrogen-1 and oxygen-16 over the neutron energy range 1 MeV – 100 MeV.

Fast neutrons (200 keV to 10 MeV) passing through water are more likely to interact with oxygen nuclei through elastic scattering or inelastic scattering, producing: (i) recoil nuclei which may ionize the medium; (ii) excited recoil nuclei (Willis and Carlile, 2009). The excited recoil nuclei emit gamma rays, which may introduce ionization to the medium, which may therefore produce Cerenkov light (as shown in Figure 1.3).

1.3 Radiotherapy

Radiotherapy has been used to treat cancer patience for more than 100 years. Conventional radiation therapy delivers two-dimensional (2D) beam of electrons or photons by using a linear accelerator (Linac) or cobalt-60 unit. An effective quality assurance (QA) is at the heart of any radiotherapy treatment.

Complicated radiotherapy treatment like intensity modulated radiation therapy (IMRT) and volumetric modulated arc therapy (VMAT) have progressively been applied in recent years (Bedford et al., 2009; Poppe et al., 2006). The aim of these techniques is to deliver a dose distribution, which conforms to the target volume, and minimise dose to surrounding normal tissues. The radiation field in IMRT and VMAT is precisely conformed to the three dimensional shape of the tumour by

controlling or modulating the intensity of the radiation beam in several small volumes.

1.3.1 Dose distribution and quality assurance

Dose distribution data are normally measured in a water phantom. These data are used in a dose calculation system to predict the dose distribution in a patient. Quality assurance (QA) assesses and validates the quality of the treatment by combining precise measurements of dose made at points in a phantom. Ionization chambers and diodes are widely used in external radiotherapy QA to measure the absorbed dose to water and validate the field size.

Complicated radiotherapy plans (like IMRT and VMAT) require dosimetric verification, individualised for each patient, before clinical delivery. Pre-treatment quality assurance is for verifying field shapes and monitor units (MU) by comparing the dose distribution calculated by the treatment planning system (TPS) and measured by a dosimetric device. By performing patient-specific QA both planning and delivery systems are being tested and checked. To compare the measured and predicted dose distributions, the gamma index is used which combines a measure of dose deviation and distance to agreement. The quality of the agreement is determined by the fraction of pixels that pass certain criteria (Boggula et al., 2010; Helo, 2010).

1.3.1.1 Central axis depth dose distributions

Ionization chambers are used to measure the absorbed dose at a depth z in a water phantom. Plane parallel or cylindrical ionization chambers are placed in the centre of the radiation field. The distance between the radiation source and the water surface (SSD) is fixed (usually 100 cm for a linear accelerator). Many correction factors must be applied when ionization chambers are used, to correct for ambient conditions (temperature, pressure and humidity), chamber polarity effects and ion recombination (Voltage effect). The percentage depth dose (PDD) profiles are used to check the beam quality by analysing the depth of maximum dose (d_{max}), the depth of 90% dose (R_{90}), the depth of Half-value dose (R_{50}) and the practical range (R_p)(R_p is only used with electron beam and heavy-ion beam). The practical range is defined as the depth where the tangent to the inflection point of the decreasing portion of the depth-dose curve meets the extrapolated Bremsstrahlung (X-ray) background (Cleland et al., 2004). Figure 1.7 shows the PDD of 9 MeV electron beam illustrating d_{max}, R_{90}, R_{50} and R_p.

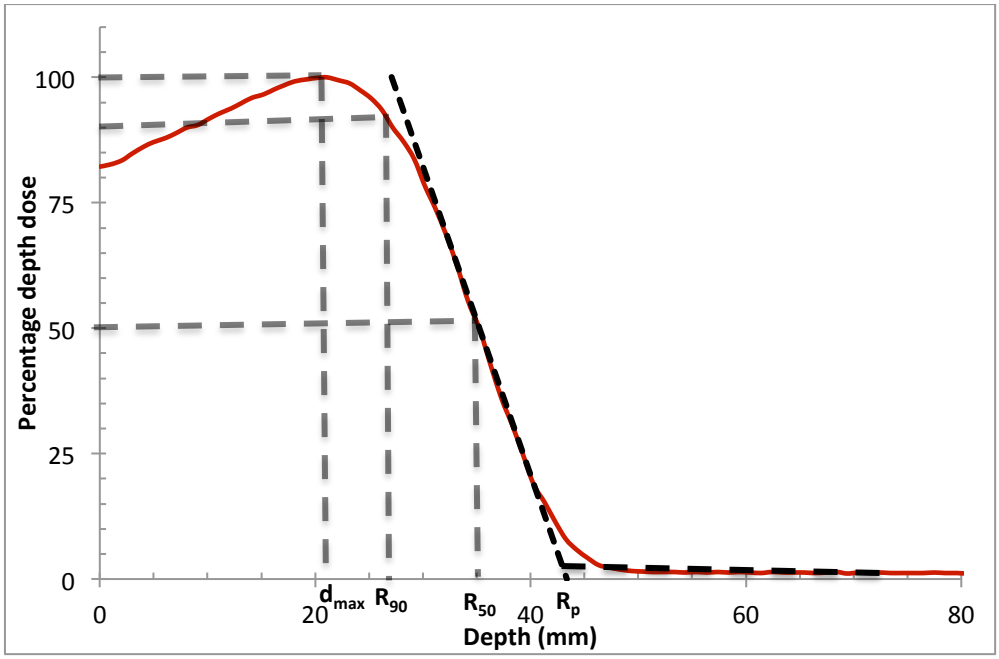

Figure 1.7 Percentage depth dose profile of 9 MeV electron beam with a field size of 10 x 10 cm^2. The figure shows the different range parameters. d_{max} = 21 mm, R_{90} = 27 mm, R_{50} = 35 mm and R_p = 43.5 mm. Measurements were taken with small detectors (NACP parallel plate ionization chambers and diodes) during the commissioning of a Varian linear accelerator (TrueBeam™, Varian Medical Systems, Palo Alto, CA) at University College London Hospital (UCLH).

Another beam quality specifier ($TPR_{20,10}$), for high energy photon radiation, may be used. $TPR_{20,10}$ is the ratio of the absorbed dose at depth 20 cm and 10 cm in water phantom with source chamber distance (SCD) = 100 cm.

Usually, the depth dose curves for electrons and photons are measured for all energies, which are used clinically and for different field sizes, at commissioning a new unit or after major maintenance, which takes several days.

1.3.1.2 Cross axis dose distributions

Ionization chambers or diodes are used to scan the absorbed dose laterally across the beam field at depth of maximum dose (d_{max}) and depth of 90% dose (R_{90}) to check the flatness of the beam at different depths. Figure 1.8 shows the off-axis profile of a 9 MeV electron beam at depth (d_{max} = 2.1 cm) and (R_{90} = 3.5 cm).

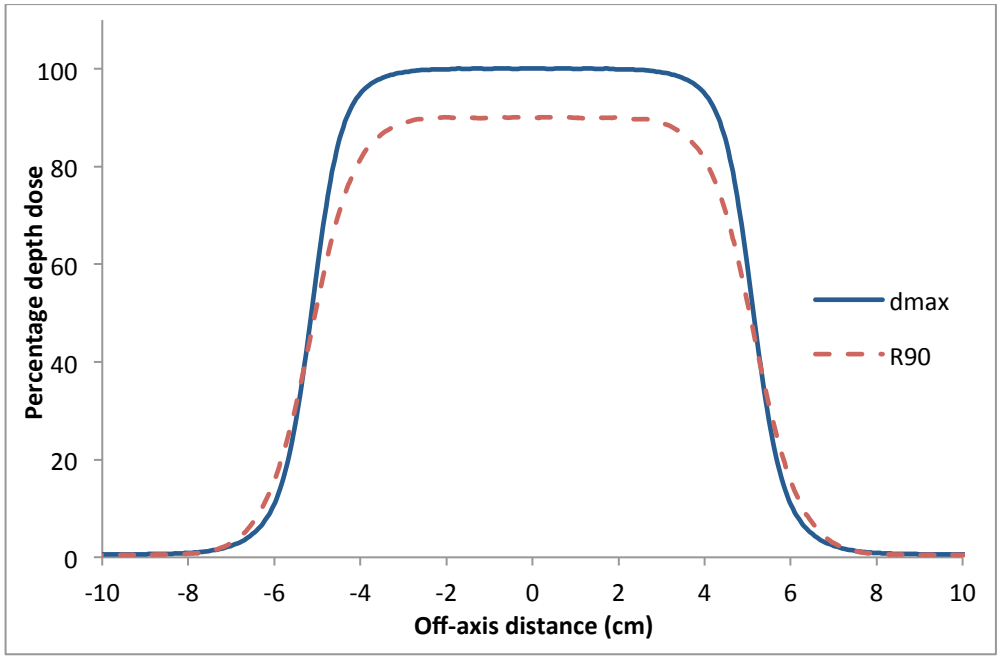

Figure 1.8 Crossbeam profiles of 9 MeV electron beam with a field size of 10 x 10 cm^2 at depth of maximum dose and depth of 90% dose. Measurements were taken with small detectors (NACP parallel plate ionization chambers and diodes) during the commissioning of a Varian linear accelerator (TrueBeam™, Varian Medical Systems, Palo Alto, CA) at UCLH.

Again, the crossbeam profiles for electrons and photons are measured for all available energies and for different field sizes, which takes a long time (days).

1.3.1.3 Film

Radiographic films can be used with a suitable phantom to verify the dose distribution in a patient treatment plan. Film is an integrating dosimeter with high spatial resolution, which can be used to measure the dose in a matrix of points, which provide a good means of obtaining dose distributions. By overlaying the printed isodose distribution curves of the measured and predicted data, it is possible to compare the predicted and measured dose distributions. The Gamma index is calculated from the electronic copy of the film (as explained in 1.3.1) (Helo, 2010).

The disadvantages of using film in pre-treatment verification are (1) the film response depends on the field size (Danciu et al., 2001), the beam orientation, the energy spectrum of the radiation and the depth (Piermattei et al., 2000); (2) film can only provide information in a single plane. Multiple films can be used, but are time-consuming to read out and analyse. To correct for all field sizes and measurement depths, film should be placed underneath sufficient build-up and with backscatter

material present (low energy scattered photons lead to over-response) in the event of low x-ray energy and gamma, and an accurate calibration should be performed (Bucciolini et al., 2003).

1.3.1.4 Gel

The use of radiation sensitive gels in dosimetric verification provides the ability to record 3D dosimetric information from a complicated treatment with high accuracy and spatial resolution. The gel is prepared in a container with a specific shape (cylindrical is recommended to minimize the oxygen penetration across the wall) then the irradiated gel is scanned using an optical-CT scanner (Xu et al., 2004).

The measured relative dose distribution from the gel measurement is compared with the dose distribution from the treatment planning system. However, gel preparation is time-consuming, and absolute dosimetry is still a challenge (Xu et al., 2004)

1.3.1.5 Thermoluminescent dosimeter (TLD)

A great number of absolute dose measurements can be achieved by using TLDs (TLD is made of crystalline materials which exhibit the phenomenon of thermo-luminescence) concurrently over the treatment volume. Different phantoms in different shapes can be used for this purpose. The disadvantages of using TLDs in pre-verification are that they need a long time to process and the results are not as accurate as methods like the ionization chamber (Khan, 2012).

1.3.1.6 Modern dosimeters

The increasing use of complex rotational therapy (like IMRT and VMAT) makes finding a convenient tool to do the pre-treatment patient-specific QA essential. Delta^4 (Scandidos, Uppsala, Sweden) is a diode array phantom that consists of 1069 p-type silicon diodes in a crossed array inside a cylindrical PMMA phantom as shown in Figure 1.9 (a). It is equipped with computer software, which compares the data from the treatment planning system (TPS) with measured data and finds the Gamma index (as explained in 1.3.1). Another example of modern dosimeter, the Octavius 4D phantom system (PTW, Freiburg, Germany) uses a two-dimensional detector array that consists of

729 cubic ionization chambers inside an octagonal rotating phantom offering 4D dose measurements as shown in Figure 1.9 (b), It is equipped with a computer software, which compares the data from TPS with measured data (as explained in 1.3.1) (Helo, 2010).

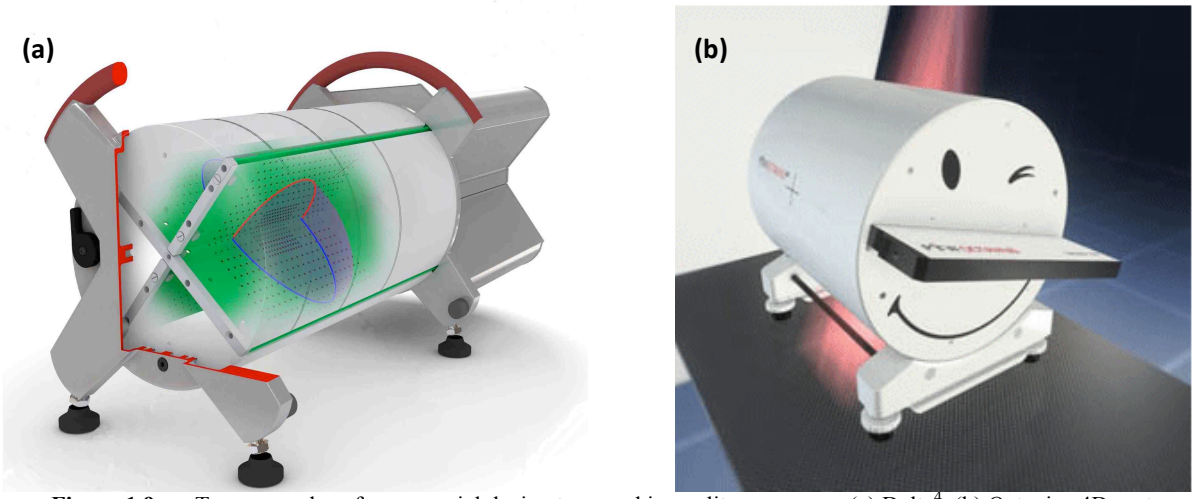

Figure 1.9 Two examples of commercial dosimeters used in quality assurance. (a) Delta[4]. (b) Octavius 4D system.

1.4 Proton therapy

Protons have been used to treat some types of cancer in the last decade (Lomax, 2008; Timmermann et al., 2007). Compared with conventional radiotherapy, proton therapy allows more precise delivery of dose to the tumour while avoiding or reducing dose to the surrounding tissue due to the sharp distal fall-off in dose at the Bragg peak (Brada et al., 2007; Levin et al., 2005). The Bragg peak happens because the energy loss by a heavy charged particle is inversely proportional to the velocity squared of the particle. Thus, the deposited energy increases with increasing depth and results in the phenomenon of the Bragg peak (Kacperek, 2009). Two techniques at present are used to deliver the dose in proton therapy: scanning beams and passive-scattered, modulated beams (modulator is used to form the spread out Bragg peak (SOBP)) (Lomax et al., 2001; Timmermann et al., 2007). However, the uncertainties in dose localization in proton therapy are still under investigation (Lomax, 2008; Paganetti, 2012; Pflugfelder et al., 2008). Figure 1.10 compares the depth dose distributions in water of 9 MeV electron beam and proton beam which was modulated using filters (as is usually done in hospitals) and had a maximum energy of 60 MeV. The proton beam shows a sharp dose cut-off beyond the range where the electrons beam shows a gradual dose drop-off beyond R_{50}.

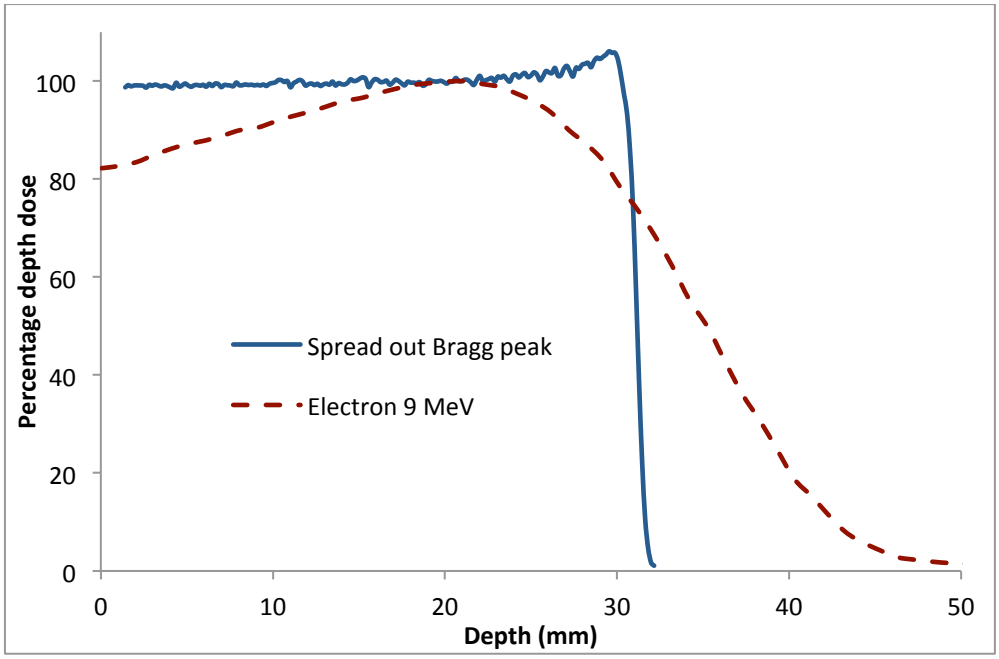

Figure 1.10 Comparison of depth dose characteristics of electron beam and proton beam in water. Measurements made during beam quality assurance (QA) measurements at the Clatterbridge Cancer Centre with a flat ion chamber (Classic Markus, PTW-Freiburg).

An example of the superiority of proton therapy over conventional therapy is the treatment of eye tumour where proton beams have precisely defined penetration and can be shaped to the target lesion with minimal irradiation to the nearby organs at risk like optic nerve and fovea (Bonnett et al., 1993; Kacperek, 2009).

1.4.1 Dose distribution and quality assurance

Currently, there are no internationally accepted standards for dosimetry of proton beams. Different type of dosimeters, such as calorimeters (the absorbed dose in a medium can be measured by sensing the temperature changes in that medium), ionization chambers, Faraday cups (Faraday cup is used to determine the number of protons in a beam) and diodes are used in clinical protons dosimetry (Andreo et al., 2002; Vatnitsky et al., 1999). Faraday cups are made of a metal cylinder, ions reach the inside of the cylinder are neutralized by accepting or donating an electron, which generate current in the cup. The resulting current is measured and used to determine the number of ions reaching the cup (Knoll, 2010; Khan et al., 2010). Diode detectors are made of semiconductor materials that convert ionising radiations (photons or charged particles) to current. The Ionizing radiation creates holes and free electrons inside the semiconductor; the number of the

produced hole-electron couples is propositional to the energy of the radiation to the detector (Knoll, 2010; Khan et al., 2010).

The deposited energy is usually measured in a water phantom using an ionization chamber; along with measurements of the tumour taken by a surgeon or by imaging (like ultrasound, CT and MRI), these data contribute at the planning stage, to calculate the dose distribution in a patient.

Quality assurance assesses and validates the quality of the treatment. Many methods are being investigated to verify the distal edge of the proton beam. Due to the high dose gradient at the distal edge of the Bragg peak, it is important to verify its true position in relation to the target volume. A gamma-camera may be used to measure prompt gamma emission, which is a single photon from the decay of an excited nucleus, typically in less than a nanosecond (Kurosawa et al., 2012; Min et al., 2006). Alternatively, positron emission tomography (PET) can be used to image the radioactivity arising from the proton beam in the medium, the decay time of the radioactive nuclei typically being from a few ms to many minutes (Hishikawa et al., 2002; Parodi et al., 2007). Using PET in proton therapy will be discussed in detail later in this chapter.

1.4.1.1 Central axis depth dose distributions

A parallel plate ionization chamber is recommended for proton depth dose measurements in a water phantom. For relatively low energy protons (less than 90 MeV, which is usually used with ocular tumours), a small field size equal to 4 cm x 4 cm and high dose rate is used, while for higher energy protons (above 150 MeV, which is usually used with big or deep seated tumours), field sizes and dose rates similar to those used in photon therapy are used. The use of plastic phantoms is not recommended in proton therapy, since they are sources of discrepancies in the determination of absorbed dose (Andreo et al., 2002; Vatnitsky et al., 1999).

The proton depth dose distribution curves consist of two regions: 1. Plateau region where the dose is approximately constant with depth. 2. Bragg peak region where the dose rises rapidly to a maximum. The practical range (R_p) in proton therapy is defined as the depth at which the absorbed dose beyond the Bragg peak or SOBP (SOBP is the sum of different energies of Bragg peaks) falls to 10% of its maximum value (Andreo et al., 2002). The depth dose distribution for a 60 MeV proton beam in water is shown in Figure 1.11.

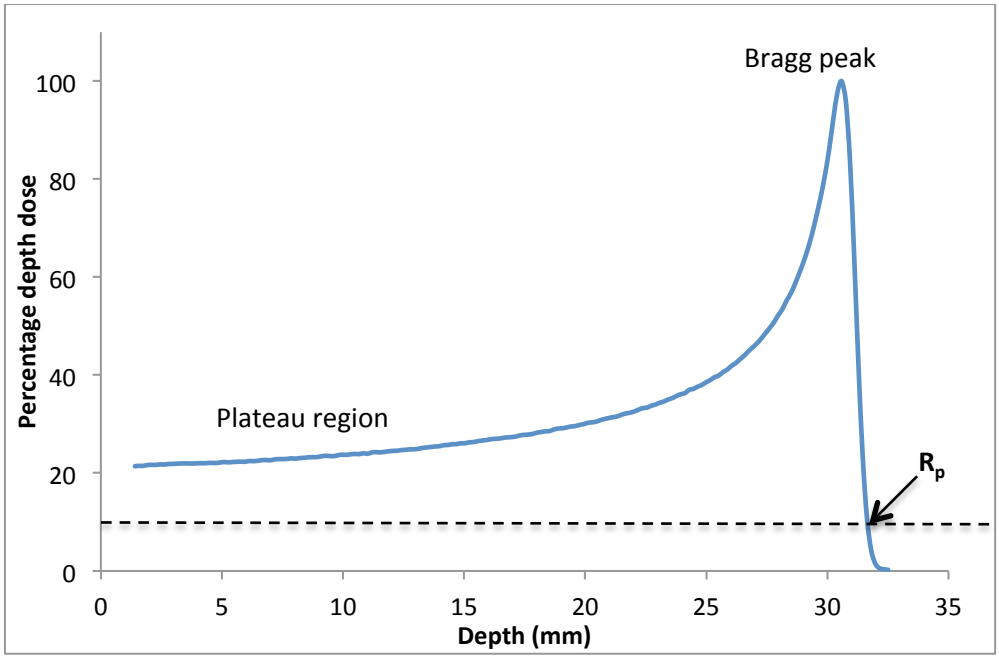

Figure 1.11 Percentage depth dose profile for a 60 MeV proton beam, illustrating the plateau and Bragg peak regions and the practical range (R_p). Measurements were made during beam quality assurance (QA) measurements at the Clatterbridge Cancer Centre with a flat ion chamber (Classic Markus, PTW-Freiburg).

1.4.1.2 Lateral depth dose distributions

Radiographic films are recommended to map the dose distribution in order to check the flatness and the symmetry of the proton beam. The film is placed in the direction perpendicular to the beam at different depths. Figure 1.12 shows radiographic images of a circular proton beam with diameter of 2.50 cm and energy 62 MeV. The film was placed behind a plastic phantom at the position of the Bragg peak.

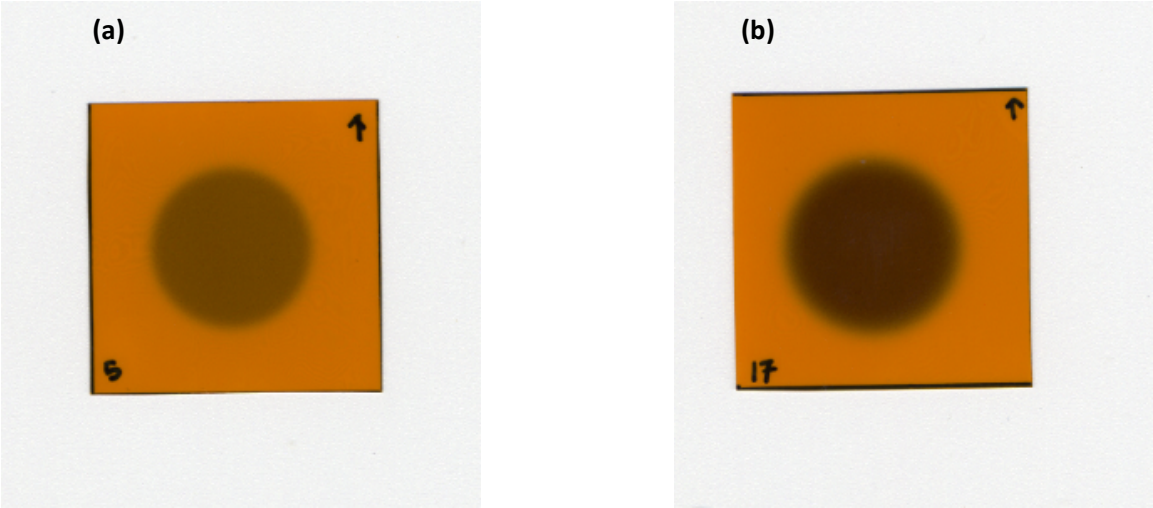

Figure 1.12 Lateral dose distribution for a 62-MeV proton beam. Radiographic images of proton beam where the film placed (a) behind a plastic phantom and (b) at Bragg peak position. The measurements took place in Catania proton therapy facility in Italy and performed by a UCL PhD student (Vanessa La Rosa).

1.4.1.3 Positron emission tomography (PET)

Positron emission tomography (PET) is a nuclear medicine imaging method, which creates a three-dimensional image of functional processes in the human body. Generally a short-lived radionuclide is introduced into the body. It emits a positron which then annihilates with an electron to emit pairs of gamma rays which are detected by suitable detectors. Figure 1.13 shows an example of a PET image obtained using a micro PET/CT scanner with 10 min exposure time. The activity of FDG (^{18}F solution) at the time of imaging was 10.5 MBq (Li et al., 2010).

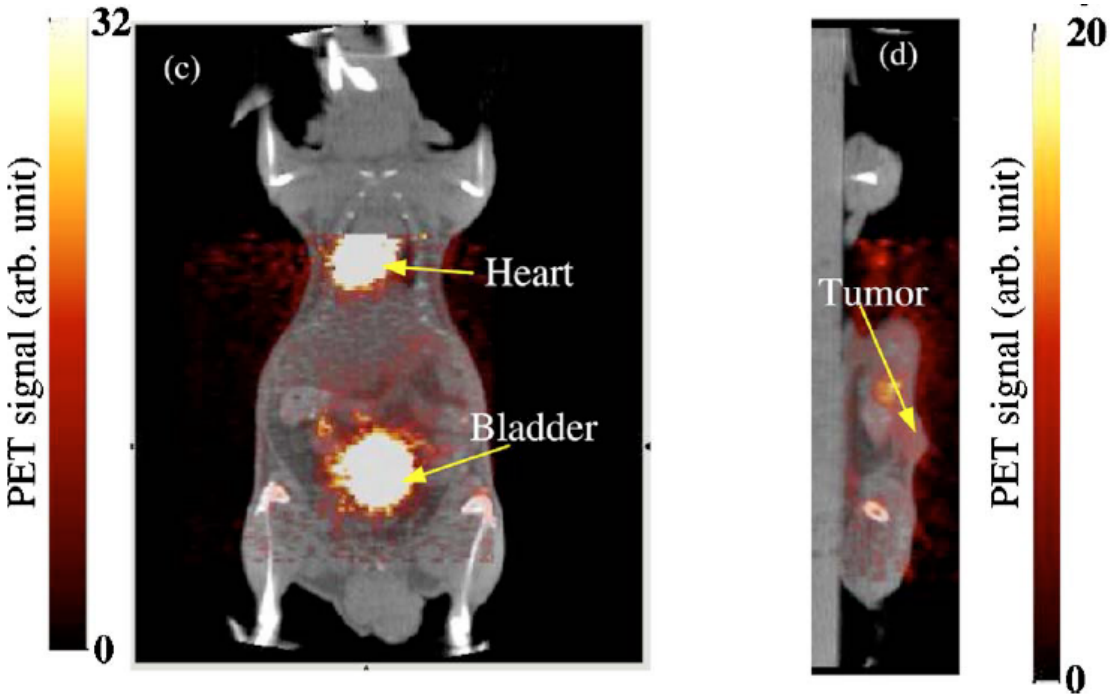

Figure 1.13 Reconstructed PET images fused with microCT images (Li et al., 2010).

PET images obtained after proton and carbon-ion treatment are currently being used as a quality assurance scheme to ensure the accurate functioning of beam delivery and treatment planning systems (Levin and Hoffman, 1999; Krane and Halliday, 1987). A PET image of a carbon-ion beam shows high pixel counts at the Bragg peak (some of the incident carbon particles become radioactive themselves). On the other hand, a PET image of a proton beam shows high pixel counts in the whole proton beam track (some of the target atoms which interact with the incident proton beam become radioactive) (Hishikawa et al. 2002).

Positron emitters are generated during proton therapy such as ^{11}C and ^{15}O created by nuclear interactions along the proton beam path, and can be imaged during (online) or shortly after (offline) treatment as a spatial marker of dose distribution. Table 1.2 gives information on the nuclear interactions leading to the production of positron emitters (Levin and Hoffman, 1999; Krane and Halliday, 1987).

Table 1.2 Positron-emitter production reactions in the human tissue; p: proton, n: neutron, α: alpha particles (Levin and Hoffman, 1999; Krane and Halliday, 1987).

Nuclear Reactions	Threshold Energy (MeV)	Half life Time (min)	Positron Max.Energy (MeV)
$^{16}O(p,pn)^{15}O^{(1)}$	16.79	2.037	1.72
$^{16}O(p,\alpha)^{13}N^{(2)}$	5.66	9.965	1.19
$^{16}O(p,\alpha pn)^{11}C^{(2)}$	27.50	20.39	0.96
$^{14}N(p,pn)^{13}N^{(1)}$	11.44	9.965	1.19
$^{12}C(p,pn)^{11}C^{(1)}$	20.61	20.39	0.96
$^{14}N(p,\alpha)^{11}C$	3.22	20.39	0.96
$^{16}O(p,\gamma)^{17}F$	0	1.07	1.74
$^{16}O(p,3p4n)^{10}C$	39.1	0.32	1.87
$^{16}O(p,p2n)^{14}O$	30.7	1.18	1.81
$^{18}O(p,n)^{18}F$	2.6	109.8	0.64
$^{12}C(p,p2n)^{10}C^{(3)}$	34.5	0.32	1.87
$^{12}C(p,\gamma)^{13}N$	0	9.97	1.19
$^{13}C(p,p2n)^{11}C^{(3)}$	25.5	20.3	0.96
$^{13}C(p,n)^{13}N$	3.2	9.97	1.19
$^{14}N(p,n\alpha)^{10}C$	17.2	0.32	1.87
$^{14}N(p,\gamma)^{15}O$	0	2.04	1.72
$^{14}N(p,n)^{14}O$	6.6	1.18	1.81
$^{15}N(p,n\alpha)^{11}C$	14.7	20.3	0.96
$^{15}N(p,nd)^{13}N$	20.4	9.97	1.19
$^{15}N(p,t)^{13}N$	13.8	9.97	1.19
$^{15}N(p,n)^{15}O$	3.8	2.04	1.72

(1) p + n includes deuteron (d)
(2) 2p + 2n includes alpha (α)
(3) p +2n includes triton (t)

Many isotopes are produced during proton therapy. However, in human tissue it is found that just six main interactions will dominate the production of the positron emitters (highlighted interactions in Table 1.2). The reactions induced by protons with ^{15}N, ^{13}C and ^{18}O are negligible due to the very low abundance of these isotopes in the human body. The cross-sections of the radioactive capture reactions (p,γ) are very small (micro-barns) compared with the cross-section of the six main interactions (millibarns) (Beebe-Wang et al., 2003; Malmer, 2001).

There are some difficulties when using PET to verify the dose distribution after proton therapy; (1) due to the delay required for patient transportation and relocating, generally the short half-life radionuclides such as ^{15}O would have decayed, and only the distribution of long half-life radionuclides such as ^{11}C can be imaged. (2) Errors may be caused by patient repositioning and anatomical changes during the patient transportation and relocating. (3) The biological washout of activity can considerably disturb the spatial distribution of the signal. (4) The relatively long imaging time needed (Parodi et al., 2008; Zhu et al., 2011).

1.4.1.4 Proton therapy and eye cancer

Cancer in the human eye can develop in several locations inside the eye including the iris, uvea and cornea. Around 400 to 500 new cases of eye cancer are diagnosed each year in the UK (NHS website). Uveal melanomas are the most common type of eye cancer, which arise from the pigment cells and may include the iris and progress inside the eye cavity. The cause of uveal melanoma is still unknown. However, exposure to ultraviolet radiation and indoor work conditions may increase the risk of eye cancer (Anderson and Skinner, 1961). Usually, ocular melanomas are diagnosed by performing an ultrasound scan and/or ophthalmoscopy. Proton therapy is preferable to treat ocular melanomas, as protons show a rapid energy loss at the end of their tracks (as explained in section 1.4), which help to minimize the dose to the surrounding sensitive tissues (the optical nerve).

Quality assurance measurements of the proton beam are performed on a regular basis in the clinic for verifying field shapes, monitor units and proton range in a water phantom by comparing the dose distribution calculated by TPS and measured by an ionisation chamber or film.

At the moment, no patient-specific QA (verification of the dose distribution and the beam range inside the target) for eye cancer patient is performed, mainly because of the lack of availability of a PET scanner close to the treatment room and the reasons stated in section 1.4.1.3.

1.5 Cerenkov emission in radiotherapy

1.5.1 Cerenkov luminescence tomography

Imaging using Cerenkov phenomena is very new technique and there are just few published works on Cerenkov luminescence tomography (CLT) for small animal imaging (e.g. Cho et al., 2009; Li et al., 2010; Spinelli et al., 2010).

CLT is a method in which ^{18}F-fluorodeoxyglucose(^{18}F-FDG) is used to reconstruct the radiotracer activity distribution inside the animal body by modelling the optical photon propagation with the diffusion equation and reconstructing the optical emission source distribution iteratively with a preconditioned conjugate gradient method (PCG). PCG is an algorithm which attempts to solve the diffusion equation (Li et al., 2010).

In Figure 1.14, an example of a CLT image obtained by using a CCD camera with 5 min exposure time and a filter for the wavelength range between 695 and 770 nm. The activity of FDG (^{18}F solution) at the time of imaging was 23.8 MBq. The CLT image was registered to a CT image (Li et al., 2010).

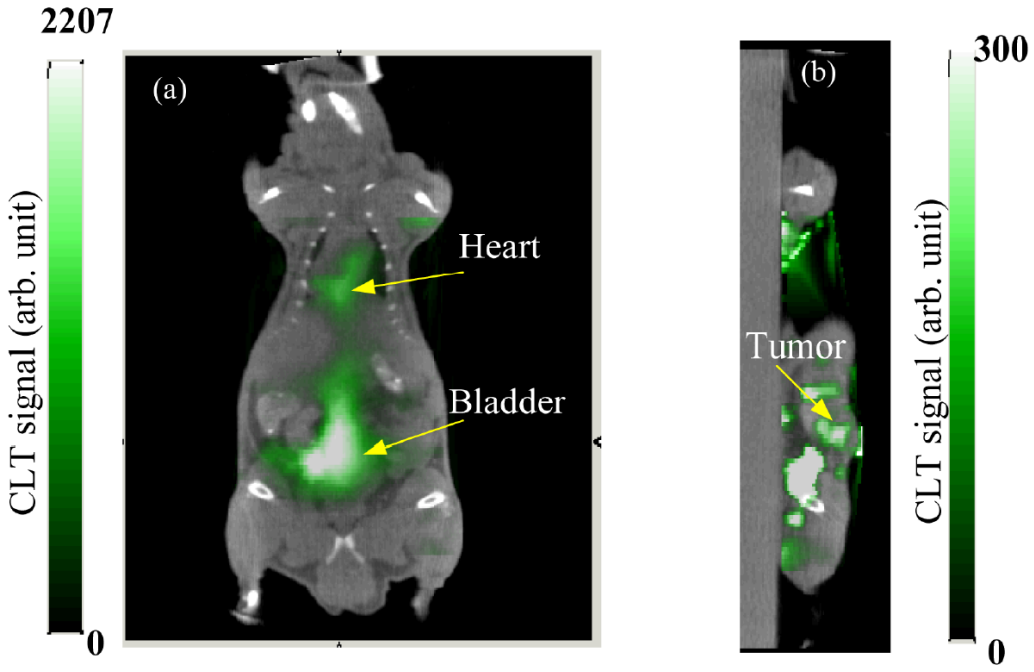

Figure 1.14 Reconstructed Cerenkov luminescence tomography images fused with microCT images using CCD camera (Li et al., 2010).

Spinelli et al (2013) presented for the first time images obtained by detecting Cerenkov radiation escaping the thyroid of hyperthyroidism patient (overactive thyroid), by using a cooled electron multiplying charge coupled camera (EMCCD).

1.5.2 Cerenkov fibre dosimetry

Scintillating fibre optic radiation dosimeters (SFOD) have been developed in recent years to be used for QA in photon and electron therapy (Beddar, 2006). The advantages of using SFOD in radiotherapy are (1) small size; (2) independent of temperature and pressure; (3) the amount of scintillating light is proportional to the deposited energy at low ionizing density. The disadvantages are noise from Cerenkov emission generated inside the fibre or the scintillator material (1.5% reported by Jang et al (2011)), non-proportionality to the dose at high ionizing density (for example, within a proton Bragg peak), which is called the quenching effect (temporary damage to the scintillation molecules by the high energy charged particles) (Jang et al., 2012a; Lambert et al., 2009).

Measuring Cerenkov emission generated in a plastic optical fibre (usually used to transmit the light) without a scintillating material was proposed as an alternative to SFOD for dosimetry in proton therapy and heavy ions therapy (Jang et al., 2012b). The advantages of using Cerenkov fibre dosimeter are (1) no quenching effect (no scintillation material needed), thus more accurate results; (2) good flexibility; (3) and no interference from electromagnetic fields. The disadvantages are (1) low light output (where in Cerenkov emission there are approximately 28 photons per MeV for electrons (as shown in section 1.2.2), compared to typical scintillation efficiency of between 1000 and 20000 photons per MeV (L'Annunziata, 2012)); (2) Cerenkov emission directionality dependence.

1.5.3 Tissue oxygenation and Cerenkov emissions

Recently, measuring Cerenkov emissions in tissue in radiation therapy has been proposed as a method for measuring haemoglobin oxygen saturation by exploiting the differential absorption of the Cerenkov light as a function of wavelength, using techniques pioneered in near infrared spectroscopy (Axelsson et al., 2012). The role of tissue oxygenation in radiotherapy effectiveness is well known.

1.5.4 Imaging Cerenkov emission during radiotherapy

Glaser et al (2013) published a paper about imaging Cerenkov light as a tool for quality assurance (QA) in photon therapy. They delivered, a 4 x 4 cm^2 photon beam field with energy equal to 6 MeV to a water phantom and Cerenkov emission was imaged by using a sensitive CCD. Recently, Zhang et al (2013) imaged Cerenkov emission from the surface of a flat tissue phantom and compared with the estimated superficial dose deposited by electron beam in that phantom measured by diode. They tested the dose linearity of Cerenkov measurement along with the crossbeam profiles.

1.6 Light emissions seen by patients during radiotherapy

Patients undergoing proton/Carbon therapy of the eye or the brain tumours frequently report seeing flashes of light (Khan et al., 2010; Newman et al., 2008). Similar sensations, known as phosphenes, have been reported by about 80% of astronauts. The major contribution is thought to be direct stimulation of photoreceptors by charged cosmic rays, with Cerenkov light contributing 5-10% of the visual sensation (anticipated by the shape of the reported light flashes) and minor contributions from stimulation of the optic nerve, stimulation of the retina by secondary particles and scintillation in the lens (Fuglesang, 2007; Sannita et al., 2006). Similar visual sensations from x-rays have been described for over a hundred years (Röntgen, 1898) and it is now well established that visual flashes occur during photon, electron, proton and heavy ion radiotherapy of the eye and brain (Khan et al., 2010; Newman et al., 2008; Schardt et al., 2013). Although the conventional explanation for light sensation during photon and electron radiotherapy has been direct stimulation of the retina (Avdeev et al., 2002), it is now accepted that there are also contributions from Cerenkov radiation (Newman et al., 2008; Steidley et al., 1989). Newman et al, (2008) proposed that the light seen by patients treated for head and neck cancer with megavoltage photon and electron beam can be attributed to Cerenkov radiation inside the eye. In their study, theoretical calculations of the Cerenkov light yield in the eye were estimated. However, the sensation of light during proton and heavy ion therapy has been assumed to be due to causes other than Cerenkov radiation because the primary therapeutic beam has insufficient energy to deliver Cerenkov radiation directly. These causes have been suggested to be emissions generated by interactions between protons and the beamline, production of free radicals (Khan et al., 2010), or direct stimulation of the retina (Schardt et al., 2013). Indeed, (Schardt et al., 2013) investigated the mechanism for flashes of light reported by patients undergoing carbon ion radiotherapy for skull base tumours (in

the energy range 80 to 400 MeV). They concluded that "as the ion beam energy is below the Cerenkov threshold (481 MeV), these [light flashes] cannot be caused by Cerenkov light", and showed that flashes were only observed when the retina was stimulated directly. Some of the patients in the same study reported seeing coloured light, and no explanation was given. The assumption of no Cerenkov emission during carbon-ion therapy was not correct, as the contributions of the secondary (like positron and electron) in producing Cerenkov emission should be considered. (Helo et al., 2014a)

Radioluminescence wasn't proposed as an explanation of the phenomena, mainly because the low light output. Radioluminescence happens when ionization particles pass through a material, which cause the material to luminescence. The reported efficiency of radioluminescence in water is 1.7 x 10^{-6} obtained from electron beam with energy no higher than 230 keV (Tarasov et al., 2007), where the reported efficiency of the fluorescence yield in air (nitrogen) between 300 and 430 nm is 4.23 photons/meter with electron energy 0.85 MeV (Lefeuvre et al., 2007). Radioluminescence in air or water is considered in this study to be negligible comparing with Cerenkov emission in water.

1.7 The objectives of the work

In this work the possibility of imaging Cerenkov emission in electron therapy as a QA tool using a commercial camera is explored. The delivered doses and dose rates are correlated to the measured image intensities in photographs of Cerenkov light. Comparisons are made between the percentage depth dose (PDD) of different electron beam energies with profiles measured from Cerenkov emissions in order to explore whether the latter can be used to check the stability of electron ranges in water. Comparisons are also made between the beam profile of 6 x 6 cm^2 electron beam at d_{max} with the Cerenkov beam profile at the same depth, to explore whether the latter can be used as a field size verification tool. Imaging Cerenkov light in radiotherapy (electron or photon) is affected, among other things, by: (i) the scattering pattern of electrons inside the water which is energy dependent; (ii) the angular dependency of Cerenkov production, which is also energy dependent; (ii) the refraction of the light when it travels from water to transparent phantom walls then to air. To better understand how these factors influence the expected measurements, a Monte Carlo simulation of the experiment was performed, which incorporated these effects. (Helo et al., 2014d)

The potential of using a standard commercial camera, which has the infrared filter removed, to image Cerenkov emission generated from electrons in breast like optical phantom for QA during breast treatment was explored. The delivered doses and dose rates are correlated to the measured image intensities in photographs of Cerenkov light. The Beam-direction profiles of Cerenkov emissions were used to check the electron ranges in phantom. The maximum in the light output with the incident electron angles was examined. The potential of using Cerenkov image for detecting and identifying differences between normal and diseased tissues was investigated.

Light emission in proton therapy was examined and two different components of Cerenkov emission were identified: *(1)* a fast component, which is Cerenkov emission from prompt gamma and neutron interactions; and *(2)* a slow component, which is Cerenkov emission from positrons and electrons emitted by radioactive decay. We compare the percentage depth dose (Bragg peak) of a 60 MeV proton beam with simulated distributions of ^{15}O, ^{11}C and Cerenkov emission in order to explore whether Cerenkov emissions can be used to determine the proton ranges in water. Comparisons are also made between the simulated and measured slow component of Cerenkov emission. The delivered doses and dose rates are correlated to the fast and slow components with a view to determining whether they can be used for online or offline verification. (Helo et al., 2014a)

Chapter 2

MONTE CARLO SIMULATION

2.1 Background

Monte Carlo (MC) simulation is a computerized mathematical algorithm that depends on a sequence of random numbers (seed) generated during the simulation to solve a problem by finding numerical results. Different seeds of random numbers give similar results to within the statistical error (variation in the simulation results between different runs) (Binder and Heermann, 2010).

Geant4 is an open source Monte Carlo toolkit for the simulation of the path of particles through different materials. Geant4 is used to simulate nuclear and accelerator physics, in addition to studies in medical and space science (Geant4 Publications, 2012). Monte Carlo simulation was proposed as alternative to the analytical methods used in dose calculation in radiotherapy (Verhaegen and Seuntjens, 2003). The advantages of using Monte Carlo in treatment planning system are (1) better accuracy in the calculation of the dose distribution in inhomogeneous media; (2) MC allows the possibility of investigation of the influence of different factors on the treatment plan (Caccia et al., 2007).

Several Monte Carlo codes have been developed to handle the transportation of radiation through matter (EGSnrc, MCNPX and Geant4 (Agostinelli et al., 2003)) or the transportation of light (MCML packages (Wang et al., 1995)). Geant4 is the only software can handle both the radiation and optical light transportation simultaneously (Glaser et al., 2013). In addition, Geant4 is compatible with different analysis and visualisation programmes (Root, openGL, etc.), and is capable of handling varied nuclear interactions and optical emissions.

Geant4 simulates the passage of charged particles in medium by invoking different processes, which depend on the type of the particles. Three different types of particles are handled in Geant4, charged particles, uncharged particles and optical photons. Figure 2.1 illustrates the potential different processes for each type of particle in a medium. In Geant4, two processes produce optical photons, the Cerenkov effect and scintillation. Unlike other particles, optical photons are generated in Geant4 without energy conservation (i.e. the charged particle doesn't lose energy to produce Cerenkov emission) (Geant4 Publications, physics group, 2012; Geant4 Publications, 2012; Perl, 2003).

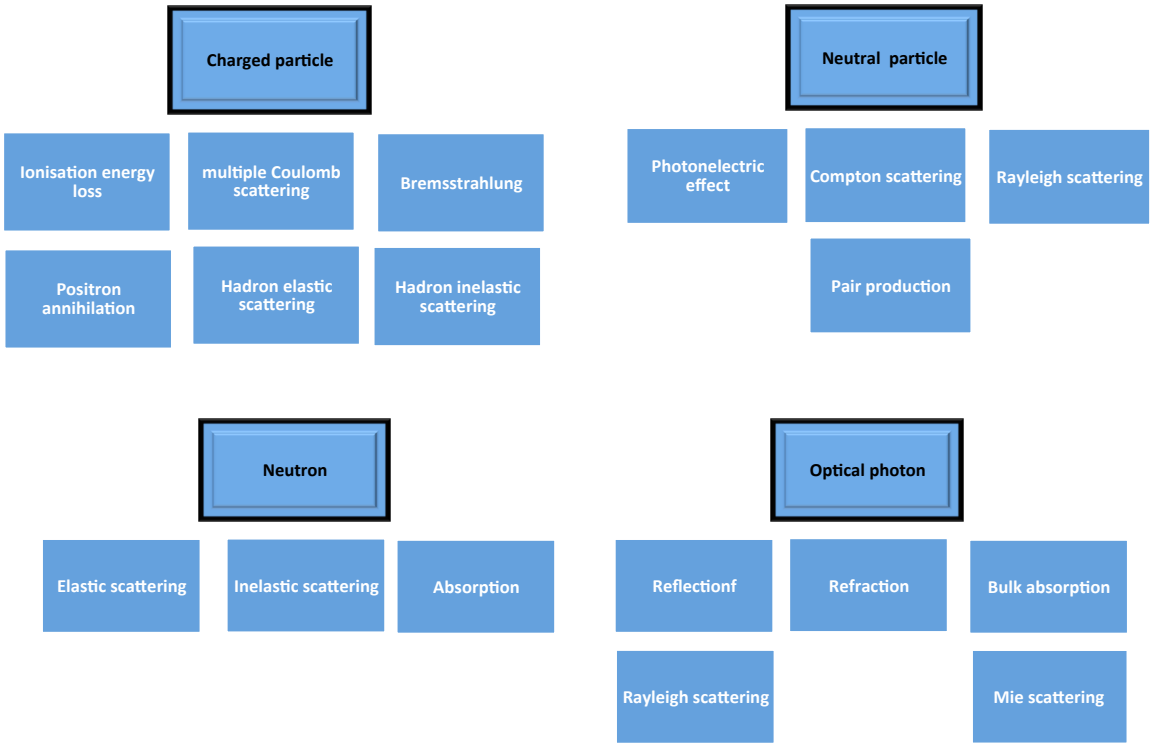

Figure 2.1 Different physics processes implemented in Geant4 for charged, uncharged, neutron and optical particles.

Cerenkov process happens when a charged particle travels through a dispersive medium faster than the group velocity of light in that medium. When the medium atoms emit Cerenkov light the charged particles lose a small amount of its energy. However, in Geant4 this is not taken into account. The energy loss because of emitting Cerenkov light is too small (≈ eV over 1 cm) compared to the energy loss by ionization processes (≈ MeV over 1 cm) (Krane and Halliday, 1987).

The Cerenkov process is implemented in Geant4 by adding the user-defined optical properties of the materials. The optical properties could be a function of the photon's energy or constant. In practice, the optical properties are quoted in terms of the energies of the photons (eV), the absorption length (cm), and the refractive indices of the materials used in the simulation. The absorption length is the average distance travelled by a photon before being absorbed by the material (Geant4 Publications, 2012; Jelley, 1958).

In Geant4, the charged particles are tracked to the end of their range. Nevertheless, when the energy of the charged particle is high, the energy is lost via discrete interactions (i.e. generating secondary particles) by the processes described in Figure 2.1. However, when the particle energy is

below the threshold energy, the energy is lost continuously and no secondary particles are produced. The threshold is known as a cut-off value and is determined by the user as a compromise between accuracy and speed of calculation. In practice, this cut-off value is cited as a distance, which Geant4 converts into energy using pre-installed empirical formula (Geant4 Publications, physics group, 2012; Geant4 Publications, 2012).

2.2 Electron beam simulation

A clinical electron beam entering a water phantom was simulated using a Monte Carlo simulation [Geant4.9.6 (Agostinelli et al., 2003; Geant4 Publications, physics group, 2012)] to investigate the possibility of using Cerenkov emission in daily quality assurance (QA) checks (including assessment of depth dose, dose linearity, dose rate linearity and beam profile) for an electron beam. A simulation was performed of the deposited energy and of Cerenkov production in water. Monte Carlo simulation was used to predict the measured light distribution around the water phantom, to reproduce Cerenkov images and to find the relation between deposited energy and Cerenkov production. The camera was modelled as a pinhole camera in Geant4, to attempt to reproduce Cerenkov images. In all simulations, 10^7 electrons were executed unless stated otherwise. The cut-off value for all particles in all simulations was 0.1 mm (i.e. approximately 0.1 MeV for an electron in water) unless stated otherwise.

2.2.1 Monte Carlo code validation

2.2.1.1 Depth dose distribution and cross beam profile simulations

The dose deposited and Cerenkov light distributions were investigated using Geant4 to simulate a clinical electron beam with a customised energy spectrum and beam divergence. The simulation was fine-tuned and validated by comparing the calculated electron dose distributions in water against measurements taken with small detectors (NACP parallel plate ionization chambers and diodes) during the commissioning of a Varian linear accelerator (TrueBeam™, Varian Medical Systems, Palo Alto, CA) at University College London Hospital (UCLH). Electron beams with energies of 6 MeV, 9 MeV and 12 MeV and field sizes of 10 x 10 cm^2 were simulated irradiating a 50 x 50 x 50

cm^3 water phantom with a wall thickness of 0.5 cm Perspex. Figure 2.2 shows the geometry of the simulation and the scoring volumes of (a) depth dose profile and (b) crossbeam profile.

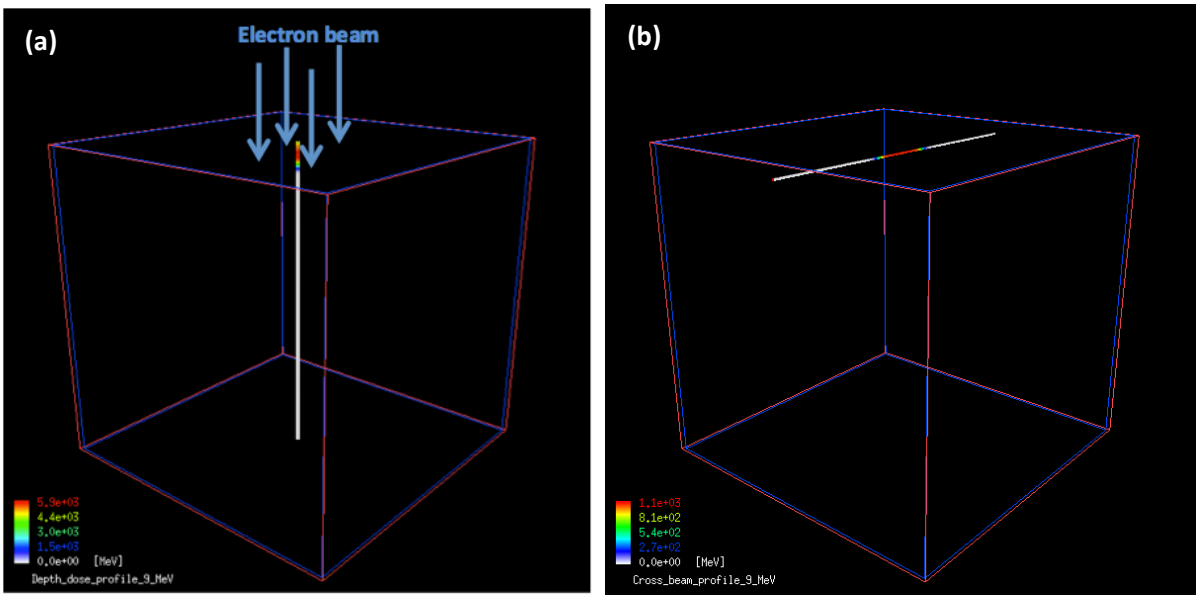

Figure 2.2 Simulation of 10 x 10 electron beam with energy of 9MeV, the phantom is made of 50 x 50 x 50 cm^3 of water with a wall thickness of 0.5 cm Perspex; the phantom-collimator distance is 80 cm; the standard deviation of the beam angular profile is 0.6 degree. (a) The scoring volume of the depth dose profile is a square 0.5 x 0.5 cm^2 with step equal to 0.1 cm. (b) The scoring volume of the transverse profile is a square 0.3 x 0.3 cm^2 with step equal to 0.5 mm at depth of maximum dose (d_{max}).

Ideally, a phase-space data of the simulated linear accelerator output should be imported as a particle source in the Monte Carlo code. However, the phase-space of the used linear accelerator was not available, and using any phase-space files available in the IAEA website (offered for specific machines) will not enable us to tune the initial electron energy to achieve the best fit to the measured depth dose and profile distributions where the fine-tuning is an essential part of the MC treatment head commissioning process (Righi et al., 2013; Pimpinella et al., 2007). Alternatively, we used the expected energy spectrum distributions of 6 MeV, 9 MeV and 12 MeV electron beams. The energy distributions were simulated as a quasi-Gaussian energy spectrum, with an additional long tail, and a Gaussian angular distribution were fine-tuned in the simulation to match the simulated depth doses to ionization chamber measurements.

Figure 2.3 illustrates a comparison of the depth dose profile of a 9 MeV electron beam between ionization chamber measurement and Monte Carlo simulation considering the energy distribution (i) mono-energetic 9 MeV electron beam, (ii) a Gaussian distribution with centred energy 8.6 MeV

and full width at half maximum (FWHM) equal to 1 MeV, and finally (iii) a quasi-Gaussian energy spectrum, with an additional long tail, and a Gaussian angular distribution which were fine-tuned in the simulation to match the simulated depth doses to ionization chamber measurements.

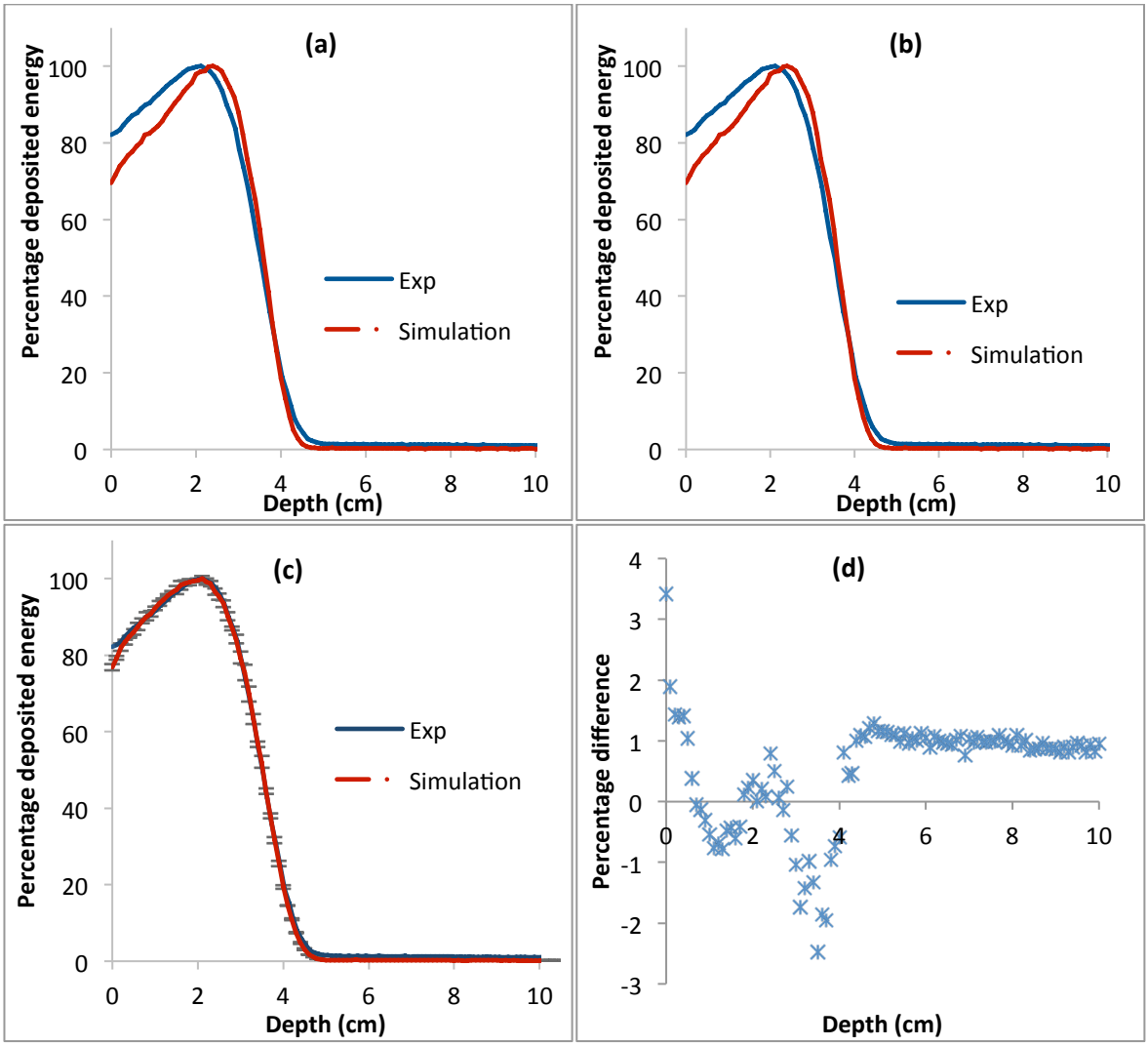

Figure 2.3 Comparison of depth dose profile between ionization chamber measurements and Monte Carlo simulations, for a 9 MeV electron beam. The electron energy spectrum is (a) mono-energy of 9 MeV, (b) Gaussian with centred energy 8.6 MeV and FWHM equal to 1 MeV and (c) quasi-Gaussian energy spectrum with an additional long tail, the beam divergence (sigma) was 0.6 deg. Error-bars illustrate the statistical standard deviation of the simulation data. (d) The percentage difference of the experimental and simulated depth dose profiles of the 9 MeV electron beam in (c).

Figure 2.4 shows a comparison between measured and simulated depth dose for electron energy of 6 MeV and 12 MeV respectively, the input electron energy distribution is again assumed to be a quasi-Gaussian energy spectrum, with an additional long tail, and a Gaussian angular distribution

which were fine-tuned in the simulation to match the simulated depth doses to ionization chamber measurements. The full width at half maximum (FWHM) of the Gaussian energy function was 0.8 MeV and 1.2 MeV for 6 MeV and 12 MeV electron beams, respectively.

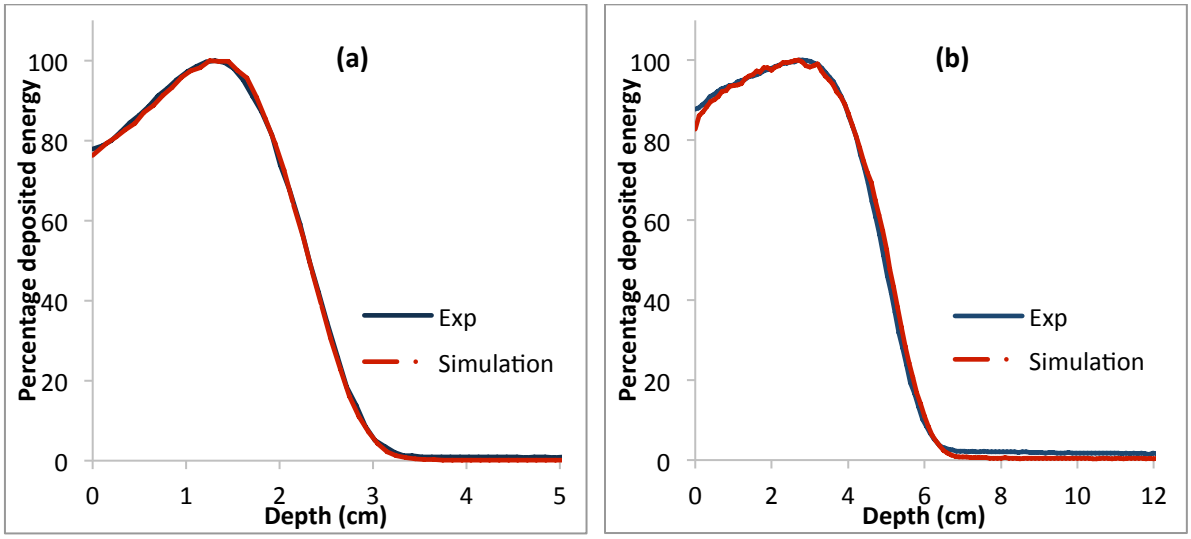

Figure 2.4 Comparison of depth dose profile between ionization chamber measurements and Monte Carlo simulations, for (a) 6 MeV electron beam and (b) 12 MeV electron beam. The electron energy spectrum is quasi-Gaussian energy spectrum with an additional long tail. The full width at half maximum of the Gaussian energy function was 0.8 MeV and 1.2 MeV for 6 MeV and 12 MeV electron beams, respectively.

The depth of the maximum dose (d_{max}) of 6 MeV, 9 MeV and 12 MeV electron beams was found at 1.3 cm, 2.1 cm and 2.7 cm respectively. Comparisons of the crossbeam profiles at d_{max} in water against diode measurements for 6 MeV, 9 MeV and 12 MeV electron beam are shown in Figure 2.5.

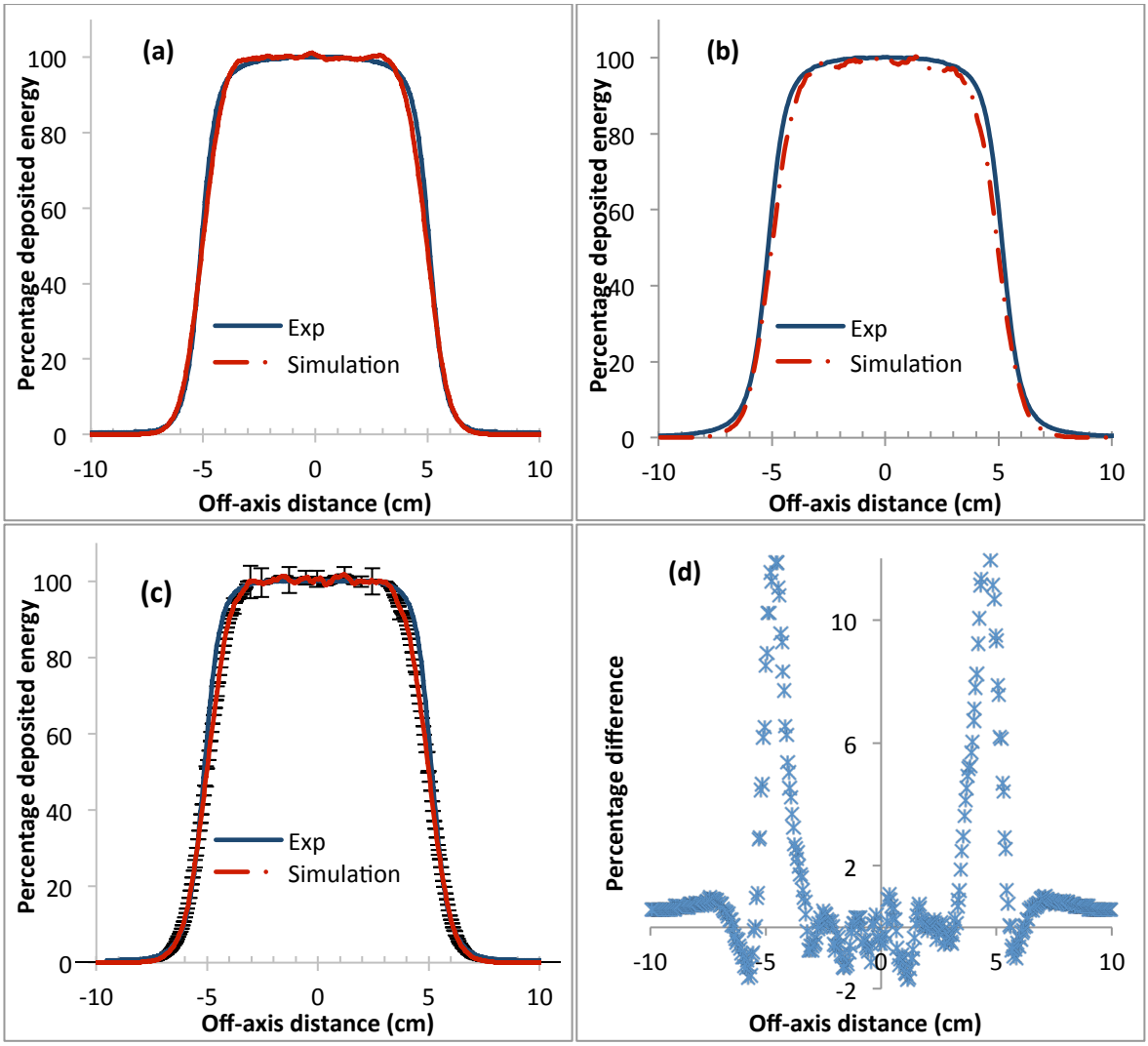

Figure 2.5 Comparison of crossbeam profile at depth of maximum dose between diode measurements and Monte Carlo simulation, for (a) a 6 MeV electron beam, (b) a 12 MeV electron beam and (c) a 9 MeV electron beam. The field size was 10 x 10 cm^2. Error-bars illustrate the statistical standard deviation of the simulation data for 9 MeV electron beam. (d) The percentage difference of the experimental and simulated crossbeam profiles of the 9 MeV electron beam.

It can be seen that the energy spectrum and the beam divergence employed in the simulation satisfactorily reproduce the data measured with an ionization chamber and diode to within 2% apart from the entrance dose of the depth dose profiles and the shoulders of the crossbeam profiles. This could be due to the simplified electron energy and divergence model used compared to the real distribution from the applicator.

2.2.1.2 Justification of the customised energy spectra

Geant4 was employed to model the end of electron beam line and the beam interactions in a water phantom. To simulate one beam with a specific field size, we took the following steps: (1) An initial prediction of the energy spectrum (Gaussian distribution with tail) was suggested; (2) We compared the simulated depth dose distributions with those measured by the ionization chamber at UCLH; (3) The energy spectrum was tuned as necessary in the simulation to match the simulated depth doses to ionization chamber measurements; (4) We compared the simulated central axis dose distributions at d_{max} and R_{90} (as described in 1.3.1.1) with those measured by diode at UCLH; (5) The angular distribution of the beam was tuned as necessary in the simulation to match the simulated central axis doses to diode measurements; (6) Steps 2 to 5 were repeated until we were satisfied with the results. To construct another beam in our simulation with different energy or field size, the previous process was followed. This means that the process of constructing a beam is independent of the energy or field size of that beam.

To check how realistic our method in estimating the energy spectra is, we implemented the phase space files of Varian 2100CD found on IAEA website (www-nds.iaea.org) to Geant4. The phase space of two energies 6 MeV and 9 MeV electron beams were used to retrieve the deposited energy inside the water phantom as described in 2.2.1.1 and compared to the ionization chamber measurements. Figure 2.6 illustrates a comparison of the depth dose profiles of 6 MeV and 9 MeV electron beams between ionization chamber measurements and Monte Carlo simulations. The kinetic energies of the incident electrons were dumped to file before they hit the water phantom and compared to the customized energy spectrum found by us. Figure 2.7 illustrates a comparison of the kinetic energy spectra of the 6 MeV and 9 MeV electron beams between phase space data and customized kinetic energy data.

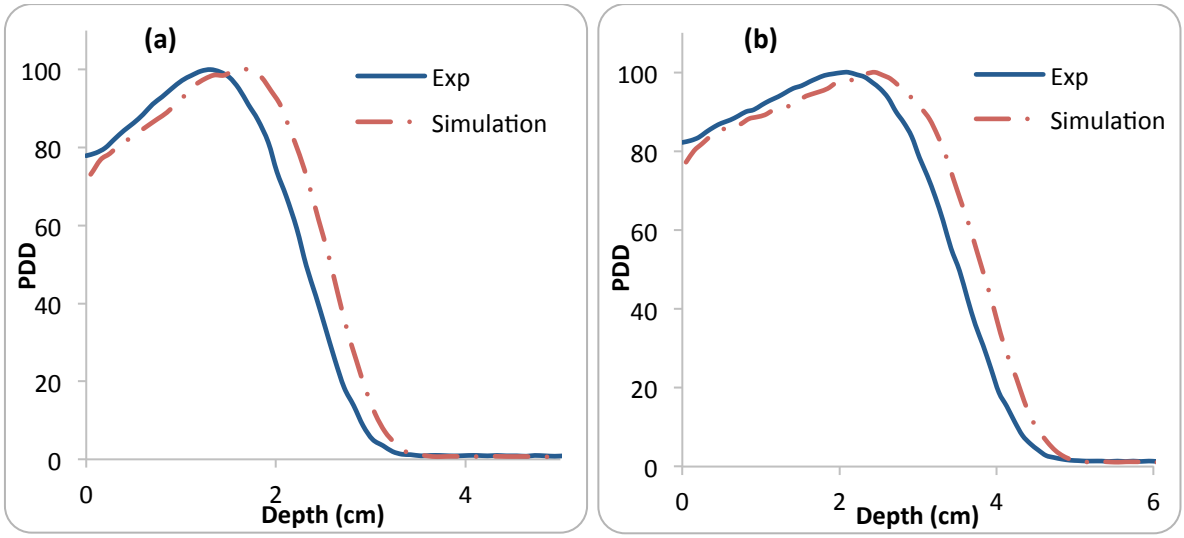

Figure 2.6 Comparison of depth dose profile between ionization chamber measurements and Monte Carlo simulations, for (a) 6 MeV electron beam and (b) 9 MeV electron beam. Simulations used the phase space files of Varian 2100CD.

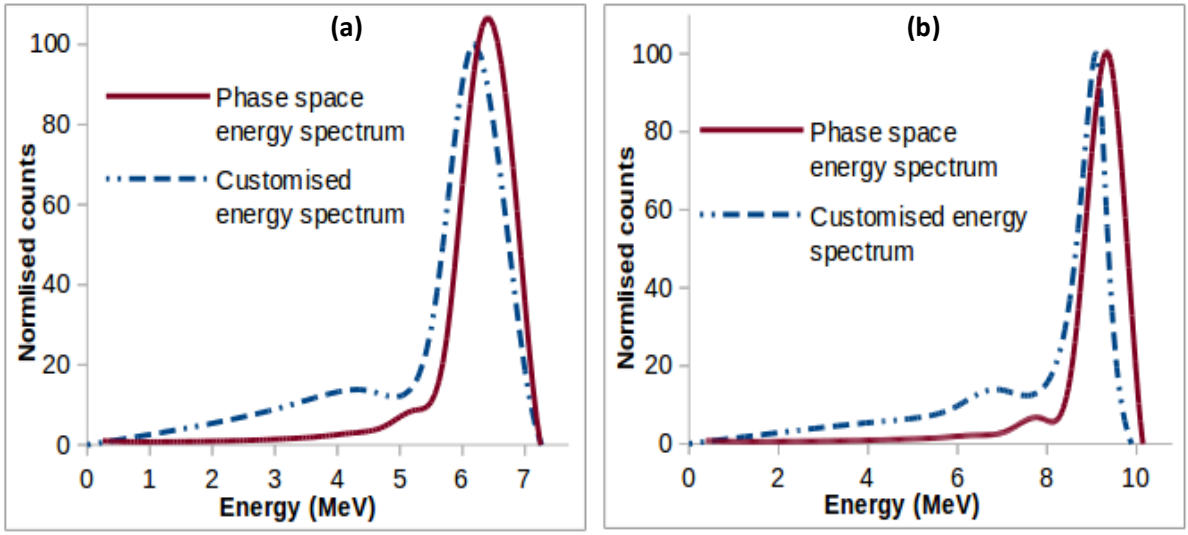

Figure 2.7 Comparison of energy spectrum between IAEA phase space data and customised data, for (a) 6 MeV electron beam and (b) 9 MeV electron beam.

As expected, there are differences between the simulated depth profile based on the IAEA phase space data and the ionization chamber measurement at UCLH. Since the chosen IAEA phase space and the customised kinetic energy reflect the output of two different machines, we found that using the IAEA phase space data of a random machine in our simulation is impractical, as it will not enable us to tune the initial electron energy.

It can be seen that, our customized kinetic energy distributions have the same behaviour as the IAEA phase space data.

2.2.1.3 Cerenkov implementation verification

In order to verify the Cerenkov process implementation in our code, we compared the simulated average number of Cerenkov photons generated in water with that predicted by Cerenkov theory (equation 1.5) for different mono-energetic electron beams as shown in Figure 2.8. The electron range in water which is used in theoretical calculation was taken from continuous slowing down approximation (CSDA) tables and electron practical range table (as defined in 1.3.1.1) (Hale and Querry, 1973; Kasarova et al., 2007; NIST Publication, 2013).

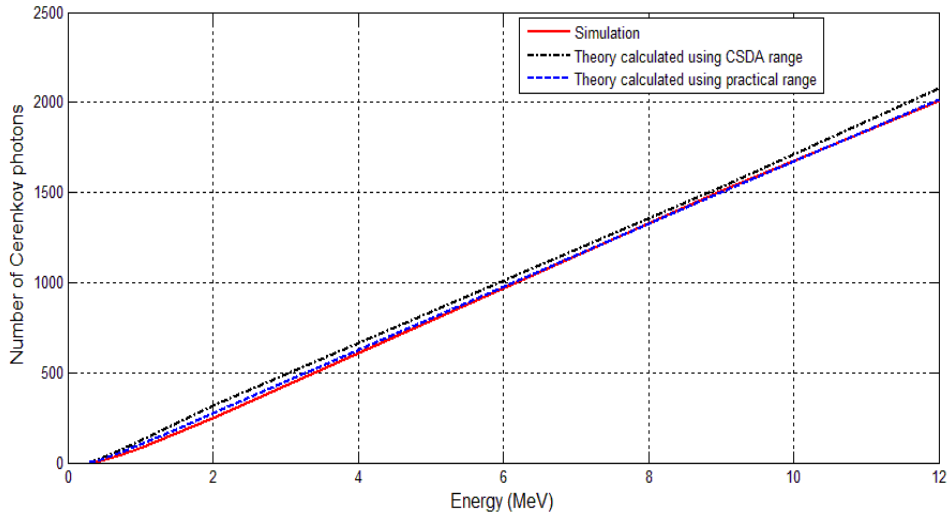

Figure 2.8 Simulated and theoretical average number of Cerenkov photons generated in water by movement of different energies of electrons.

The slight difference between the simulated and the theoretical average number of Cerenkov photons generated in the water phantom (Figure 2.8) could be due to Cerenkov theory assuming that the charged particle velocity is constant during movement inside a material. Consequently, the theory overestimates the number of generated photons in comparison with simulation where the particle energy is lost gradually by ionization processes. It was found that using the electron practical ranges (as defined in 1.3.1.1) rather than the CSDA ranges in the theoretical calculation slightly improve the estimation of the generated photons.

2.2.2 Secondary emission in electron therapy and Cerenkov emission

Electrons interact with matter primarily through Coulomb forces and radiative losses. Coulomb interaction causes excitation and ionization (secondary electrons) in the medium, leading to secondary electrons with an energy spectrum extending from a few keV to a few MeV. Some of the secondary electrons exceed the Cerenkov production threshold and therefore contribute to the Cerenkov yield. Radiative losses produce Bremsstrahlung radiation which may introduce further ionization (as explained in 1.2.5.1) which could also emit Cerenkov light (Knoll, 1988; Podgorsak, 2006). In Figure 2.9 we plotted (a) the secondary electron spectrum, (b) gamma-ray spectrum and (c) positron spectrum arising from electron interaction, which they produced in the water phantom described in section 2.2.1 from 12 MeV electron beam. The cut-off value is 0.01 mm (i.e. approximately 25 keV for electrons in water). The average number of secondary electrons was 45.68 per primary electron. The average number of secondary gammas was 1.77 per primary electron. The average number of secondary positrons was 0.0037 per primary electron. In Figure 2.9(b), the 511 keV line from positron annihilation can be recognised easily.

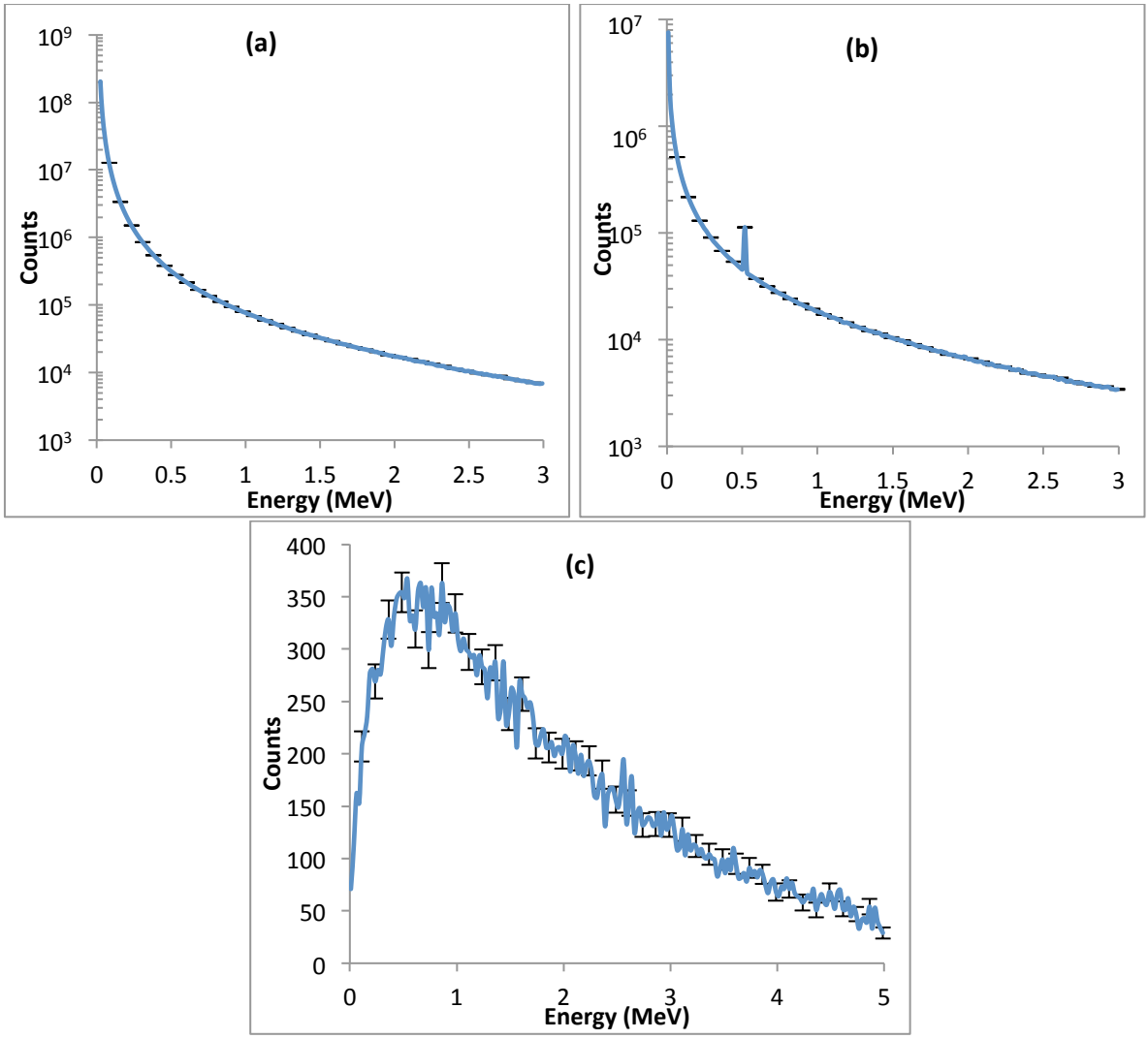

Figure 2.9 The simulated (a) secondary electron spectrum, (b) gamma-ray spectrum and (c) positron spectrum. A 10 x 10 cm^2 electron beam with energy of 12 MeV irradiated 50 x 50 x 50 cm^3 water phantom. Error-bars illustrate the statistical standard deviation of the simulation data, the error bars in (a) and (b) are smaller than the used point size.

Only 3.8% of the total secondary electrons exceed the Cerenkov emission threshold (0.27 MeV), which corresponds to 1.73 secondary electrons per primary electron. Thus, the secondary electron contribution to producing Cerenkov emission in electron therapy is important. The secondary gamma spectrum extends from a few keV to a few MeV; 15.8% of the total gamma photons have energy more than 0.422 MeV (the threshold energy of gamma to produce Compton electron via 180 degree-scatter with enough energy to produce Cerenkov light, as explained in section 1.2.5.1), which corresponds to 0.28 photons per primary electron. The ionization caused by gamma is included in Figure 2.9(a). Most of the produced secondary positrons have enough energy to produce Cerenkov emission, 93.4% of the total secondary positrons have energy more than 0.27

MeV, which corresponds to 3.4 x 10^{-3} positrons per primary electron. Therefore, positrons have a small contribution in producing Cerenkov emission in electron therapy.

2.2.3 *Cerenkov light distribution*

In order to inform the measurement of the Cerenkov emissions, Monte Carlo simulation was used to predict the light distribution around the phantom. The Cerenkov light distribution around the water phantom was found by scoring the light in the X^- and Y^- faces just after the Perspex walls. The Cerenkov light yield was scored between 400 nm and 720 nm, which corresponds to the sensitivity of commercial cameras. The refractive index and the absorption length of water and Perspex were added with a spectral resolution of 25 nm (Hale and Querry, 1973; Kasarova et al., 2007). The refractive index of air was assumed to be 1.0. The refraction and reflection effects as light travels between water, Perspex and air were included in the simulation. The position of the maximum light intensity was found by finding the depth profile of the light distribution with and without considering the boundary effect (refraction and reflection). Figure 2.10 shows the light distribution for a 9 MeV electron beam and the light distribution profiles as function of angle Θ with respect to the incident electron beam. (Helo et al., 2014d)

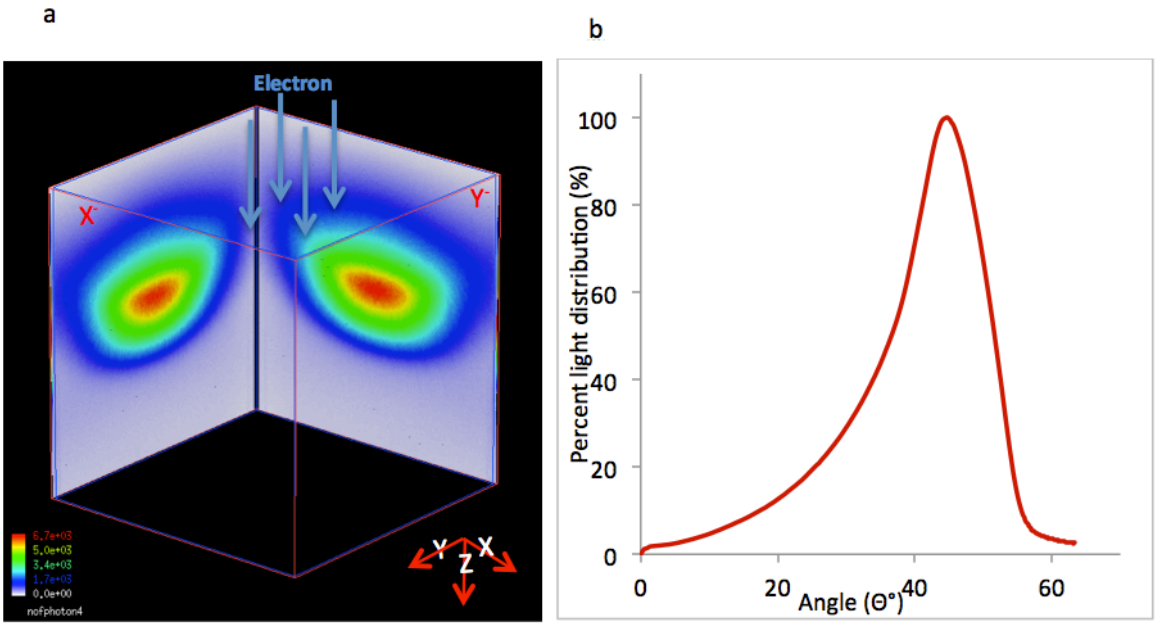

Figure 2.10 (a) Simulated 2D light distribution in a 50 x 50 x 50 cm3 water phantom irradiated by a 10 x 10 cm^2 electron beam with energy equal to 9 MeV. Refraction and reflection at boundaries were applied. The scoring area is a mesh pixelated into 0.2 x 0.2 cm^2. (b) Light distribution profile across the X- face as function of angle. (Helo et al., 2014d)

The maximum in the light distribution detected around the water phantom was found at depths of 24.4 cm and 24.8 cm for 6 MeV and 9 MeV electrons beam respectively. This corresponds to 43.6° and 44.1° with respect to the incident electron beam for energies of 6 MeV and 9 MeV respectively while the theoretical predictions for pencil beam and without considering the electron scattering is 41.4° (as shown in 1.2). The difference is because the light refraction on boundaries and the internal reflection, and electron scattering pattern in water weren't taken into account in the theoretical calculation. As expected, a more energetic electron beam shifts the maximum intensity peak deeper below the surface of the water. However, when the refraction and reflection at boundaries were neglected, the maximum in light intensity was found at angle 47.6° and 48.2° for 6 MeV and 9 MeV electron beams respectively. (Helo et al., 2014d)

2.2.4 Cerenkov production profile

To simulate the dose and Cerenkov production depth profiles, the deposited energy in the centre of the water phantom and Cerenkov light were scored within a linear array of 5 x 5 x 1 mm^3 scoring volumes [Figure 2.2(a)]. Cerenkov photons were scored in a particular volume only if they were formed in that pixel; photons travelling through a volume were ignored. The chosen scoring volume size was similar to the size of the ionization chamber used experimentally at UCLH (as explained in 2.2.1 and 1.3.1.1) to measure the PDD. (Helo et al., 2014d)

The relation between the deposited energy and Cerenkov production for a 6 MeV pencil electron beam was investigated by scoring the deposited energy and the Cerenkov light which was generated in the same volume. The simulation was repeated for field size 10 x 10 cm^2 as shown in Figure 2.11. (Helo et al., 2014d)

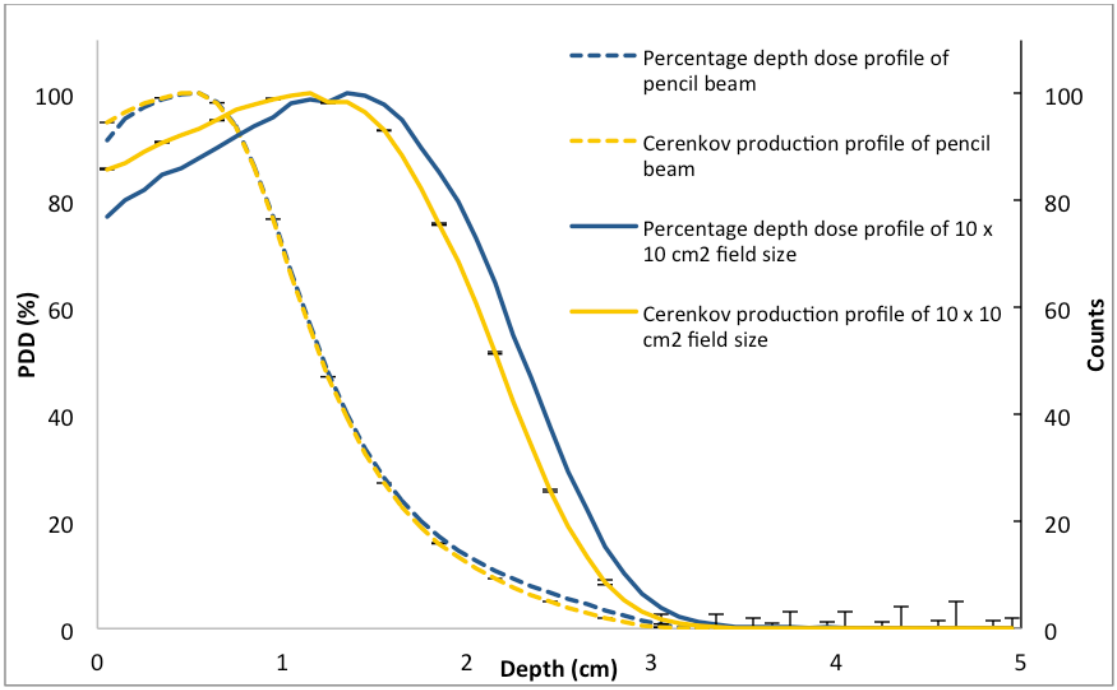

Figure 2.11 Comparison between simulated energy deposited profile and simulated Cerenkov production profile for two 6 MeV electron beams, one a pencil beam and the other with a field size of 10 x 10 cm^2. The scoring area is a 0.5 x 0.5 cm^2 square with step equal to 0.1 cm. Error-bars illustrate the statistical standard deviation of the simulation data for Cerenkov production profile. (Helo et al., 2014d)

The relation between the deposited energy and Cerenkov production for 9 MeV and 12 MeV electron beam was investigated and repeated as shown in Figure 2.12, for field size 10 x 10 cm^2.

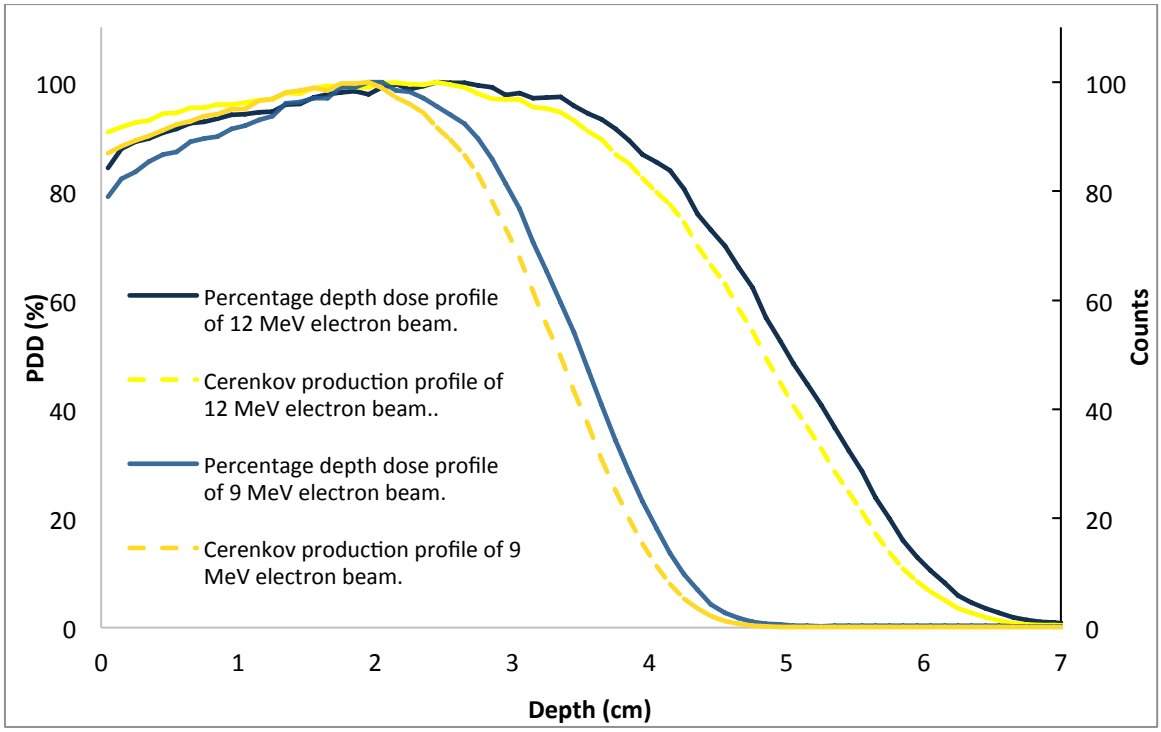

Figure 2.12 Comparison between simulated energy deposited profile and simulated Cerenkov production profile for 9 MeV electron beam and 12 MeV electron beam. The field size was 10 x 10 cm^2.

We found a very close relation between the deposited energy as a function of depth and the number of Cerenkov photons produced as a function of depth for the pencil beam of electrons. However, with a 10 x 10 cm^2 field size, the Cerenkov production profile tended to overestimate the dose at the build-up region (+9%, +8% and +7% for 6 MeV, 9 MeV and 12 MeV respectively) and it reaches a maximum at a different depth than the depth dose curve (-2 mm, -1 mm and -0.5 mm for 6 MeV, 9 MeV and 12 MeV respectively). This could be due to the simplified electron energy and divergence model used (as explained in 2.2.1) compared to the real distribution from the applicator, on the other hand the threshold of Cerenkov production, after which Cerenkov emission ceases, will slightly affect the distal tail of Cerenkov production profile.

2.2.5 An investigation of the discrepancy between the simulated Cerenkov profiles and depth dose profiles found in Figures 2.11 and 2.12

We found a very close relationship between the deposited energy and the number of Cerenkov photons as a function of depth for a pencil beam and a scoring area equal to 0.5 x 0.5 cm^2. Most of the secondary electrons produced along the beam track have energy less than Cerenkov threshold

(as found in 2.2.2), and therefore they don't contribute to Cerenkov profiles. The contributions of the secondary electrons to the total deposited energy vary with the dimension of the scoring area. In the case of a relatively small scoring area and pencil beam, it is more likely that the secondary electrons deposit their energy outside the scoring area and don't contribute to the deposited energy profiles, so the deposited energy profiles and Cerenkov profiles become similar to each other. To investigate our theory, we design a simulation where the scoring area varies between 0.5 x 0.5 cm^2 and 10 x 10 cm^2. The relation between the deposited energy and Cerenkov production profile for a 6 MeV pencil electron beam for different scoring areas is shown in Figure 2.13. The percentage contributions of the secondary electrons with energy less than 0.263 MeV and the total deposited energy as a function of scoring area were investigated as shown in Figure 2.14. Similarly, as the contributions of the secondary electrons to the total deposited energy vary with the field sizes, the previous simulation was repeated for fixed scoring area (0.5 x 0.5 cm^2) and different field sizes. The percentage contributions of the secondary electrons with energy less than 0.263 MeV and the total deposited energy as a function of field size were explored as shown in Figure 2.15.

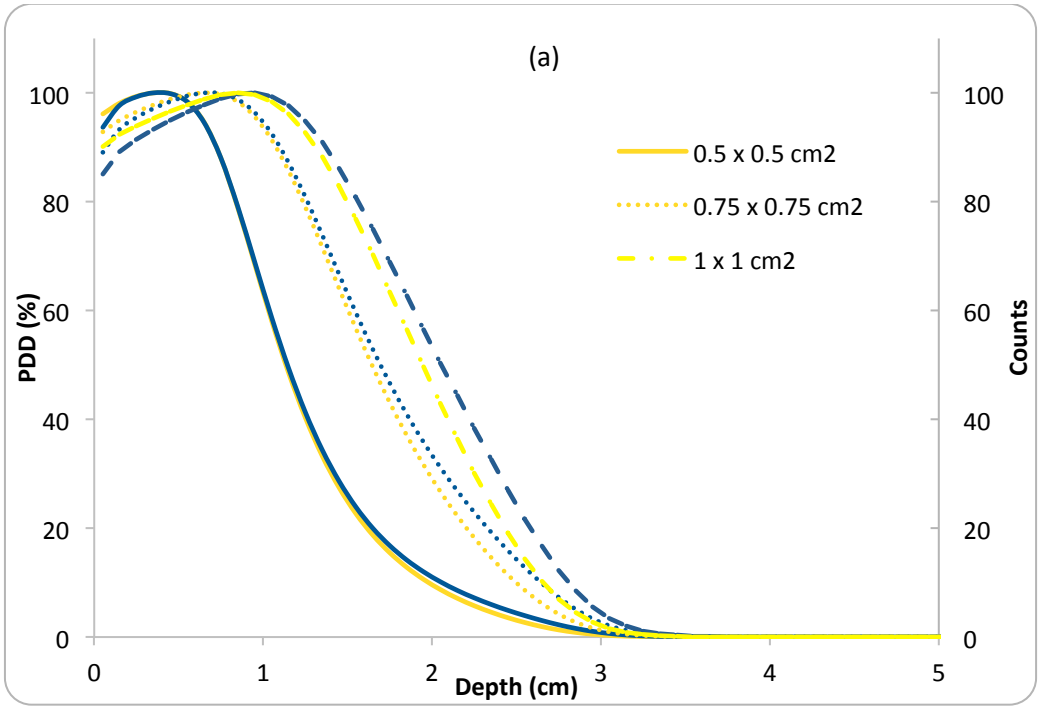

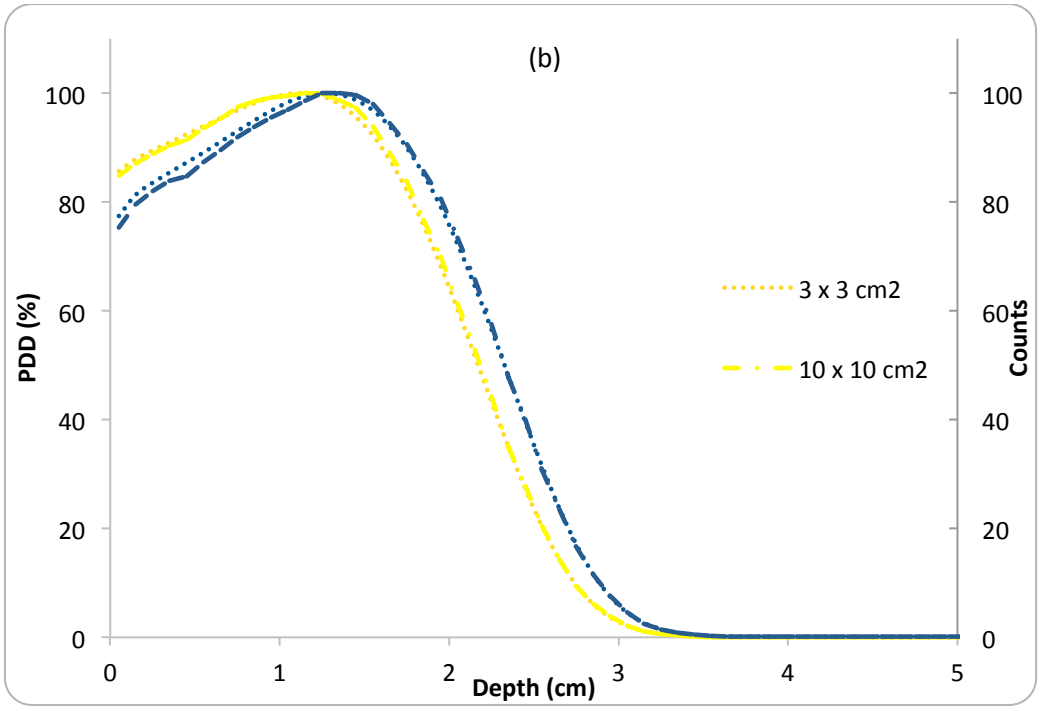

Figure 2.13 Comparison between simulated energy deposited profile (blue lines) and simulated Cerenkov production profile (yellow lines) for 6 MeV electron pencil beam. (a) The scoring area is 0.5 x 0.5 cm^2, 0.75 x 0.75 cm^2 and 1 x 1 cm^2. (b) The scoring area is 3 x 3 cm^2 and 10 x 10 cm^2.

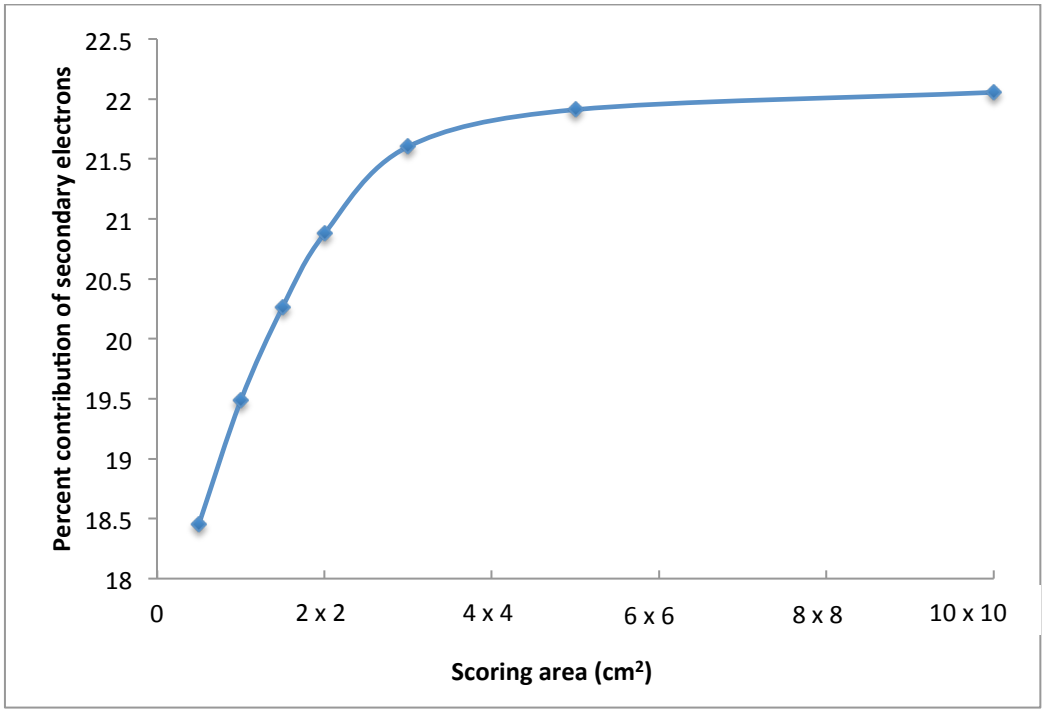

Figure 2.14 The percentage contributions of the secondary electrons with energy less than 0.263 MeV to the total deposited energy as function of scoring area

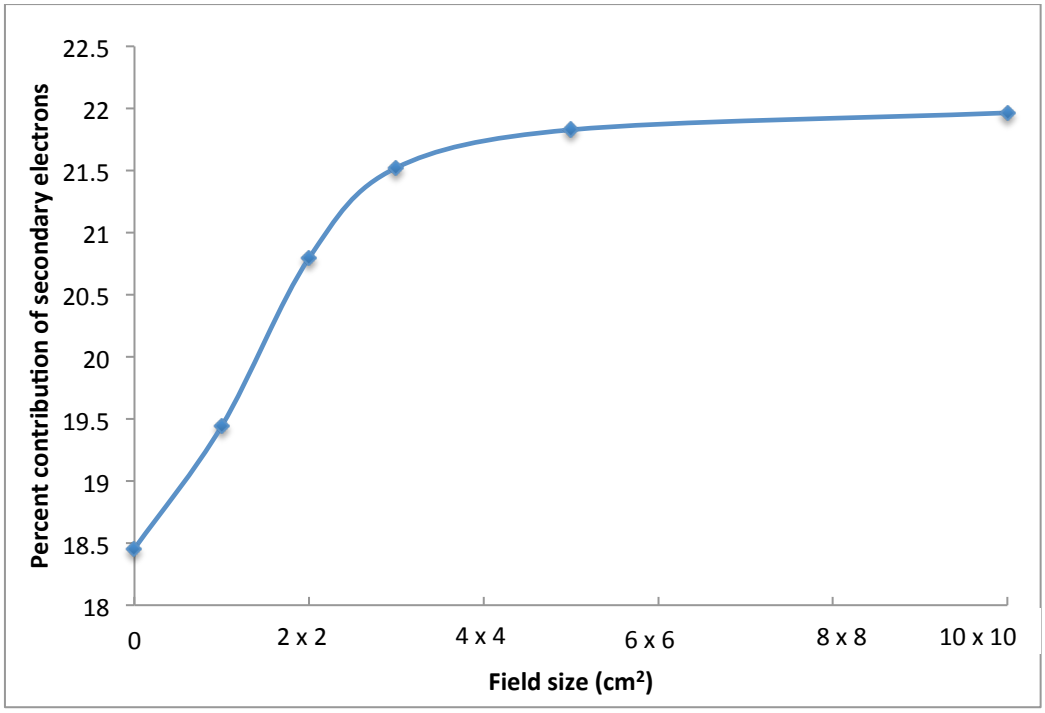

Figure 2.15 The percentage contributions of the secondary electrons with energy less than 0.263 MeV to the total deposited energy as function of field size.

The contribution of the secondary electrons that have energy less than the Cerenkov production threshold to the deposited energy profiles increased with larger scoring areas and larger field sizes. The percentage contributions of the secondary electrons increased from 18.5 % for pencil beam to 21.5 % for 3 x 3 cm^2 field size, but for larger field sizes the contribution plateaus. We believe this explains the increasing disagreement between the simulated Cerenkov profiles and depth dose profiles (Figure 2.11) at larger field sizes.

2.2.6 Pinhole code

A Nikon D70 SLR digital camera was simulated by approximating it to a pinhole camera. The advantage of simulating a pinhole camera is that it has infinite depth of field, it was not necessary to simulate the complex lens system, there is no vignetting effect, and the resolution of the image is determined solely by the dimension of the hole. The disadvantage, however, is that small aperture means that the collection efficiency is low, so the collected intensity is low unless the integration time is very long. The pinhole was a circle with radius 1 mm, and the image was projected into a sensitive 3 cm x 4 cm detector pixelated into 0.2 mm x 0.2 mm pixels. This was chosen as a

compromise between acceptable resolution and simulation time; the simulation geometry is shown in Figure 2.16. (Helo et al., 2014d)

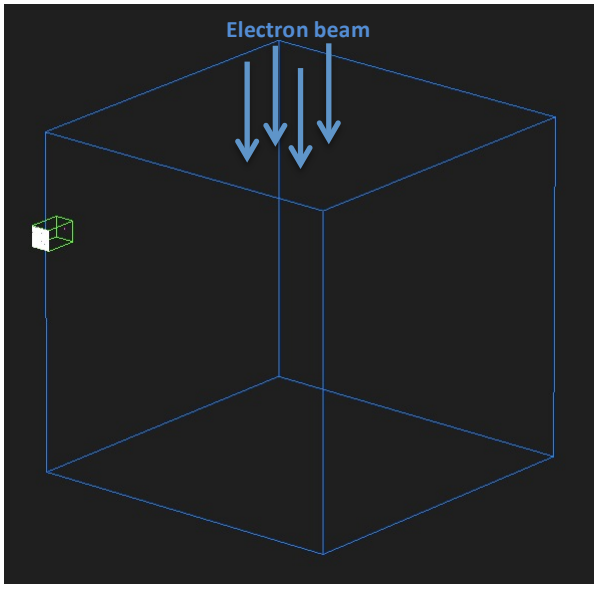

Figure 2.16 The geometry of Pinhole camera simulation, the phantom is made of 50 x 50 x 50 cm^3 of water with a wall thickness of 0.5 cm Perspex; the distance between the pinhole and the scoring volume is 5 cm (focal length); the distance between the pinhole and the central axis of the phantom is 30 cm; the diameter of the pinhole is 2 mm positioned 2 cm under the water surface. The scoring volume is a mesh pixelated into 0.2 x 0.2 mm^2.

Cerenkov light Images from a pinhole camera simulation for 6 MeV, 9 MeV and 12 MeV electron beams were modelled for 10 x 10 cm^2 field size and compared with the equivalent experimental images (the experimental images obtained by using a CCD camera, as will be explained in 3.1.3.3) as shown in Figure 2.17(a). 5 x 10^7 electrons were modelled. The beam-direction profiles in the experimental images and the simulated images were compared as shown in Figure 2.17(b), the resolution of the pinhole camera images determined by the diameter of the used pinhole. The beam-direction profiles were smoothed in Matlab by an averaging filter of 10 pixels diameter. (Helo et al., 2014d)

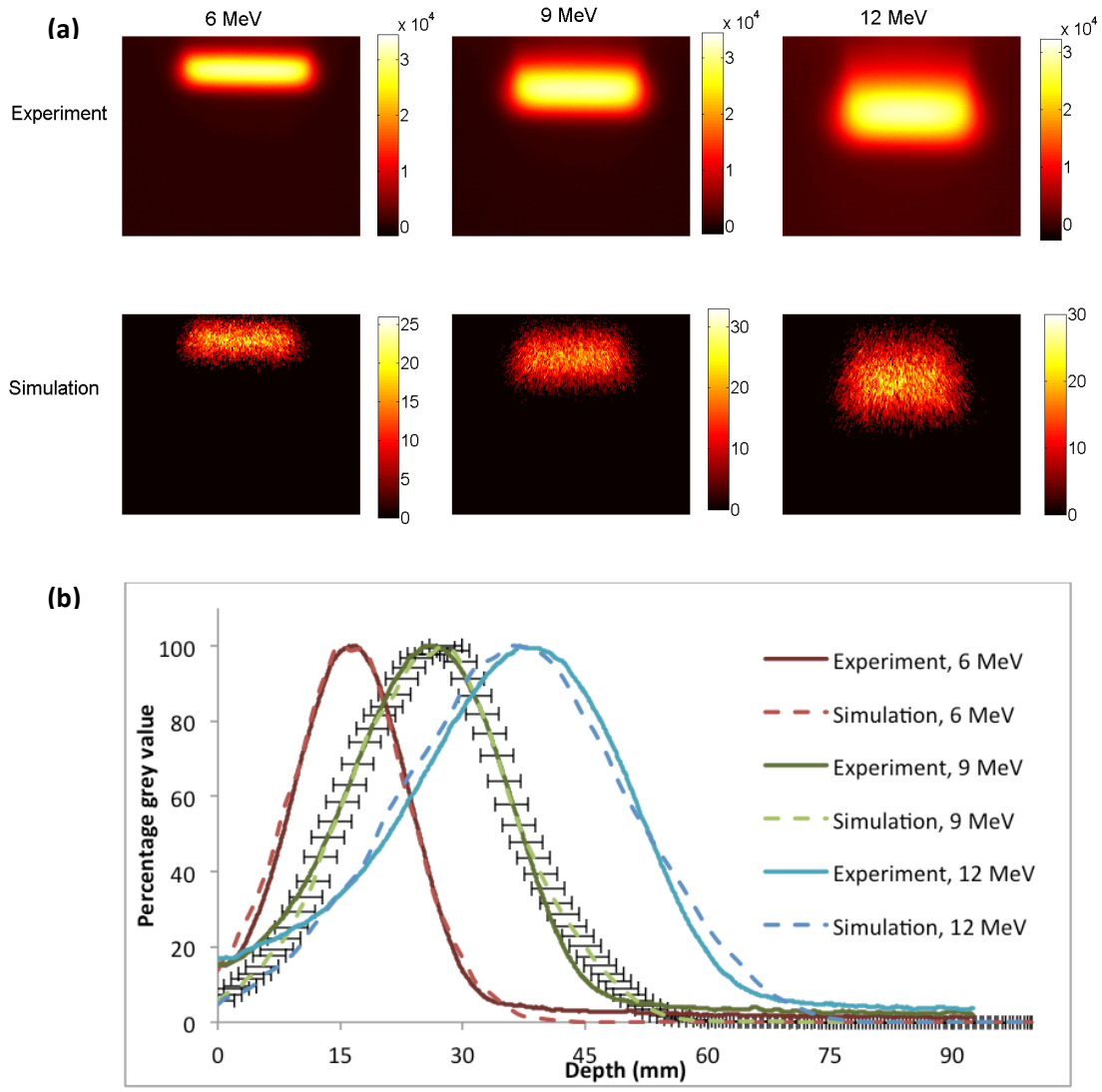

Figure 2.17 (a) Comparison of experimental Cerenkov images and pinhole camera simulations for 6, 9 and 12 MeV electron beams. Experimental measurements were executed with 10 x 10 cm^2 field size, 200 MU dose and 600 MU/min dose rate, more information about the experiment setup and the used camera can be found in 3.1.2. (b) Beam-direction profiles for experimental and simulation Cerenkov images for a 10 cm x 10 cm field size. The error bars are due to the diameter of the pinhole and the pixel size, and are illustrated just for 9 MeV electron beam. (Helo et al., 2014d)

Cerenkov light Images from pinhole camera simulation for 12 MeV electron beams were modelled for 6 x 6 cm^2 and 10 x 10 cm^2 field size and compared with the equivalent experimental images. The cross-line profile in the experimental images and the simulated images were compared as shown in Figure 2.18.

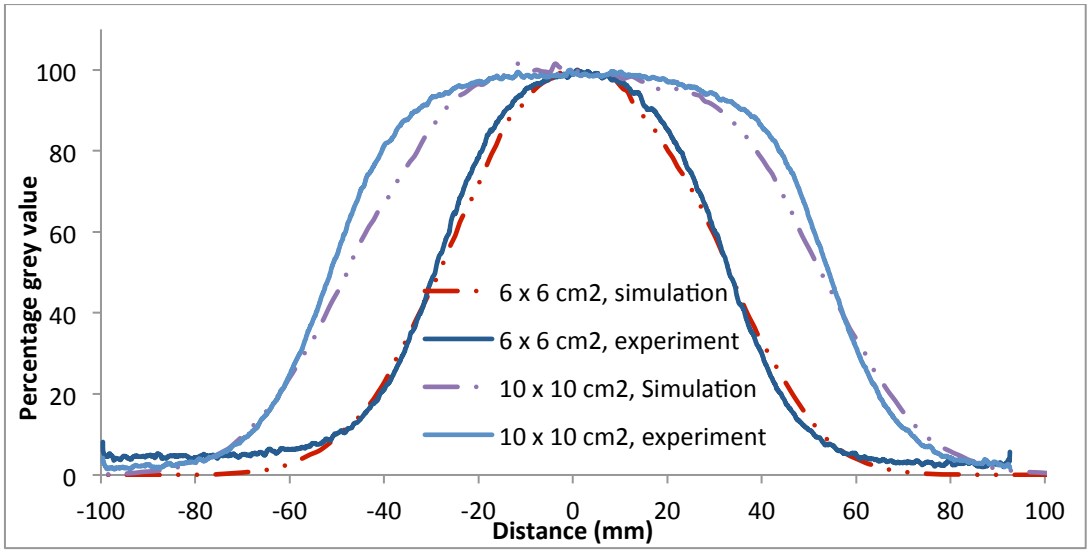

Figure 2.18 Crossbeam profiles for experimental and simulation Cerenkov images for a 6 cm x 6 cm and 10 cm x 10 cm field sizes.

Modelling the camera as a pinhole allowed us to simulate the complex lens-camera combination. We were able to reproduce the experimental Cerenkov images taken in UCLH for different energies and different field sizes within 2 mm accuracy apart from the shoulders of the crossbeam profiles. The statistics in the simulated images were not satisfactory because of the low number of photons detected (77610 photons for 12 MeV electron energy and 10 x 10 cm^2 field size) and the long-time of the simulation (almost 2 weeks). To increase the number of photon detected by the pinhole camera, we could either increase the pinhole diameter, which affects the spatial resolution, or increase the initial number of electrons, which affects the computing time. (Helo et al., 2014d)

2.2.6.1 Magnification effect simulation

The unequal magnification effects associated with imaging beams with practical field sizes were studied. Cerenkov images are a projection of a 3-D field onto a 2-D plane, which causes image distortion. The geometry and intensity projections depend on the beam field size and the acceptance angle of the camera. (Helo et al., 2014d)

The magnification effect can be illustrated by considering a uniform 3D cubic light source in the middle of the water phantom [Figure 2.19(a)]. For any plane parallel to the beam direction, the relative intensity of the image can be calculated by:

$$\frac{I`}{I} = \frac{r^2}{(r+x)^2} \quad (2.16)$$

The relative magnification effect in one dimension can be calculated by:

$$\frac{y`}{y} = \frac{r+x}{r} \quad (2.17)$$

Where:

x: the distance between a given projection and the midline projection.

r: the distance between midline projection and the projection plane.

I: the intensity of the image of the midline projection.

I': the intensity of the image of the given projection at distance x.

y: the width of the midline projection.

y': the width of a given projection.

By summing the contributions of all the projections of light sources for three different cube sizes (6 x 6 cm^2, 10 x 10 cm^2 and 15 x 15 cm^2), and normalising at the centre of each summed projection, one gets the results shown in Figure 2.19(b). This figure shows: (i) the sharp edge of the original light source projects as a slanting penumbra; (ii) the slant of the penumbra is somewhat dependent on the size of the cube and (iii) the FWHM width of the penumbra coincides with the actual width of the light cube. These effects apply both in the beam-direction and in the cross- beam profile. No attempt was made to correct the measured data for this effect; the above analysis should help the understanding of the influence of this effect on the results. (Helo et al., 2014d)

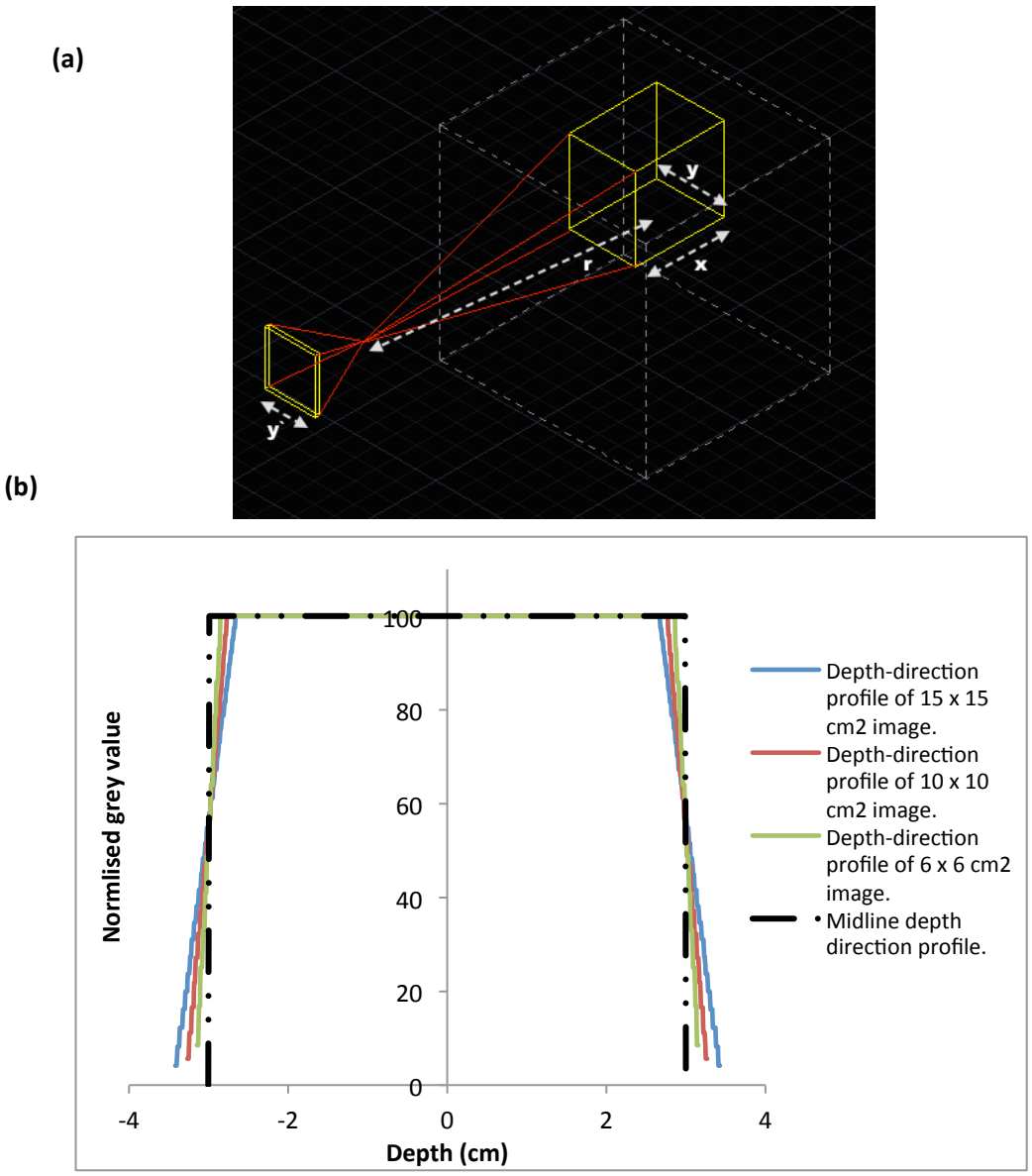

Figure 2.19 (a) Geometrical magnification and inverse square law effects on projection of a 3D light cube, as described in the text. (b) Magnification and inverse square law effects on projection of the 3D cubic uniform light source described in Fig. 2.19(a). (Helo et al., 2014d)

2.3 Proton beam simulation

A clinical proton beam entering a water phantom was simulated using a Monte Carlo simulation to explore the different sources of Cerenkov emissions in proton therapy. A simulation was performed of the deposited energy and of Cerenkov production in water. Monte Carlo simulation was used to predict the measured light distribution around the water phantom, to find the relation between deposited energy, Cerenkov production and the depth distribution of different radionuclides. A simple model of the human eye was simulated to predict the light distribution in the retina. All

simulations used 10^8 protons unless stated otherwise. In Geant4, a cut-off value of 0.01 mm (i.e. approximately 0.025 MeV for electrons in water) was chosen below which the particle is no longer assumed to produce secondary particles. (Helo et al., 2014a, 2014e)

2.3.1 Monte Carlo code validation

2.3.1.1 Pristine Bragg peak and spread out Bragg peak (SOBP) simulations

The dose deposited and Cerenkov light distribution were modelled using a Monte Carlo simulation of a clinical proton beam with realistic proton energy spectrum and beam divergence. The simulation was fine-tuned and validated by comparing the calculated proton dose distributions in water against measurements made during beam quality assurance (QA) measurements at the Clatterbridge Cancer Centre with a flat ion chamber (Classic Markus, PTW-Freiburg) which has a sensitive diameter of about 3.5 mm, and a very thin window of <0.1 mm polythene. A circular proton beam of diameter 2.5 cm and 60 MeV energy was simulated to irradiate a 5 x 5 x 5 cm^3 water phantom. Figure 2.20(a) shows the geometry of the simulation and the scoring volumes of depth dose profile for pristine Bragg peak. (Helo et al., 2014a)

A simulated Spread-Out Bragg Peak (SOBP) was composed of 24 pristine Bragg peaks from 59.8 MeV to 16 MeV in 2 MeV intervals, with different intensities. This approximates the range modulator wheel steps used at Clatterbridge for the experiments. Figure 2.20(b) shows the geometry of the simulation and the scoring volumes of depth dose profile for SOBP.

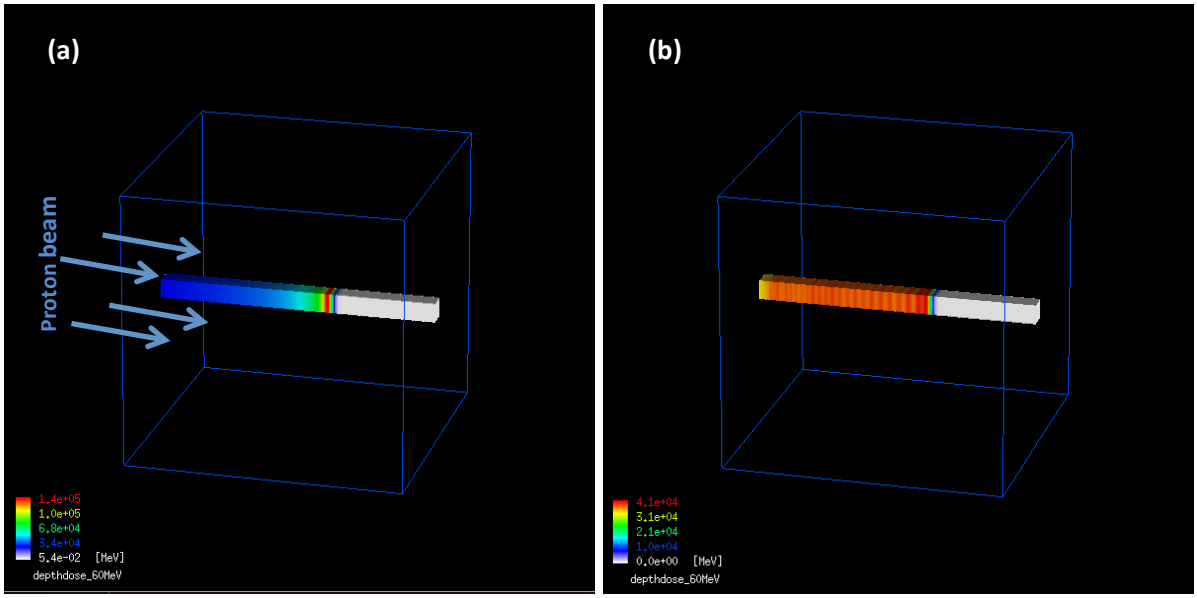

Figure 2.20 Simulation of circular proton beam with diameter of 2.50 cm, the phantom is made of 5 x 5 x 5 cm^3 of water; the scoring volume is a square 3.5 x 3.5 mm^2 with step equal to 0.1 mm. The phantom-collimator distance is 5 cm; the standard deviation of the beam angular profile is 0.1 degree. (a) The pristine proton energy spectrum is Gaussian with very long tail, the centred energy of the Gaussian is 60.1 MeV and FWHM equal to 0.71 MeV (standard deviation equal to 0.3 MeV). (b) The SOBP was composed of 24 Bragg Peaks from 59.8 MeV to 16 MeV in 2 MeV intervals, with different intensities.

The energy distribution of a 60 MeV proton beam was simulated as a Gaussian energy spectrum with centre energy 60.1 MeV and standard deviation (σ) 0.3 MeV, in addition to a very long tail; a Gaussian angular distribution was fine-tuned in the simulation to match the simulated depth doses to ionization chamber measurements. The beam divergence (sigma) of all beams was 0.1 deg. Figure 2.21(a) illustrates a comparison of the depth dose profile of 60 MeV proton beam between ionization chamber measurement and Monte Carlo simulation. Figure 2.21(b) shows a comparison of the depth dose profile of SOBP between ionization chamber measurement and Monte Carlo simulation. (Helo et al., 2014a)

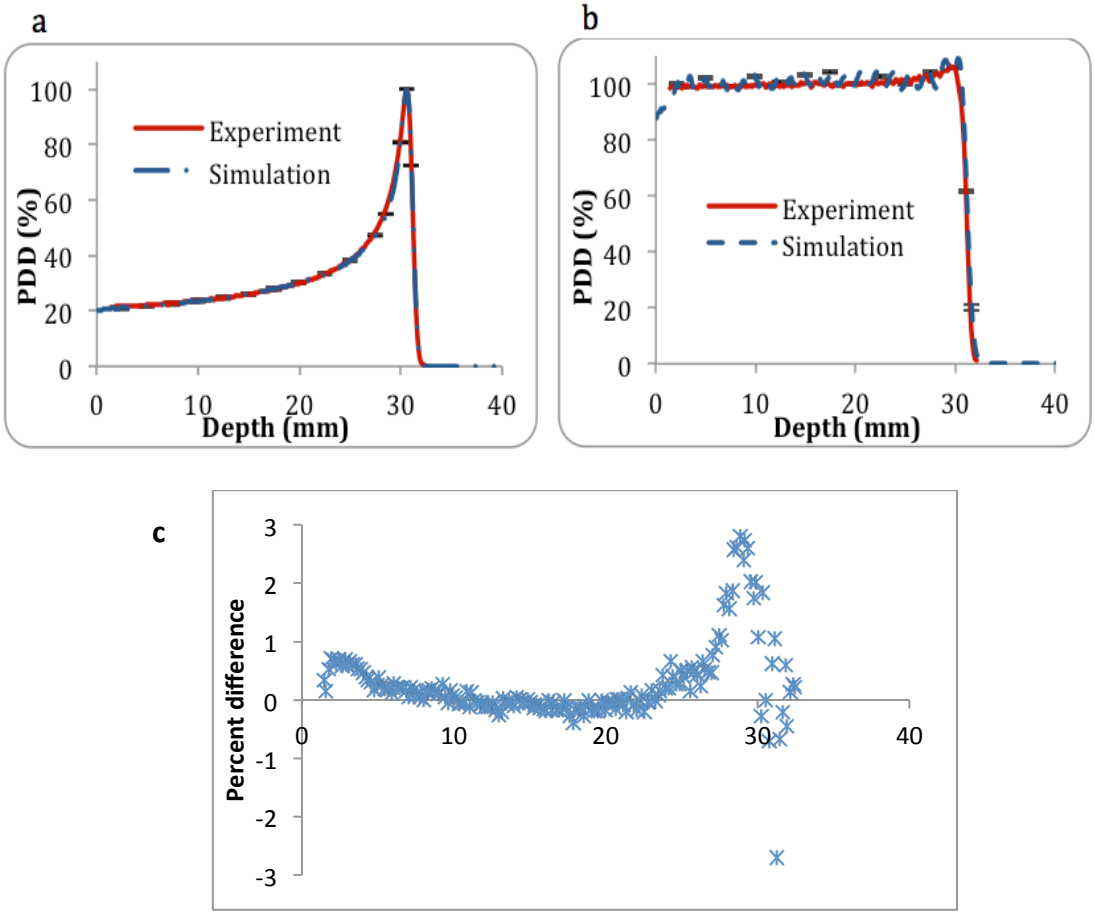

Figure 2.21 (a) Comparison of depth dose profile between Markus ionisation chamber measurement and Monte Carlo simulation, the scoring volume is a square 3.5 x 3.5 mm^2 with step equal to 0.1 mm. (b) SOBP simulated using Monte Carlo and measured using an ionization chamber. The typical standard error in the experimental data was 0.17 mm. Error-bars illustrate the statistical standard deviation of the simulation data. (c) The percentage difference of the experimental and simulated depth dose profiles of the pristine 60 MeV Bragg peak. (Helo et al., 2014a)

We found that the Gaussian function with very long tail satisfactorily reproduces the measured data. This fit very well with previous spectroscopy measurement done in Clatterbridge centre using a plastic scintillator (NE102a) (Kacperek and Bonnett, 1990). Nevertheless, we found that the measured spectrum has a larger FWHM (1.0 MeV) than that which we used in our simulation (0.71 MeV) and we conclude that the NE102a system may increase the apparent FWHM of the proton spectrum. NE102a is an organic polymer scintillator made of Polyvinyl toluene (PVT) with refractive index 1.58 and density 1.032 g/cm^3 (Torrisi, 1998). PVT detectors are inexpensive, easily fabricated in large volume and they can be made to be quite sensitive to radiation; but PVT detectors have very poor energy resolution (Portals et al., 2011). The resolution of the plastic scintillator depends on (1) the internal refraction of the light; (2) pulse pile-up (coincident pulses distort the recorded energy spectrum) (Taguchi et al., 2010); (3) quenching effect, which cause non-linearity in the

scintillator response, results in general broadening of the spectra (Knoll, 1988). It was noted during the experiment in Clatterbridge centre that larger collimators gave a larger FWHM, which indicates that the measurement depends on the beam field size.

2.3.1.2 Lateral profile simulation

The geometry of the simulated lateral proton beam profile and the scoring volumes are shown in Figure 2.22(a). A comparison of the lateral profile of the simulated and experimental pristine Bragg peak, at the depth of the Bragg peak in water (3.05 cm) against film measurements is shown in Figure 2.22(b).

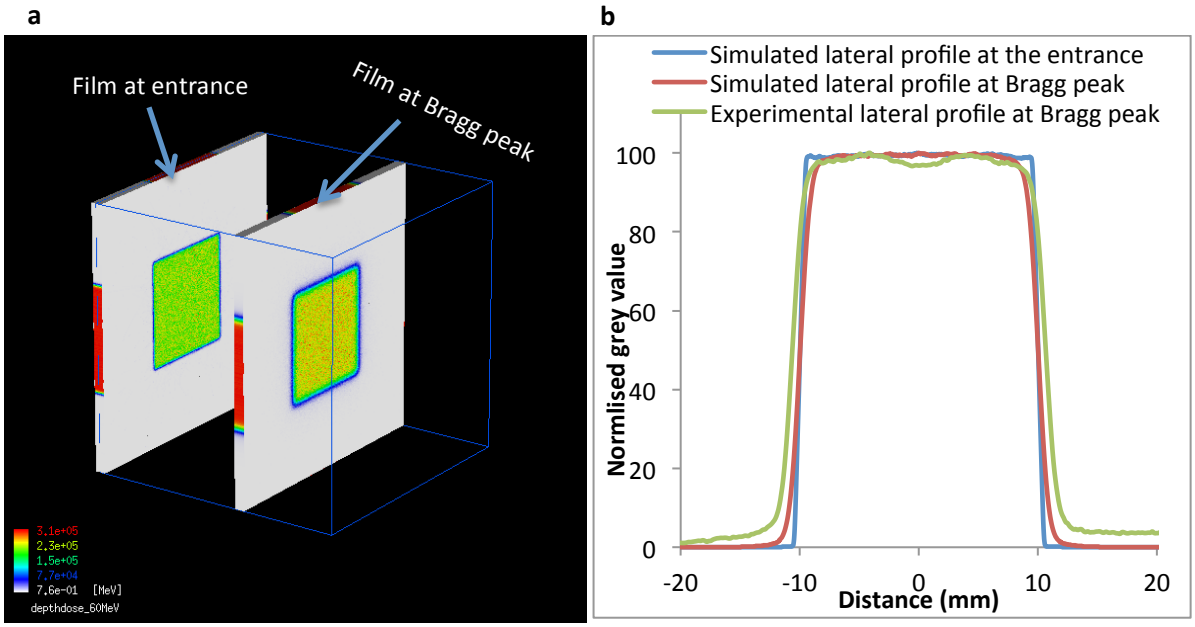

Figure 2.22 (a) Simulation of square proton beam with dimension of 20 x 20 mm^2, the phantom is made of 5 x 5 x 5 cm^3 of water, the collimator-film distance is 2.95 and 6 cm respectively (at the entrance of the beam and at Bragg peak position), the film is a square of 5 x 5 cm^2 with resolution equal to 0.05 mm. The standard deviation of the beam angular profile is 0.1 degree. (b) A comparison between simulated and experimental lateral proton beam profile. In the experimental measurement a collimator of 20 x 20 mm^2 was used, and a film scanned with resolution equal to 150 dpi (equal to 0.169 mm), the collimator film distance is 6 cm. The film was placed behind a plastic phantom and at Bragg peak position. For simulation, the primary proton beam energy was assumed to follow a Gaussian function with long tail as explained in 2.3.1.1.

The depth dose profile and transverse profile generated by Monte Carlo simulation for a pristine 60 MeV Bragg peak and a SOBP reproduced data measured with an ionization chamber and film to

within 3%. This could be due to the simplified proton energy and divergence model used compared to the real distribution from the cyclotron.

2.3.1.3 Nuclear cross-section verification

The production cross-section of the different nuclear reactions induced by a proton beam in water was computed using a homogeneous medium of ^{16}O where the incident particle is terminated at the first interaction and the electromagnetic processes were not considered. Then the cross-sections of different radionuclides were compared with ENDF (B-VII.1, 2011) nuclear database library (Chadwick et al., 2011). The production cross-section of oxygen-15 and carbon-11 are presented in Figure 2.23(a) and 2.23(b) respectively.

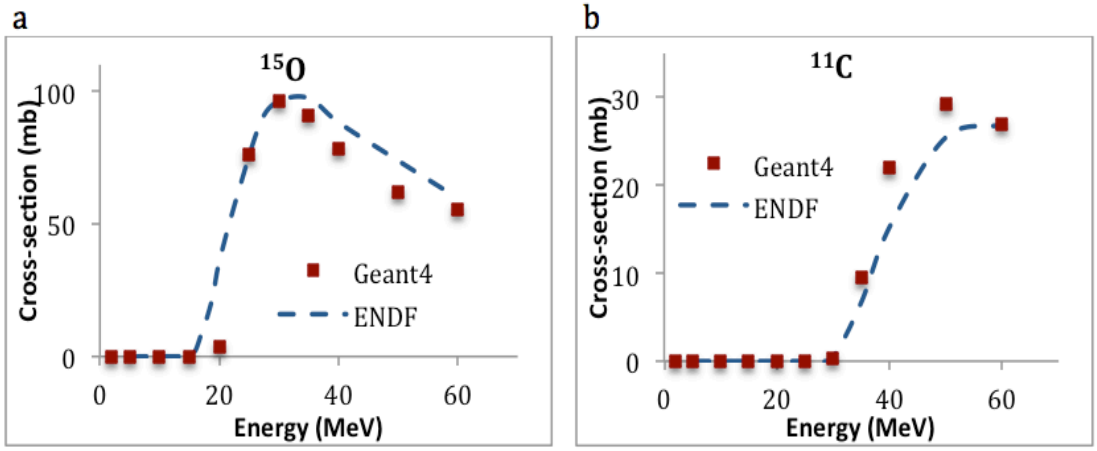

Figure 2.23 Comparison of production cross-sections between ENDF database library and Monte Carlo simulation for (a) ^{15}O isotopes and (b) ^{11}C isotopes.

The computed cross-sections of the most important radionuclides (^{15}O, ^{11}C, ^{13}N, ^{17}F, ^{10}C, ^{14}O and ^{7}Be) (Beebe-Wang et al., 2003) agreed with the ENDF data to within 15% except for the direct capture reaction ^{16}O (p,γ)^{17}F, where the simulated production cross-section of fluorine 17 overestimates the ENDF data; thus the ^{17}F contribution in Cerenkov production was excluded in this study. ^{15}O and ^{11}C are the most abundant isotopes in water as they have high production cross-sections (Chadwick et al., 2011).

2.3.1.4 Radioactivity implementation

In order to verify the radioactivity implementation in our code, we simulated a fluorine 24 isotope (^{24}F) placed in the centre of the previous phantom. ^{24}F has a probability to decay with β^- and half-life 400 ms to ^{24}Ne which itself has a probability to decay with β^- and half-life 3.38 minutes to ^{24}Na which may then decay with β^- and half-life 14.96 hours to ^{24}Mg which is stable (L'Annunziata, 2007). Figure 2.24(a) shows the radioactivity decay rate of fluorine 24 individually (i.e. ^{24}F to ^{24}Ne) and the radioactivity of the complete chain of the three decays (i.e. ^{24}F to ^{24}Mg) as shown in 2.24(b). The half-life of the decays was calculated by fitting an exponential curve to the simulated data. The radioactivity of a chain of any number of decays required a complicated algebra solution (Bateman's equations) (L'Annunziata, 2007). However, because of the half-life of sodium 24 is large (14.96 hours) compared to fluorine 24 and neon 24, it is expected that the half-life of sodium 24 will dominate the complete decay process.

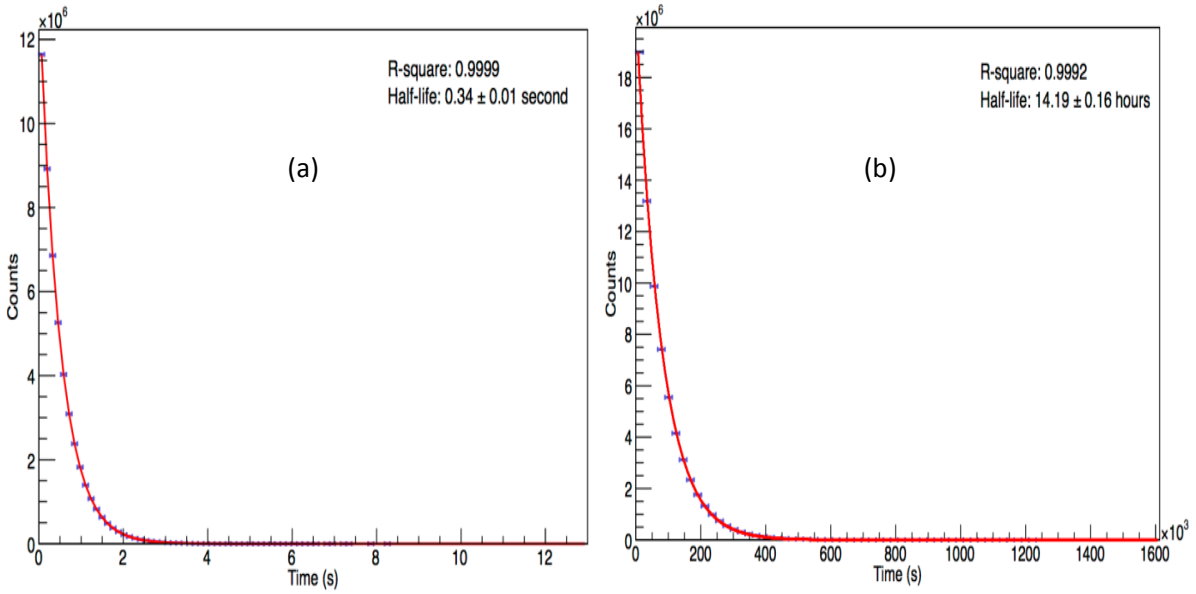

Figure 2.24 The simulated radioactivity decay rate of (a) Fluorine 24 individually and (b) the complete chain. The half-life was calculated by fitting an exponential curve. Simulations used 10^6 fluorine 24 isotopes. Error-bars illustrate the statistical standard deviation of the simulation data.

We were able to identify all radioactive products resulting from fluorine 24 decay chain accurately. The simulated half-life of fluorine 24 decay is reasonably close to the theoretical value of 400 ms.

2.3.2 The secondary emissions in proton therapy

A proton beam loses its energy mainly by Coulomb interactions, which yield free electrons. Protons may also lose energy by non-elastic nuclear interactions, which yield either uncharged particles (neutrons or photons) or heavy charged particles (like deuterons and alphas). Radioactive nuclei are produced along the beam path due to non-elastic interactions as explained in 1.2.4.1.

The contribution of the secondary particles in Cerenkov production was investigated for the 60 MeV proton beam described in 2.3.1.1 by plotting the energy spectrum of the secondary protons, neutrons, gammas, electrons and positrons at a resolution of 0.01 MeV. All simulations used 10^8 protons.

2.3.2.1 Secondary proton spectrum

In order to estimate the contribution of secondary protons to the Cerenkov production, the energy spectrum of proton emissions up to 60 MeV was simulated, as shown in Figure 2.25. On average, we found 0.07 secondary protons were produced per primary proton.

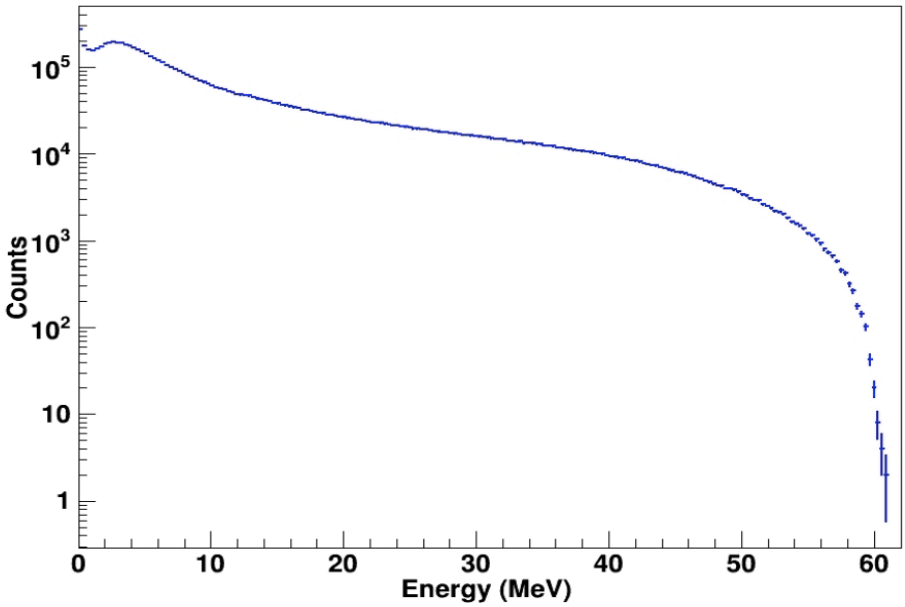

Figure 2.25 The simulated secondary proton spectrum. The phantom was irradiated by a 60 MeV circular proton beam with diameter of 2.50 cm. The error bars (illustrating the statistical standard deviation) are smaller than the point size in some points of the curve.

We found that the secondary proton spectrum extends up to 60 MeV for a primary beam energy of 60 MeV. The secondary protons interact with water molecules as the primary protons do, as described in 1.2.4.1.

2.3.2.2 Secondary electron spectrum

In order to estimate the contribution of secondary electrons to the Cerenkov production, the energy spectrum of electron emissions up to 10 MeV was simulated, as shown in Figure 2.26. On average, we found 203.46 secondary electrons were produced per primary proton.

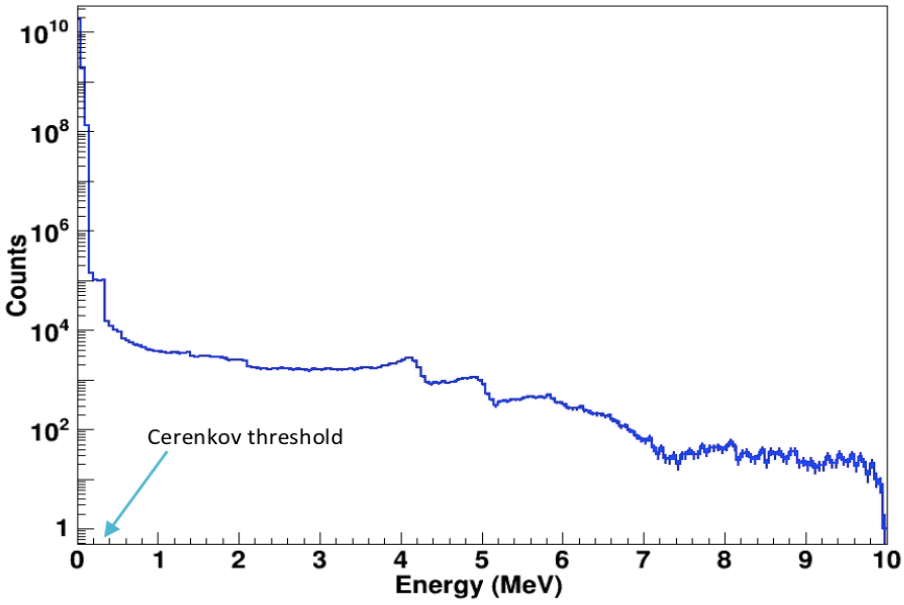

Figure 2.26 The simulated secondary electron spectrum. The phantom was irradiated by a circular proton beam with diameter of 2.50 cm. The error bars (illustrating the statistical standard deviation) are smaller than the point size in some points of the curve.

We found that the secondary electron spectrum extends up to a few MeV. Most of the secondary electrons (Compton electrons) do not exceed the Cerenkov production threshold. Only 0.002% of the total secondary electrons pass the Cerenkov emission threshold (0.27 MeV), which corresponds to 0.005 secondary electrons per primary proton.

2.3.2.3 Secondary gamma emission spectrum

In order to estimate the contribution of gamma ray photons to the Cerenkov production the energy spectrum of gamma emissions up to 20 MeV was simulated, as shown in Figure 2.27 (see also (Bom et al., 2012; Polf et al., 2013)). On average, we found 0.27 gamma photons were produced per primary proton (agreeing with previous work which reported values of between 0.15 and 0.33 gamma photons per proton, depending on the energy of the primary proton (Bom et al., 2012; Fiedler et al., 2011)). (Helo et al., 2014a)

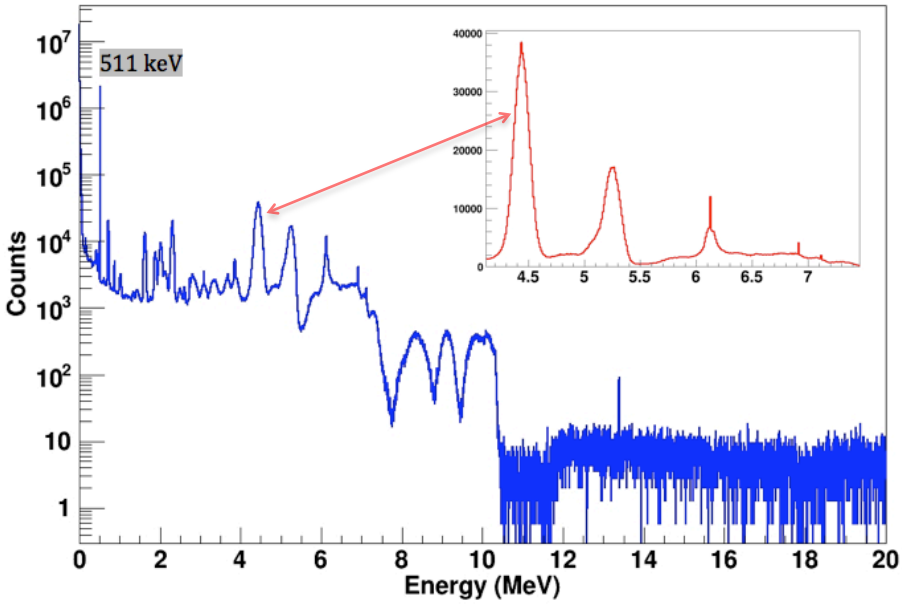

Figure 2.27 The simulated secondary gamma spectrum. The phantom was irradiated by a circular proton beam with diameter of 2.50 cm. The error bars (illustrating the statistical standard deviation) are smaller than the point size in some points of the curve. (Helo et al., 2014a)

The gamma emission spectrum shows the 0.511 MeV peak from positron-electron annihilation. The de-excitation nuclear lines of oxygen, carbon and nitrogen are also visible (4.44 MeV emission from ^{12}C, 5.27 MeV emission from ^{15}N and 6.13 MeV, 6.92 MeV and 7.12 MeV emissions from ^{16}O nuclei are highlighted). Oxygen peaks are much narrower than those from carbon and nitrogen, which is explained by Doppler broadening having more influence on the lighter carbon nuclei and nitrogen nuclei emissions than oxygen emissions (Polf et al., 2013). (Helo et al., 2014a)

Secondary gamma spectrum extends up to few MeV; 17.8% of the total gamma photons have energy more than 0.422 MeV (the threshold energy of gamma to produce Compton electron via

180°-scatter with enough energy to produce Cerenkov light, as explained in 1.2.5.1), which corresponds to 0.05 photons per primary proton.

2.3.2.4 Secondary neutron emission spectrum

In order to estimate the contribution of neutrons to the fast component of Cerenkov production, the energy spectrum of neutron emissions up to 60 MeV was simulated as shown in Figure 2.28. On average, we found 0.01 neutrons produced per primary proton.

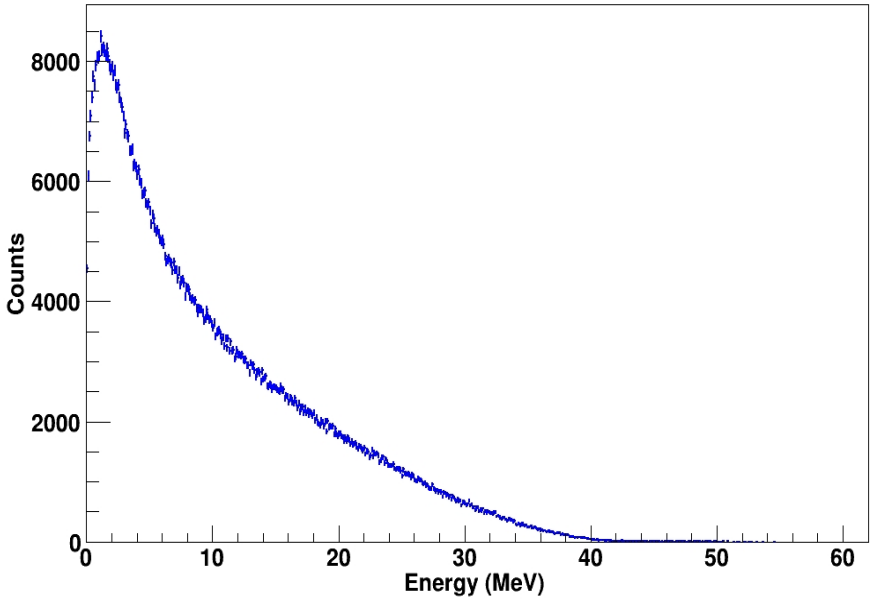

Figure 2.28 The simulated secondary neutron spectrum. The phantom was irradiated by a circular proton beam with diameter of 2.50 cm. The error bars (illustrating the statistical standard deviation) are smaller than the point size in some points of the curve.

The neutron emission spectrum shows a continuum ranging up to 42 MeV. Cerenkov emissions by neutrons in water are explained in 1.2.5.2.

2.3.2.5 Radioactivity and secondary positron spectrum

Radioactivity introduced to the water phantom by proton nuclear interactions was simulated. Different isotopes produced in water were identified with their percentage composition, along with the decay emission spectrum, the half-life and the average number of Cerenkov photons produced by each isotope as shown in Table 2.1. (Helo et al., 2014a)

Table 2.1 The most abundant positron emitters found in water after simulated irradiation by a 60 MeV proton beam; p: proton, n: neutron, α: alpha particles. 10^7 protons were fired.

Symbol	Nuclear Reactions	Decay mode	Daughter	Half-life	Nuclides per 10^7 protons
^{15}O	$^{16}O(p,pn)^{15}O$ (1)	β^+	^{15}N	122.24 s	81207
^{11}C	$^{16}O(p, \alpha pn)^{11}C$ (2)	β^+	^{11}B	20.33 min	23057
^{10}C	$^{16}O(p,3p4n)^{10}C$	β^+	^{10}B	19.29 s	690
^{13}N	$^{16}O(p,\alpha)^{13}N$	β^+	^{13}C	9.96 min	2798
^{14}O	$^{16}O(p,p2n)^{14}O$	β^+	^{14}N	70.598 s	337
^{14}C	$^{17}O(n, \alpha)^{14}C$	β^-	^{14}N	5.73 x 10^3 year	970
^{7}Be	$^{16}O(p, 5p5n)^{7}Be$ (3)	EC	^{7}Li	53.22 d	2586

(1) p + n includes deuteron (d)
(2) 2p + 2n includes alpha (α)
(3) p +2n includes triton (t)

The most abundant β^+ emitters found in this work and in similar work were ^{15}O and ^{11}C (Beebe-Wang et al., 2003; Vynckier et al., 1993).

The simulated energy spectrum of positron emissions up to 3 MeV is shown in Figure 2.29. On average, we found 0.01 positrons produced for each primary proton.

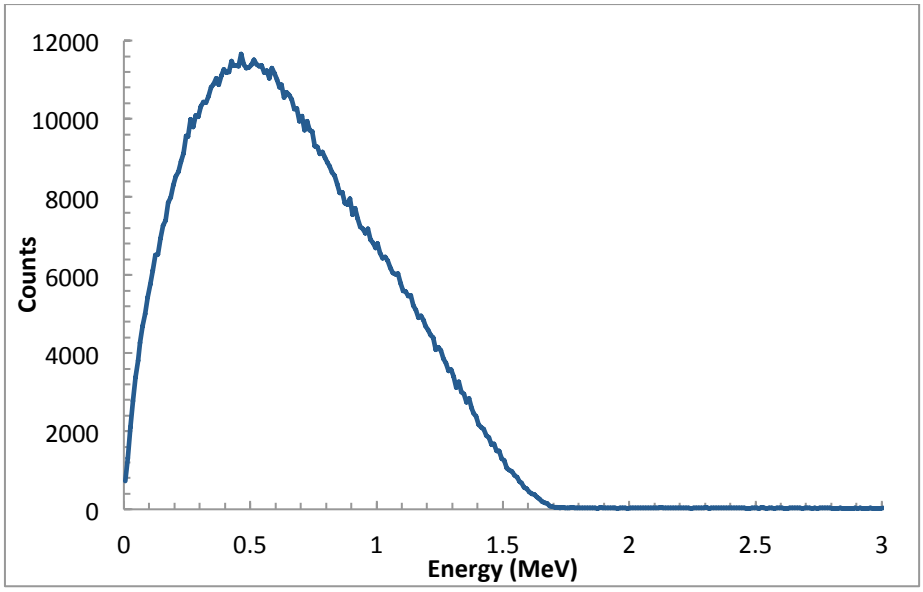

Figure 2.29 The simulated secondary positron spectrum. The phantom was irradiated by a circular proton beam with diameter of 2.50 cm. The error bars (illustrating the statistical standard deviation) are smaller than the point size in some points of the curve. (Helo et al., 2014a)

As expected (the production cross-section of ^{15}O is higher than other isotopes cross sections (section 2.3.1.3)), positron emission from ^{15}O (with maximum positron energy equal to 1.72 MeV as shown in Table 1.2) dominates the total positron emission spectrum, and the plot agrees qualitatively with that published by (Tuckwell and Bezak, 2007) for the decay of ^{15}O to ^{15}N. (Helo et al., 2014a)

Secondary positrons spectrum extends from a few eV to few MeV; 86.5% of the total positrons have energy more than 0.27 MeV, which corresponds to 0.009 positrons per primary proton.

2.3.3 Cerenkov light distribution

In order to optimize the measurement of the Cerenkov emissions, Monte Carlo simulation was used to predict the light distribution passing through the top face of the phantom. The Cerenkov light distribution was found by scoring the light in the Z^- plane just after the water phantom wall (Figure 2.30(a)). The Cerenkov light yield was scored between 400 nm and 720 nm which is the visible range, and the range to which digital consumer CCD cameras are sensitive. The wavelength-dependent refractive index and absorption length of water and Perspex were added with a spectral resolution of 25 nm (Kasarova et al., 2007). The refractive index of air was assumed to be 1.0. The

refraction and reflection effects as light travels between water, Perspex and air were included in the simulation. (Helo et al., 2014a)

The position of the maximum light intensity was found by finding the depth profile of the light distribution with and without considering the boundary effect (refraction and reflection). Figure 2.30(b) shows the light distribution for a 60 MeV proton beam and the light distribution depth profile as function of distance.

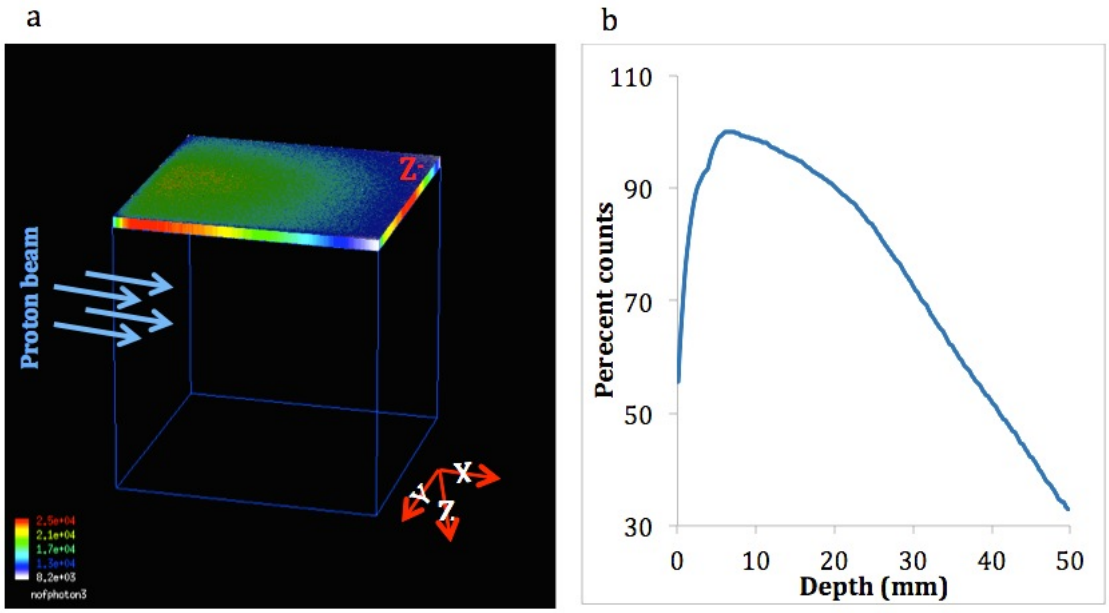

Figure 2.30 (a) Simulated 2D light distribution in a 5 x 5 x 5 cm^3 water phantom irradiated by a 60 MeV proton beam with diameter of 2.50 cm. Refraction and reflection at boundaries were applied. The scoring area is a mesh pixelated into 0.2 x 0.2 mm^2. (b) Light distribution profile across the Z- face as function of distance. The profile was smoothed in Matlab by a moving average filter of 15 pixels diameter. (Helo et al., 2014a)

The maximum in the light distribution detected above the water phantom was found at distance of 0.6 cm and 0.5 cm for pristine Bragg peak and SOBP respectively away from the water phantom wall. The maximum in light intensity found at distance 1.7 cm and 1.3 cm for pristine Bragg peak and SOBP respectively, when the refraction and the total internal reflection at boundaries were being discarded.

2.3.4 Cerenkov production profile

Light emission in proton therapy was simulated and two different components of Cerenkov emission were identified: *(1)* a fast component, which is Cerenkov emission from prompt gamma (as described in section 1.2.5.1) and neutron interactions (as described in section 1.2.5.2); and *(2)* a slow component, which is Cerenkov emission from positrons and electrons emitted by radioactive decay. (Helo et al., 2014a)

To simulate the dose and Cerenkov production depth profiles, the deposited energy in the centre of the water phantom and Cerenkov light were scored within a linear array of 0.1 x 3.5 x 3.5 mm^3 scoring volumes. Cerenkov photons were scored in a particular volume only if they were formed in that volume; photons travelling through a volume were ignored. The chosen scoring volume size was similar to the size of the ionization chamber used experimentally at Clatterbridge to measure the Bragg peak. (Helo et al., 2014a)

2.3.4.1 Cerenkov production in the fast component

The fast component pulse is shown in Figure 2.31(a) for a pristine Bragg beam. The relation between the Bragg peak and the fast component of Cerenkov production for a 60 MeV proton beam was investigated by scoring the deposited energy and the fast component of Cerenkov light which was generated in the same volume (Figure 2.31(b)). (Helo et al., 2014a)

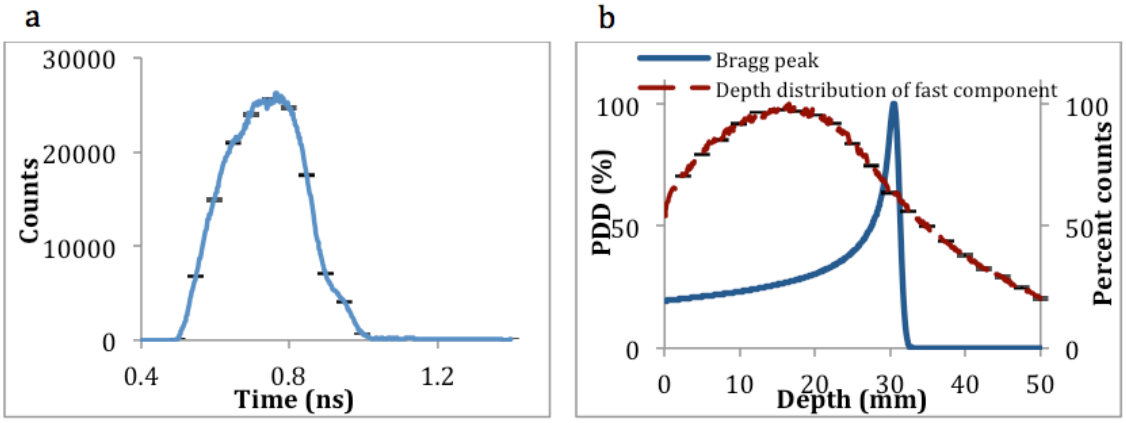

Figure 2.31 (a) Fast component of Cerenkov emission. Simulation used 10^7 proton particles with pulse width equal to zero (all protons were fired at the same time). (b) Comparison between simulated Bragg peak and simulated spatial distribution of fast component in a water phantom for a 60 MeV circular proton beam. The scoring volume is a 3.5 x 3.5 mm^2 square with step equal to 0.1 mm. Error-bars illustrate the statistical standard deviation of the simulation data. (Helo et al., 2014a)

On average, we found that 0.37 optical photons are produced per proton in the fast component. And the contribution of gamma ray photons (Figure 2.27) to the fast component of Cerenkov emission is 99.13%, while neutron (Figure 2.28) contribution make up 0.87% of the fast component.

The production of the fast component of Cerenkov emissions occurs in less than 1 ns, which is similar to the time scale of prompt gamma emissions (Paganetti, 2011). As the fast component depends on gamma rays, which may interact far from their point of origin, no spatial information could be retrieved from the fast component as seen from Figure 2.31(b). (Helo et al., 2014a)

2.3.4.2 Cerenkov production in the slow component

The first 240 s of the simulated slow component is presented in Figure 2.32. The relation between the Bragg peak and the Cerenkov production profile for a 60 MeV proton beam was investigated by scoring the deposited energy and the slow component of Cerenkov light which was generated in the same volume (Figure 2.33). The depth distribution of induced ^{15}O and ^{11}C nuclides are shown in the same figure where the ^{11}C curve is normalized to the ^{15}O curve. (Helo et al., 2014a)

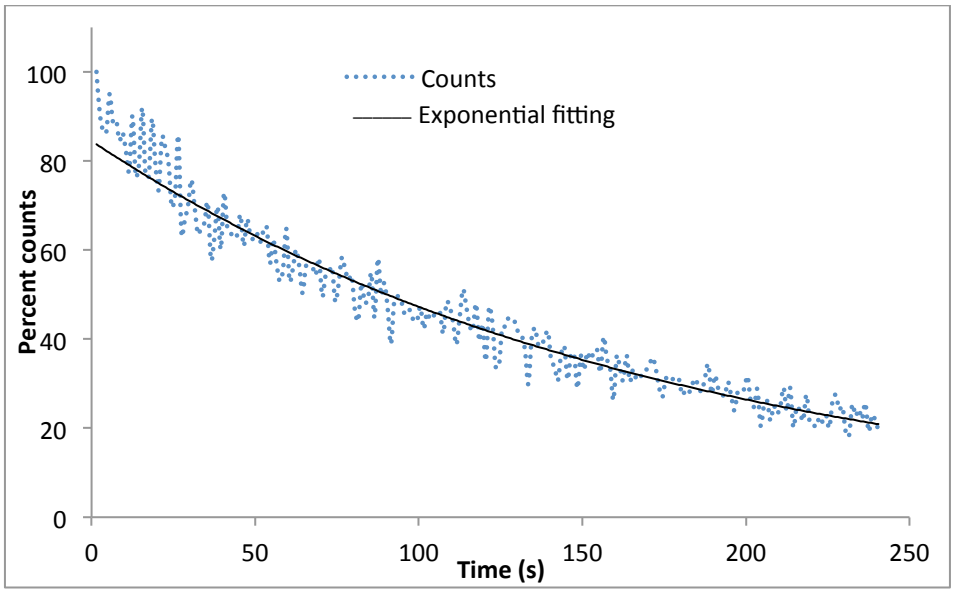

Figure 2.32 The simulated time scale of the slow component of Cerenkov emission. The simulation used 10^7 protons.

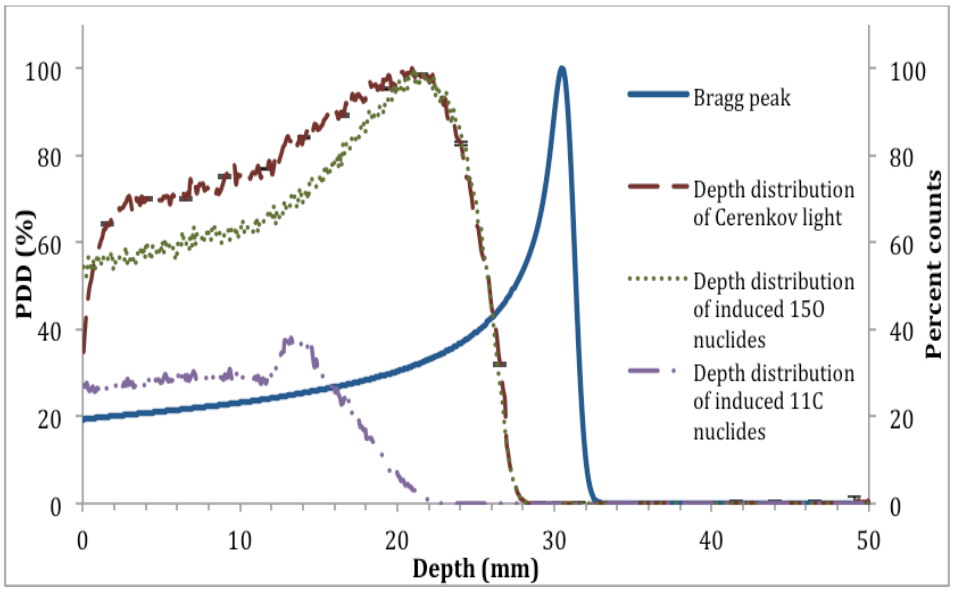

Figure 2.33 Comparison between simulated Bragg peak and simulated Cerenkov production profiles of the slow component in a water phantom for a 60 MeV circular proton beam. The scoring volume is a 3.5 x 3.5 mm^2 square with step equal to 0.1 mm. Error-bars illustrate the statistical standard deviation of the simulation data for Cerenkov production profile. (Helo et al., 2014a)

On average, we found that 0.29 optical photons are produced per proton in the slow component. The calculated half-life of Figure 2.32 was 114 s with a goodness of fit (R^2) of 0.9519. This result demonstrates that the contribution of oxygen-15 dominates over that of other radionuclides (as the half-life of O^{15} is 122.2 s (Table 2.1)). (Helo et al., 2014a)

The contribution of ^{15}O to the slow component of Cerenkov production is more dominant than that of ^{11}C largely because the number of ^{15}O nuclides produced is 3.5 times greater than the number of ^{11}C nuclides (Table 2.1). In addition, the energy spectrum of ^{15}O decay extends to 1.72 MeV, while the spectrum of ^{11}C does not exceed 0.96 MeV, suggesting that positrons emitted by ^{15}O will travel faster and deeper in the medium and therefore produce more Cerenkov emission. By simulating the decay of oxygen-15 and carbon-11 (as described in 2.3.1.4), we found that the average number of Cerenkov photons produced by ^{15}O is 32.78, while for ^{11}C it is 6.86. As the slow component depends on radioactive nuclei decay, we found strong relation between the spatial distribution of slow component and the irradiation field. (Helo et al., 2014a)

2.3.5 *Linearity between Cerenkov emissions and dose or dose rate*

The fast and the slow component linearity with dose were simulated by considering the integration time of the photon collection for all measurements is 1 second and for different irradiation times identical to the delivery times used in the experiment (as will be described in section 3.3.3.2).

2.3.5.1 Fast component

The linearity of the fast component to dose was modelled by delivering different doses to the water phantom and measuring the emitted Cerenkov light. As the measurements would take place during the irradiation time, the measured signal is a combination of the fast component and the slow component (described in section 2.3.4). Figure 2.34 shows the dose linearity of the fast and the slow component of Cerenkov emission during the irradiation time, using a 60 MeV proton beam. (Helo et al., 2014a)

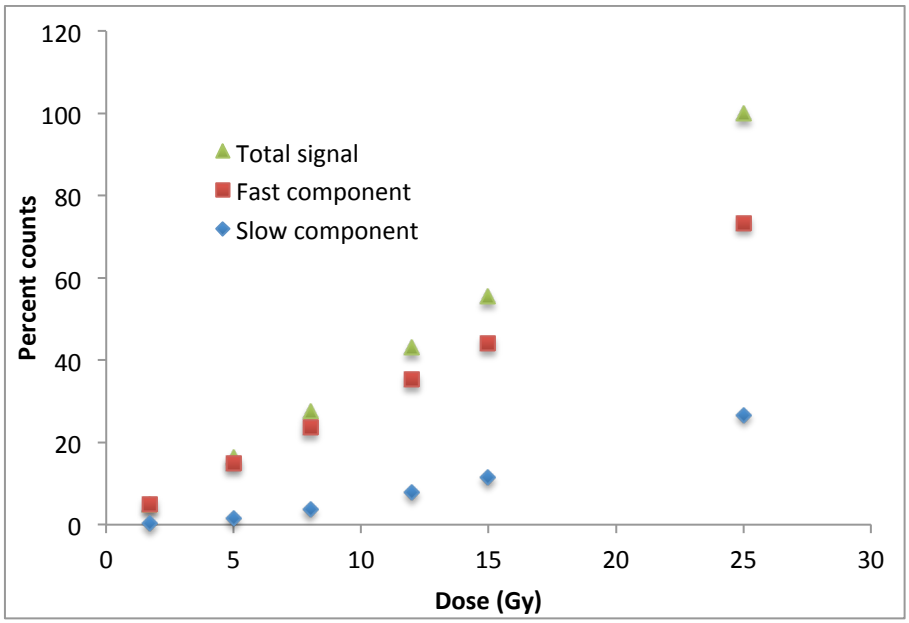

Figure 2.34 Demonstration of dose linearity from 1.7 to 25 Gy with a 60 MeV beam by simulating the Cerenkov emission during irradiation time. All measurements were normalized to 25 Gy. (Helo et al., 2014a)

Simulation showed that the fast component of Cerenkov emission is linear with dose. However, the contribution of the slow component in the detected signal varies between 0.17% and 26.63%

depending on the extended time required to deliver a given dose (which varied between 17 s and 258 s), which introduces non-linearity to the measured signal. (Helo et al., 2014a)

2.3.5.2 Slow component

The linearity of the slow component was modelled by delivering different doses to the water phantom and measuring the emitted Cerenkov light after the beam was off and for 20 s. Figure 2.35 shows the linearity of the slow component of Cerenkov measurements with dose, using a 60 MeV proton beam. (Helo et al., 2014a)

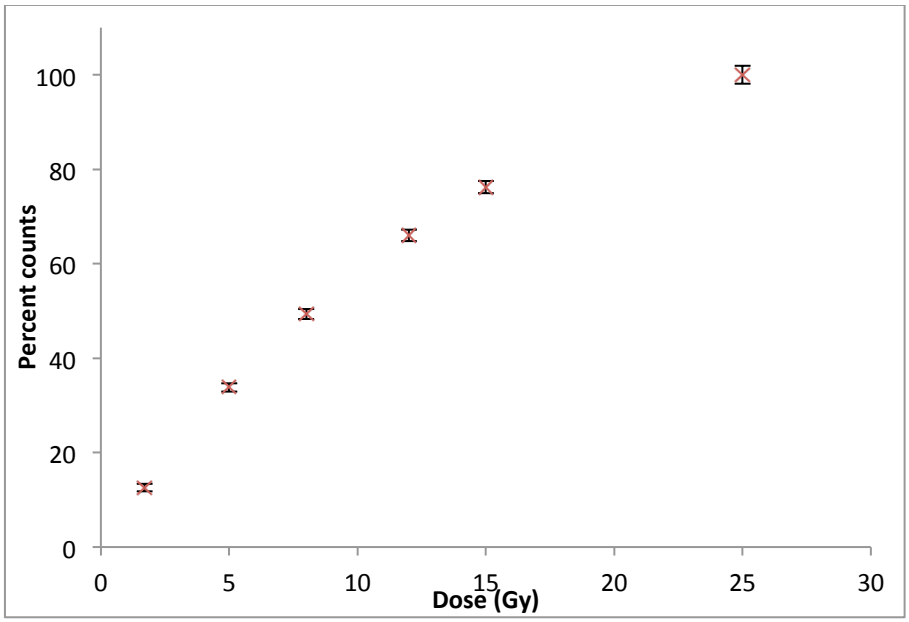

Figure 2.35 Demonstration of dose linearity from 1.7 to 25 Gy with a 60 MeV beam by simulating (a) the fast component of Cerenkov production. (b) The slow component of Cerenkov production. All measurements were normalized to the 25 Gy. Error-bars show the standard deviation of the simulation data. (Helo et al., 2014a)

Simulation showed that the slow component of Cerenkov emission is non-linear with dose. This is due to the extended time required to deliver a given dose, meaning that any radionuclides which are generated during beam delivery will have begun to decay by the end of the irradiation time, reducing the measured count rate from higher doses (and therefore longer delivery times). (Helo et al., 2014a)

2.3.6 *Eyeball and retina simulation*

The number of Cerenkov photons which hit the human retina when it is irradiated by a circular proton beam with diameter of 1 cm and energy of 60 MeV was simulated by approximating the eyeball to a sphere with 2.5 cm diameter (Kolb et al., 1995) made of water (the refractive index of water is 1.333, while the refractive index of vitreous humour is 1.336). The retina was simulated as a sphere covering 65% of the inside of the eyeball with thickness 0.1 mm (Kolb et al., 1995)(the retina contains rods which detect the light without colour sensitivity). The fovea was a sphere with 1.8 mm diameter, positioned 2.5 mm away from the eye horizontal axis (Kolb et al., 1995) (the fovea contains the cones which detect the light colour). The geometry of the eyeball simulation is shown in Figure 2.36(a); and the light distribution in the retina is shown in Figure 2.36(b). (Helo et al., 2014a)

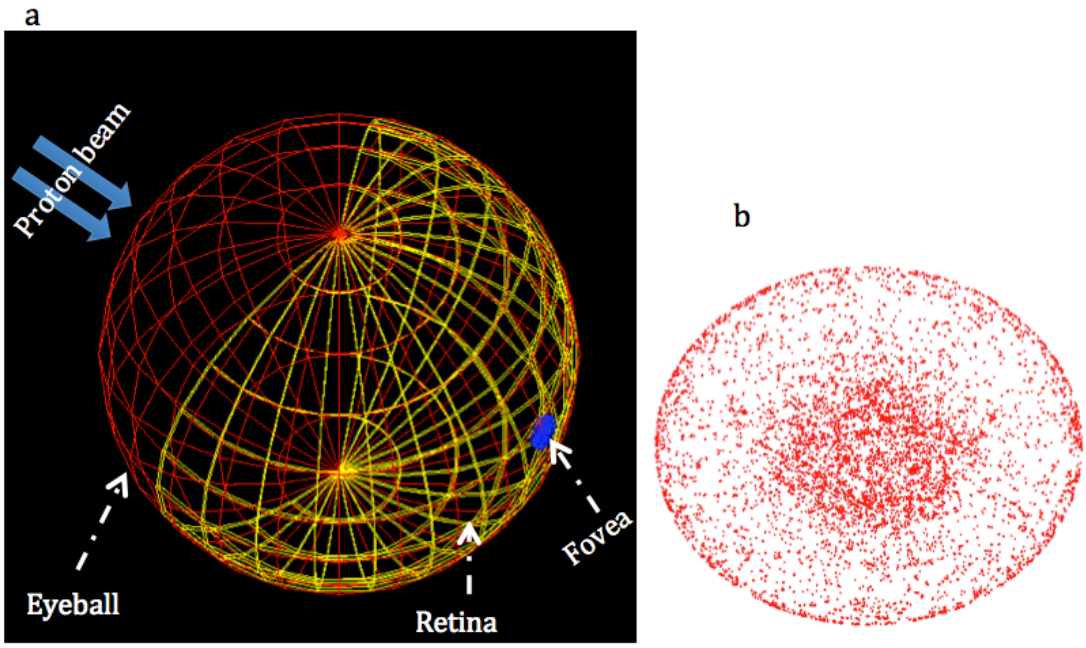

Figure 2.36 (a) Geometry of eyeball simulation. (b) Light distribution in the retina from 10^7 protons. (Helo et al., 2014a)

2.3.6.1 The total number of photons generated in the human eye by the fast and slow components of Cerenkov production

On average it was found that 6.9 x 10^{-4} photons hit the retina per proton of 60 MeV in the fast component and 5.7 x 10^{-4} photons in the slow component. While 6 x 10^{-6} photons are incident on the fovea per proton in the fast component, 2 x 10^{-5} photons are incident in the slow component. (Helo et al., 2014a)

Patients with eye cancer (uveal melanomas as an example) are given 53.1 Gy in 4 fractions, with each fraction being delivered in approximately 30 s (Kacperek, 2009). The total number of protons per second per fraction is therefore approximately 3.5 x 10^{8} assuming the mass of the eyeball is 7.5 g (Suri et al., 2008). The total number of photons, which hit the retina, is approximately 2.4 x 10^{5} photons per second by the fast component, which suggests that, considering the mean absorbance spectrum of the rods reported in Bowmaker and Dartnall (1980), 10^{5} photons per second are detected by the rods. The slow component, on the other hand, will increase from 1.8 x 10^{3} to 6.9 x 10^{4} photons per second during the irradiation time as more isotopes are generated; these emissions will decrease with time as the isotopes decay. (Helo et al., 2014a)

The human eye is capable of seeing 10-100 photons arriving within less than 100 ms when under otherwise dark conditions (Hecht et al., 1942; Schnapf and Baylor, 1987). In the treatment room, lights are usually dimmed to reduce patient distraction. In addition, many patients have their eyes partially closed during the treatments or their tumours may obscure the retina. Despite this, patients report seeing a light glow when the radiation is on even when their eyes are closed, indicating that Cerenkov emissions can be seen in the presence of room lights. Thus, we believe that Cerenkov emission liberated inside the eye during proton therapy is sufficiently bright that it should be visible to the patient. (Helo et al., 2014a)

Chapter 3

EXPERIMENTAL RESULTS AND DISCUSSION

3.1 Imaging Cerenkov emission as a quality assurance tool in electron radiotherapy

3.1.1 Objectives

The potential of using a standard commercial camera to image Cerenkov light generated from electrons in water for fast QA measurement of a clinical electron beam was explored and compared to ionization chamber measurements.

In this chapter, the delivered doses and dose rates were correlated to the measured image intensities in photographs of Cerenkov light. Comparisons are made between the percentage depth dose (PDD) of different electron beam energies with profiles measured from Cerenkov emissions in order to explore whether the latter can be used to check the stability of electron ranges in water. Comparisons are also made between the beam profile of 6 x 6 cm^2 electron beam at d_{max} with the Cerenkov beam profile at the same depth, to explore whether the latter can be used as a field size verification tool.

3.1.2 Materials and methods

All tests were carried out using a Varian linear accelerator (TrueBeam™, Varian Medical Systems, Palo Alto, CA), using electron energies of 6, 9 and 12 MeV with source-to-surface distance (SSD) equal to 100 cm and a 50 x 50 x 50 cm water phantom made from 5 mm thick walls of transparent Perspex (RFA 300, IBA, Belgium). The Cerenkov light was imaged using a CCD camera (Nikon D70, Nikon, Tokyo, Japan) equipped with a standard 50 mm f/1.8 Macro HSM lens (Sigma Corporation, Kawasaki, Japan). The integration time for all images was 30 seconds, the aperture was f/1.8 and the CCD gain was ISO800 (ISO controls how sensitive the image sensor is to light and its value usually varies between 100 and 2000). The raw images had a size of 3039 x 2014 pixels, and were processed by subtracting a background image that was obtained in the same lighting conditions but with the beam turned off. All images were converted from NEF format which is the raw format of the Nikon camera to Tiff format which retains all the information in the image and can be read into

Matlab. All images were tested for saturation and corrected for vignetting. Vignetting is the reduction of an image's brightness at the margin compared to the image centre, which is caused by optical effects in a multi-lens system (Ray, 2002). A vignetting correction factor for each pixel was determined experimentally by imaging a uniformly illuminated field produced by two 50 Hz tube white light sources positioned at 45 degrees projected onto a diffuser sheet. Vignetting correction images were smoothed in Matlab by an averaging filter of 15 pixels diameter to remove the effects of sensor noise. To reduce radiation noise in the images, which predominantly comes from stray X-rays depositing energy in the CCD, and appears as white spots, a 3 x 3 pixel median filter was applied (Smith, 2003), before applying the smoothing filter. (Helo et al., 2014d)

The camera was remotely controlled from outside the Linac room by a PC and a 25 m USB cable. The camera setup is shown in Figure 3.1. All light sources in the room were either turned off or blocked by a black sheet during the experiments. The reproducibility was tested by recording 4 consecutive images for each measurement and then calculating the standard deviation of each test. The camera was placed at 90° with respect to the incident electron beam. Distance calibration was performed for each experiment by imaging a metric ruler in the light room conditions placed in the centre of the beam as shown in Figure 3.1. (Helo et al., 2014d)

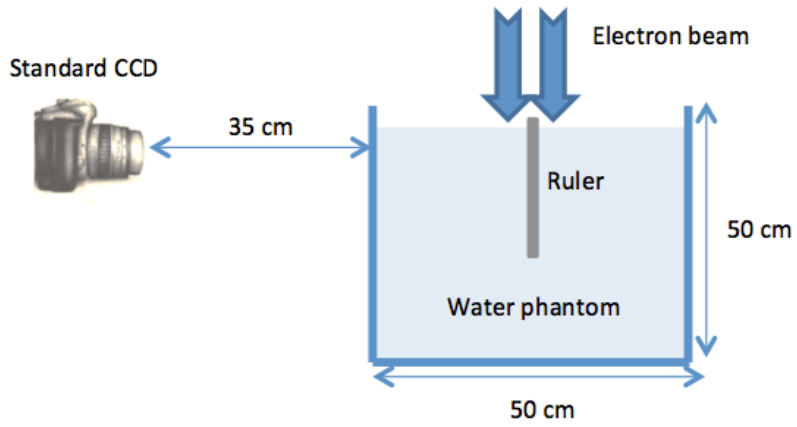

Figure 3.1 Schematic of the experiment setup. (Helo et al., 2014a)

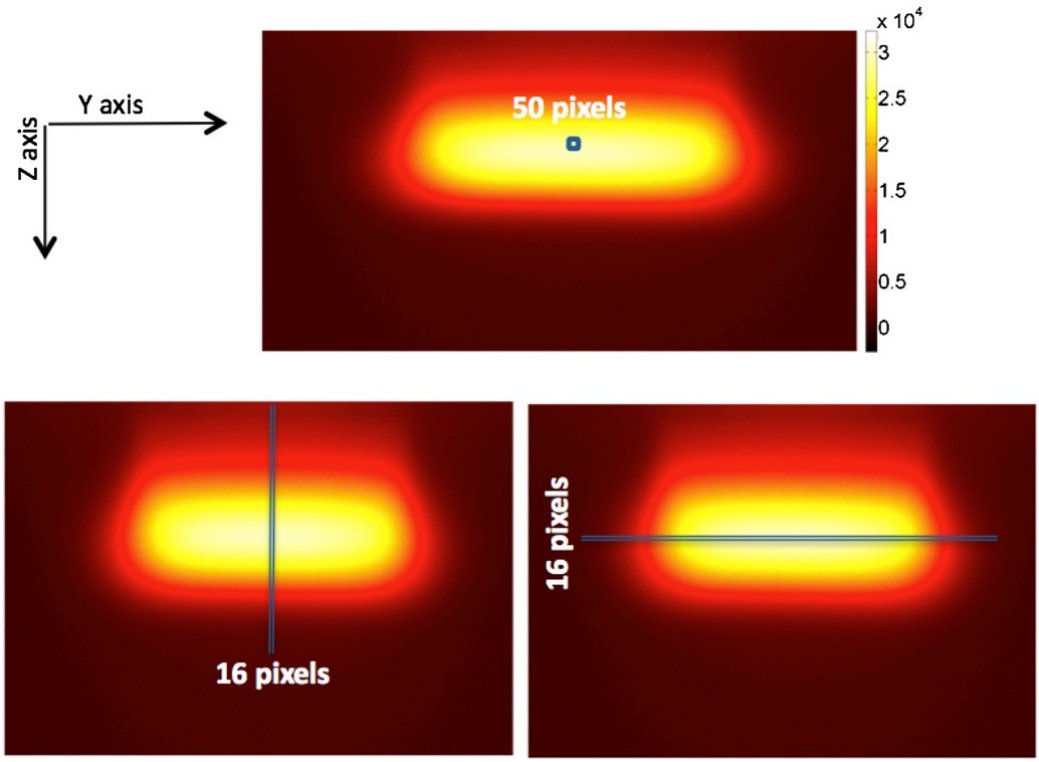

Figure 3.2 Digital images of Cerenkov light from 12 MeV electron beam showing various regions of integration. (a) The region of interest for linearity test and dose- rate dependence. (b) The beam-direction profile plane. (c) The transverse profile plane at depth of dose maximum. (Helo et al., 2014a)

3.1.2.1 Dose linearity

Images were taken with a 10 x 10 cm^2 applicator, at a dose rate of 600 Monitor Units (MU) per minute and 12 MeV electron beam. The dose linearity between 5 and 200 MU was checked by summing the value of a 50 pixel x 50 pixels area as illustrated in Figure 3.2(a). Typical treatment fields deliver dose of about 2 Gy per fraction, corresponding to 200 to 300 MU, depending on energy and field size. Ideally, a dosimeter used in radiotherapy should be linearly proportional to the dose, and any non-linearity behaviour should be corrected for over a wide range.

3.1.2.2 Dose rate dependence

Measurements were made with 10 x 10 cm^2 applicator delivering 100 MU with a 12 MeV electron beam. The dose rate dependence from 300-900 MU/min was evaluated by summing the value of 50 pixels x 50 pixels area as illustrated in Figure 3.2(a). The dose rate of a typical treatment is 600 MU/min. Ideally; a dosimeter response should be independent of the dose rate.

3.1.2.3 Beam-direction profiles and electron range measurements

Images were taken with a 10 x 10 cm^2 applicator, 100 MU dose and 600 MU/min dose rate. The beam-direction profile relates the change in the intensity values of the image with depth [the z-axis in Figure 3.2(b)], averaged over a width of 16 pixels. The practical range of electron beam was evaluated by plotting the beam-direction profiles for 6, 9, and 12 MeV electron beam images. The practical electron range is defined as the depth where the tangent to the inflection point of the decreasing portion of the depth-dose curve meets the extrapolated Bremsstrahlung (X-ray) background (as described in 1.3.1.1) (Cleland et al., 2004). In Cerenkov measurements, the range was defined as the point where the tangent to the inflection point of the decreasing portion of the extrapolated beam-direction profile curve meets the x-axis. In practice, the tangent to the curve was fitted algebraically as a straight-line passing through D_{70} and D_{30} (depth of 70% and depth of 30% of the maximum) as shown in Figure 3.3.

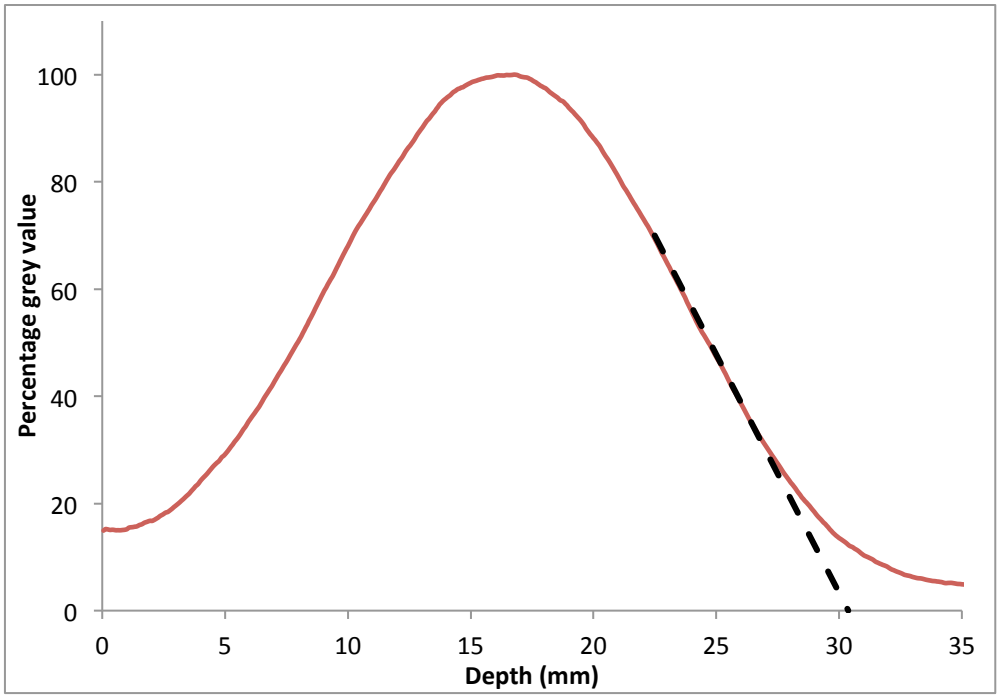

Figure 3.3 Beam-direction profile of Cerenkov emission for 6 MeV electron beam shows the tangent to the inflection point of the decreasing portion of the extrapolated beam-direction profile.

3.1.2.4 Field size

Images were taken at 100 MU, 600 MU/min dose rate and 12 MeV electron beam for applicator size equal to 6 x 6 cm^2. The transverse profile relates the change in the grey values of the image at a

certain depth, orthogonal to the z-axis (as described in 1.3.1.2). The transverse profiles at the depth of maximum dose d_{max} (2.7 cm) were evaluated by plotting the transverse profile of the field size images as shown in Figure 3.2(c), averaged over a width of 16 pixels. (Helo et al., 2014d)

3.1.2.5 Field size dependence

Measurements were made at 100 MU, 600 MU/min dose rate and 12 MeV electron beam for three different applicator sizes 6 x 6 cm^2, 10 x 10 cm^2 and 15 x 15 cm^2. The field size dependence was evaluated by plotting the beam-direction profiles as described in section 3.1.2.3 for the different field sizes. (Helo et al., 2014d)

3.1.2.6 Field depth and vignetting problem

The effects of the depth of the field on the spatial resolution and the vignetting problem were also investigated. It was found experimentally that the depth of field associated with our experiment setup reduced the spatial resolution to less than 1 mm for 10 x 10 cm^2 field size. The vignetting correction factor for each pixel was found experimentally as described in section 3.1.2. The vignetting correction factor is presented in Figure 3.4. All lenses produce geometrical distortion in the image and for best results these distortions should be corrected. Ideally this should be done by photogrammetry (not tomography) to characterize the mapping function of the real world onto the image plane with a small number (typically seven to nine) parameters (Shortis et al., 1998). The vignetting correction factor was applied to all measured images. (Helo et al., 2014d)

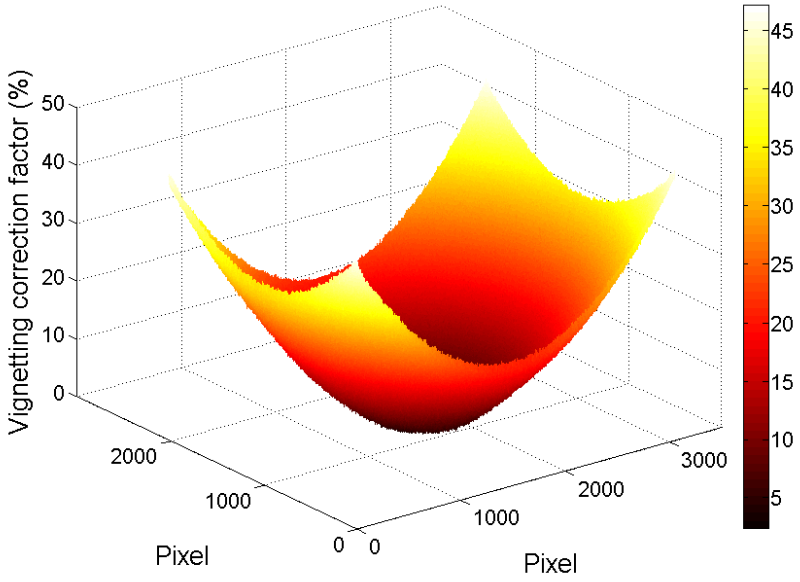

Figure 3.4 Vignetting correction factor of the used lens as described in 3.1.2. (Helo et al., 2014d)

3.1.3 Results and discussion

3.1.3.1 Linearity between Cerenkov measurements and dose

The relationship of camera response to dose was examined by delivering different doses to the water phantom and imaging the emitted Cerenkov light. Figure 3.5 shows the dose linearity of Cerenkov images using a 12 MeV electron beam. All measurements are normalised to the 200 MU measurement. (Helo et al., 2014d)

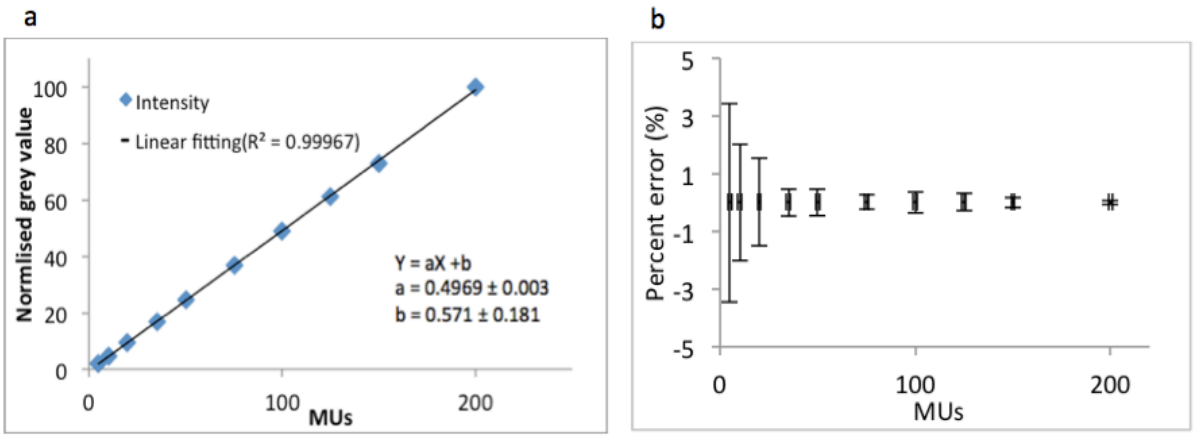

Figure 3.5 (a) Demonstration of dose linearity from 5 to 200 MU with a 12 MeV beam. All measurements were normalised to the 200 MU measurement. (b) The percentage error of the measured data as a function of MUs. The error bars represent the standard deviation of 4 repeated readings. (Helo et al., 2014d)

It was found that the commercial digital camera was sensitive enough to detect the smallest dose delivered by our Linac (5 MU) within 3% uncertainty. A region of interest in the Cerenkov images equal to a square of 3 x 3 mm^2, which is the same size as a typical scanning ionization chamber, was chosen to check the dose linearity. The goodness of the fitting to data (R^2 value) is better than 0.9997. The percentage standard deviation in the worst case was ±3.4% for the smallest MU delivered. (Helo et al., 2014d)

3.1.3.2 Dependence of Cerenkov measurements on dose rate

The linearity of Cerenkov emission detection with dose rate was measured by delivering different dose rates and imaging the emitted Cerenkov light. Figure 3.6 shows the dose rate dependence in the Cerenkov images averaged over 3 x 3 mm^2 squares, using a 12 MeV electron beam. The variation of the dose rate was found to be less than 0.65%, compared to 0.6% with an ionization chamber due to the variation in accelerator output found by (Li et al., 2013). All measurements were normalised to the 900 MU/min measurement. (Helo et al., 2014d)

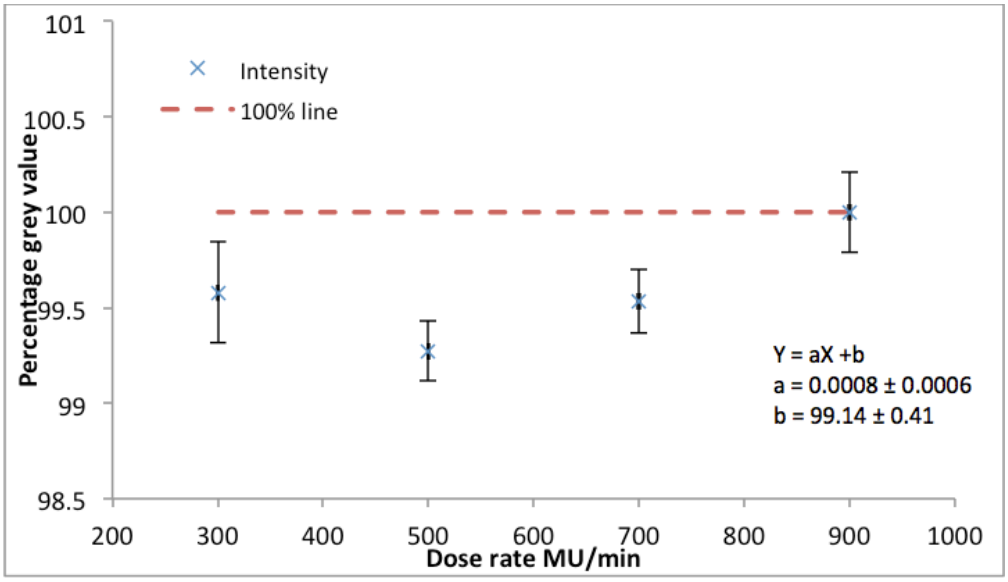

Figure 3.6 Dose rate measurements using Cerenkov-electron method for 12 MeV electron beam. The variation is less than 0.65%. All measurements normalised to the 900 MU/min measurement. Error-bars shown are the standard deviation of 4 repeated readings. (Helo et al., 2014d)

3.1.3.3 Range measurements

To measure the practical range of the electron beams in water, the measured beam-direction profiles for different electron energies were compared to depth dose profiles measured using the ionization chamber. Because the depths of dose maximum and of Cerenkov light maximum do not coincide, all data were normalised to match at the depth of 50% of dose maximum, as shown in Figure 3.7. The practical electron ranges measured in the Cerenkov images and by the ionization chamber were calculated and compared as explained in section 3.1.2.3. (Helo et al., 2014d)

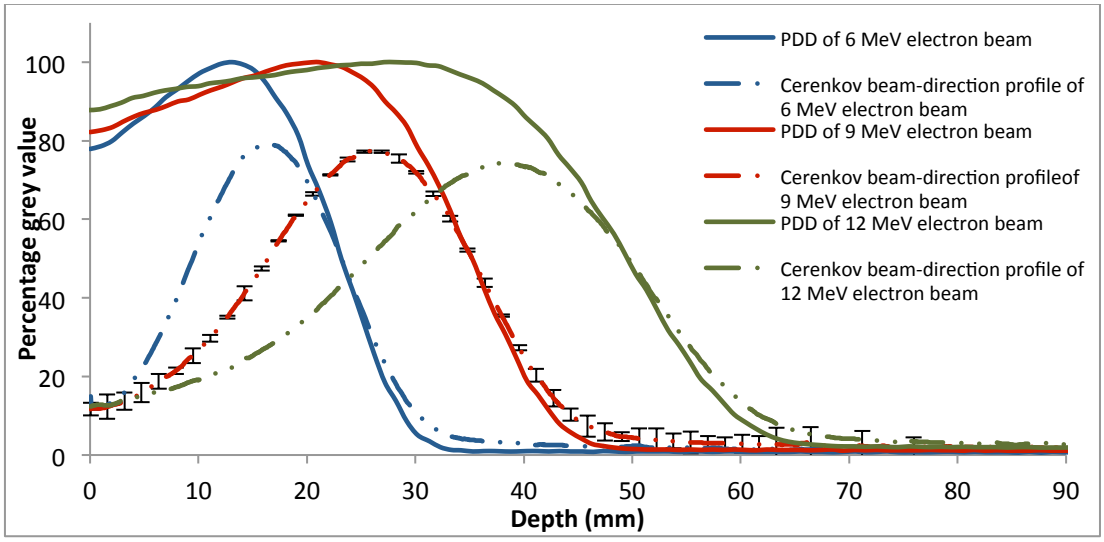

Figure 3.7 Beam-direction profiles for different electron energies compared with electron depth doses measured by ionization chamber. Error-bars shown are the standard deviation of 4 repeated readings of 12 MeV measurements. (Helo et al., 2014d)

For range measurements, an average was taken over steps of 1 mm to satisfy the clinical requirement of ≤ 2 mm. It can be seen from Figure 3.7 that the slope of the descending portion of the Cerenkov beam-direction profile is gentler than that for the depth doses. This is due to the magnification effect (as explained in section 2.2.6.1), and it results in an overestimation of the practical range derived from the Cerenkov images. The ranges were 29.5 mm and 30.5 ± 1 mm for the PDD and Cerenkov measurements for the 6MeV beam, 43.5 mm and 45.0 ± 1 mm for the 9 MeV beam and 60.0 and 63.0 ± 1 mm for the 12 MeV beam. The differences in depth between PDDs and the corresponding Cerenkov profiles increase with beam energies. This is due to magnification effects as described in section 2.2.6.1. (Helo et al., 2014d)

Note that Cerenkov beam-direction images are very different from the depth doses, especially in the build-up region, due to: (i) the scattering pattern of electrons inside the water which is energy dependent; (ii) the angular dependency of Cerenkov production, which is also energy dependent; (ii) the refraction of the light when it travels from water to transparent phantom walls then to air. (Helo et al., 2014d)

3.1.3.4 Field size

To estimate the width of the beam profile at d_{max}, the transverse profiles measured in the Cerenkov images were compared to the ionization chamber measurements at d_{max} for 12 MeV electron beam and 6 x 6 cm^2 field size as shown in Figure 3.8. All data were normalised to their maximum value.

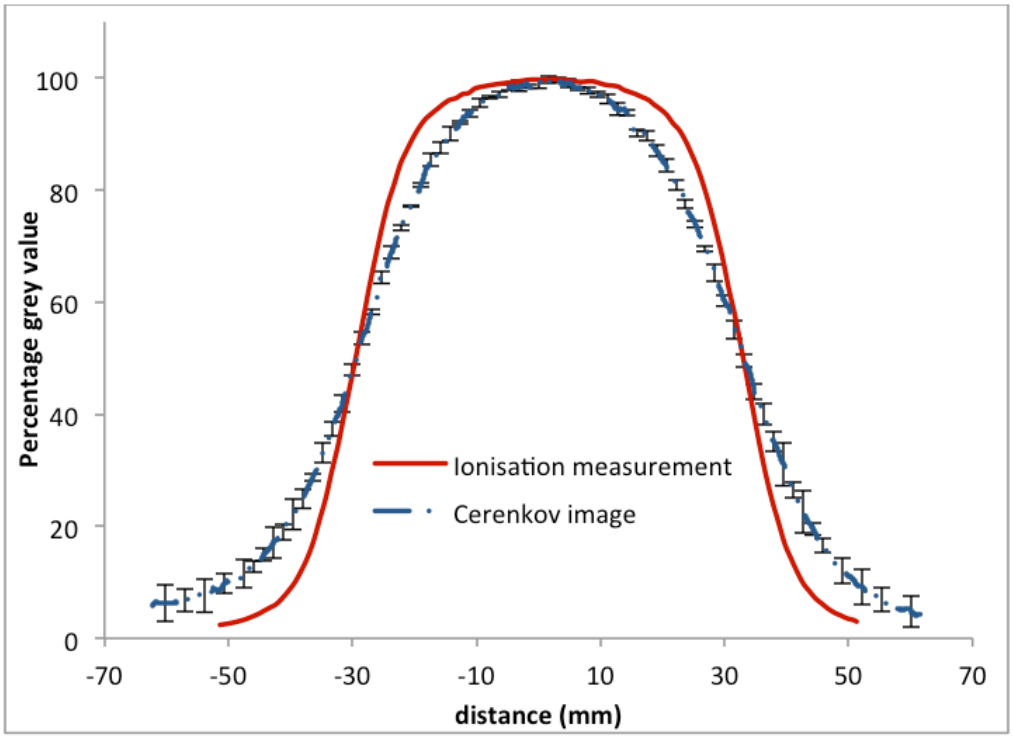

Figure 3.8 Transverse profiles at d_{max} for 6 x 6 cm^2 beam field measured by ionization chamber and Cerenkov images, The Cerenkov measurements were corrected for vignetting. Error-bars shown are the standard deviation of 4 repeated readings. (Helo et al., 2014d)

For field size measurement, again an average was taken over a 1 mm step in the z-axis to satisfy the clinical requirement of ≤ 2 mm. The penumbra of the transverse profile measurements appears much wider than for the ionization chamber measurements. This is partly due to the magnification effect, as explained in section 2.2.6.1. This leads to the blurring effect, which is apparent in Figure 3.8. This could be solved by tomography from multiple camera images. However, noting that the blurring effect is symmetrical about the primary beam axis, the Cerenkov profile will provide an accurate measure of the beam width measured at 50% of the maximum dose. For example, in Figure 3.8, the beam profile at 50% of the maximum measured by the ionization chamber is 6.2 cm whereas measured by Cerenkov emissions it is 6.2 ± 0.1 cm. (Helo et al., 2014d)

3.1.3.5 Field dependence

The dependence of the beam-direction profiles in Cerenkov images on the field sizes was explored. The measured beam-direction profiles for applicator sizes of 6 x 6 cm^2, 10 x 10 cm^2 and 15 x 15 cm^2 were compared for a 12 MeV electron beam as shown in Figure 3.9. All data were normalised to their maximum values. The beam-direction profile measurements generally matched to within 2% apart from the distal tail where the intensity was very low. Since depth dose profiles of electron beams are constant for large enough field sizes, the similarity of the Cerenkov beam-direction profiles shows that there is only a small influence from field size due to the magnification effect on the beam-direction profiles, as discussed in section 2.2.6.1. Therefore, this method can be used to check the constancy of electron range independently from the field size used. (Helo et al., 2014d)

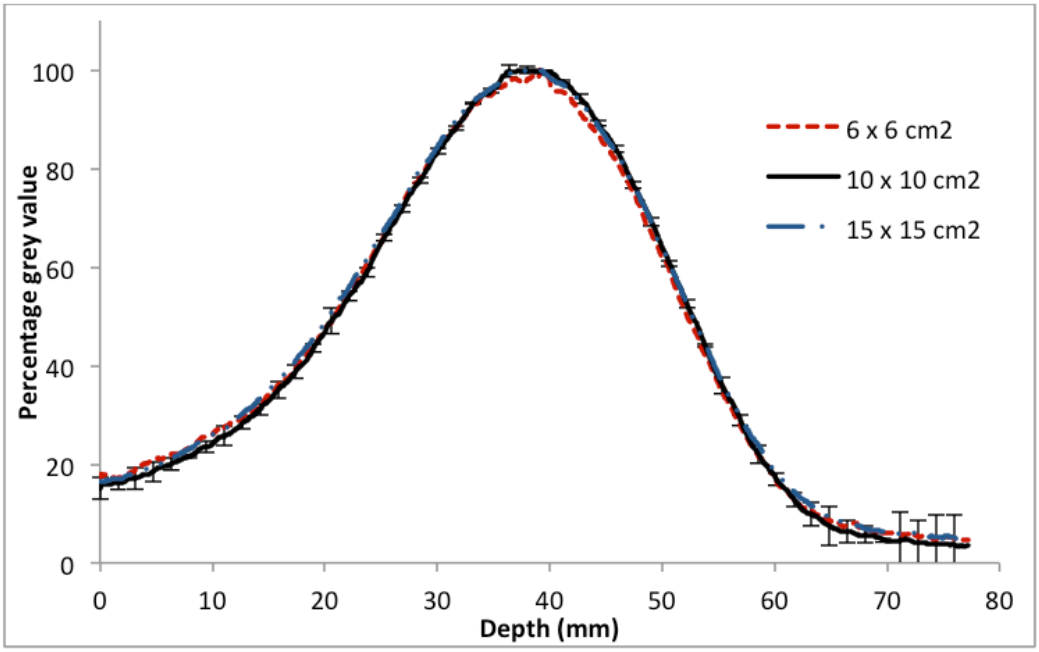

Figure 3.9 Beam-direction profiles for different collimator sizes, normalised to their respective maximum. Error-bars shown are the standard deviation of 4 repeated readings of 10 x 10 cm^2 measurements. (Helo et al., 2014d)

3.2 Imaging Cerenkov emission in a conical phantom with tissue-equivalent optical properties

3.2.1 Objective

The potential of using a standard commercial camera, which has the infrared filter removed, to image Cerenkov emission generated from electrons in conical phantom with tissue-equivalent optical properties for QA during breast treatment was explored. All commercial cameras are equipped with infrared filters to stop the infrared radiation and reduce the noise in the image. By removing the infrared filter, the camera becomes sensitive to the infrared and visible radiation. As Cerenkov emission spectrum extends to the infrared region (section 1.2) and the infrared radiation penetrates the tissue further than visible light, most of the Cerenkov emission emitted from the phantom is near infrared and infrared.

The delivered doses and dose rates are correlated to the measured image intensities in photographs of Cerenkov light. The beam-direction profiles of Cerenkov emissions were used to check the electron ranges in phantom. The maximum in the light output with the incident electron angles was examined. The potential of using Cerenkov image for detecting and identifying differences between normal and diseased tissues was investigated.

3.2.2 Material and methods

All tests were carried out using a Varian linear accelerator (TrueBeam™, Varian Medical Systems, Palo Alto, CA), using electron energies of 6, 9, 12, 16 and 20 MeV with source-to-surface distance (SSD) equal to 100 cm and a breast like optical phantom made of a mixture of titanium dioxide particles and NIR absorbing dye in epoxy resin (Firbank et al., 1995). The optical properties of the phantom at a wavelength of 800 nm are: transport scatter coefficient $\mu_s^{`} = 0.8 \pm 0.1$ mm^{-1}, absorption coefficient $\mu_a = 0.007 \pm 0.001$ mm^{-1} and a refractive index of 1.56 (Hebden et al., 2001). The Cerenkov light was imaged using a CCD camera with infrared filter removed. The integration time for all images was 30 seconds, the aperture was f/1.8 and the CCD gain was ISO800. The raw images had a size of 3039 x 2014 pixels, and were processed by subtracting a background image that was obtained in the same lighting conditions but with the beam turned off. All images were converted from NEF format which is the raw format of the Nikon camera to Tiff format which retains all the information in the image and can be read into Matlab. All images were tested for saturation and corrected for vignetting as described in 3.1.2.6. To reduce radiation noise in the images, which predominantly comes from stray X-rays depositing energy on the CCD, and appears as white spots, a 3 x 3 pixel median filter was applied.

The camera was remotely controlled from outside the Linac room by a PC and a 25 m USB cable. The camera setup is shown in Figure 3.10. All light sources in the room were either turned off or blocked by a black sheet during the experiments. The reproducibility was tested by recording 2 consecutive images for each measurement and then calculating the standard deviation of each test. The camera was placed at 90° with respect to the incident electron beam unless stated otherwise.

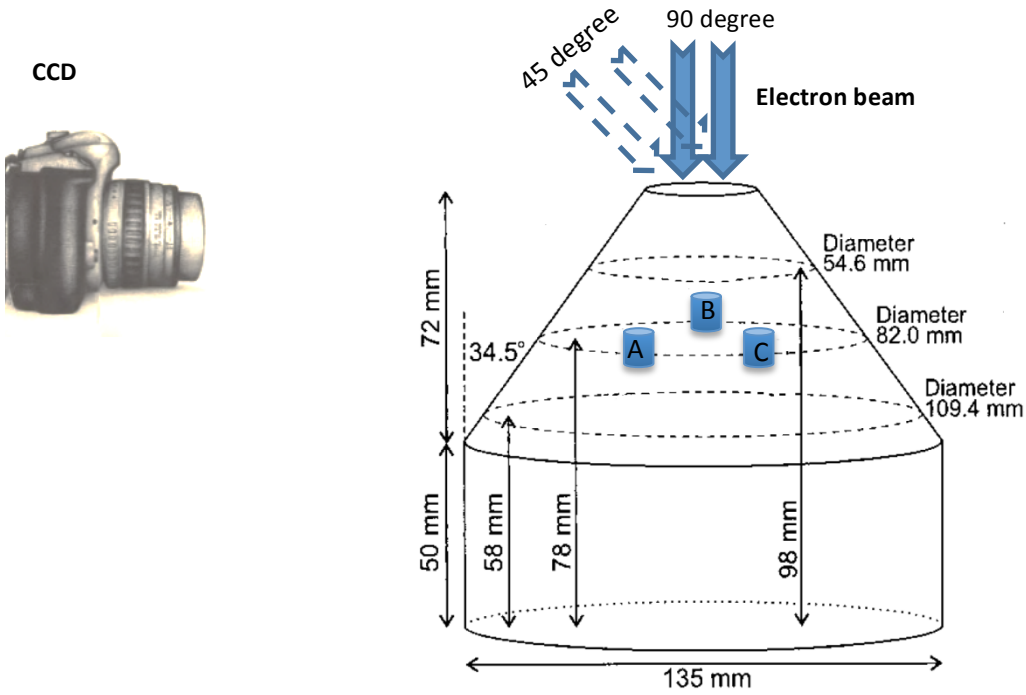

Figure 3.10 A description of the experiment setup and phantom anatomy. A, B and C are 3 cylinders with 1 cm diameter and height, made with different optical properties, A ($2\mu_s^{`}$ and $\mu_a$), B ($\mu_s^{`}$ and $2\mu_a$) and C ($2\mu_s^{`}$ and $2\mu_a$) (Hebden et al., 2001).

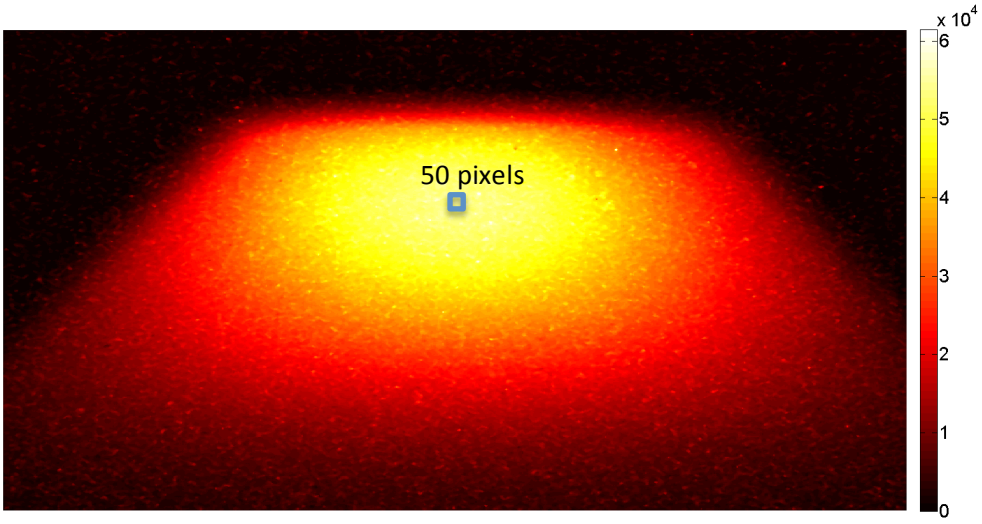

Figure 3.11 Digital image of Cerenkov light from 12 MeV electron beam showing the region of integration for linearity test and dose- rate dependence.

3.2.2.1 Dose linearity

Images were taken with a circular collimator with diameter equal to 2.5 cm, at a dose rate of 600 MU/minute and 12 MeV electron beam. The dose linearity between 5 and 150 MU was checked by summing the value of a 50 pixel x 50 pixels area as illustrated in Figure 3.11.

3.2.2.2 Dose rate dependence

Measurements were made with circular collimator with diameter equal to 2.5 cm delivering 100 MU with a 12 MeV electron beam. The dose rate dependence from 400-1000 MU/min was evaluated by summing the value of 50 pixels x 50 pixels area as illustrated in Figure 3.11.

3.2.2.3 Beam-direction profiles

Images were taken with circular collimator with diameter equal to 2.5 cm, 100 MU dose and 600 MU/min dose rate. The beam-direction profile relates the change in the intensity values of the image with depth averaged over a width of 16 pixels. The beam-direction profiles for different electron energies were measured.

3.2.2.4 Angular dependence

Images were taken with circular collimator with diameter equal to 2.5 cm, 100 MU dose and 600 MU/min dose rate. The camera was placed at different angles with respect to the incident electron beam. The angular dependence between 90 and 45 degrees (as illustrated in Figure 3.10) was checked by summing the value of a 50 pixel x 50 pixels area as illustrated in Figure 3.11.

3.2.2.5 Imaging phantom with different optical properties

A pair of conical phantoms with uniform optical properties was used (as described in 3.2.2). Inserted in one phantom three cylinders with higher scattering coefficients ($\mu_s`$) and absorption coefficients ($\mu_a$) (representing diseased tissues) as shown in Figure 3.10 (Hebden et al., 2001). Evidence suggests that the ratio between the values of both $\mu_s`$ and μ_a for healthy and cancerous tissues are of the order of a factor of 2 (Hebden et al., 2001; Tromberg et al., 2000). Images were taken with circular collimator with diameter equal to 2.5 cm, 100 MU dose and 600 MU/min dose rate. The camera was placed at different angles with respect to the incident electron beam. The images of the two phantoms were subtracted in aim of recovering the inserts positions inside the phantom by performing simple subtraction.

3.2.3 Results and discussion

3.2.3.1 Linearity between Cerenkov measurements and dose

The relationship of camera response to dose was examined by delivering different doses to the phantom and imaging the emitted Cerenkov light. Figure 3.12 shows the dose linearity of Cerenkov images using a 12 MeV electron beam. All measurements are normalised to the 150 MU measurement.

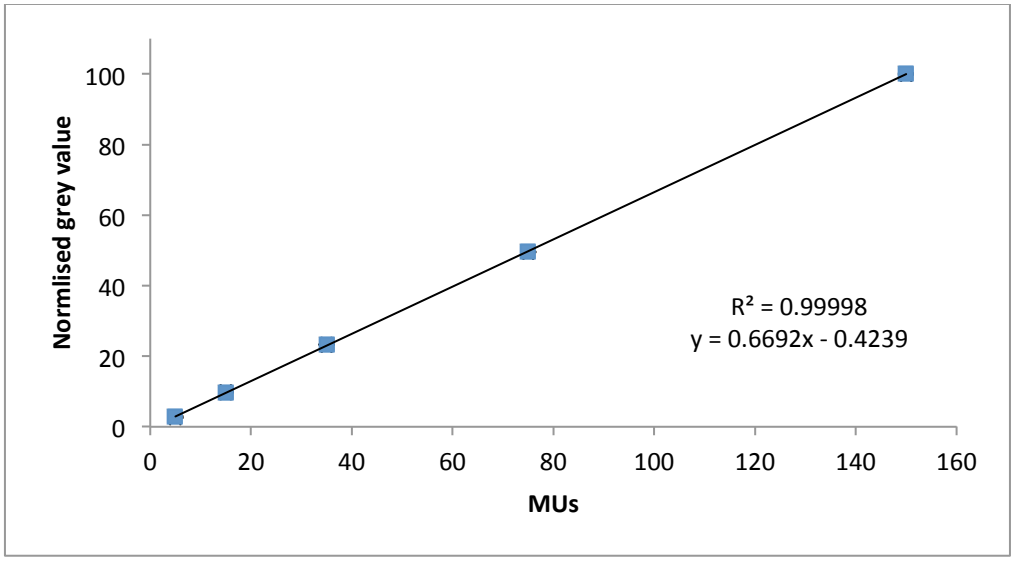

Figure 3.12 Demonstration of dose linearity from 5 to 150 MU with a 12 MeV beam. All measurements were normalised to the 150 MU measurement. The error bars (representing the standard deviation of 2 repeated readings) are smaller than the point size in some points of the curve.

The goodness of the fitting to data (R^2 value) is better than 0.9998. The percentage standard deviation in the worst case was ±8% for the smallest MU delivered.

3.2.3.2 Dependence of Cerenkov measurements on dose rate

The linearity of Cerenkov emission detection with dose rate was measured by delivering different dose rates and imaging the emitted Cerenkov light. Figure 3.13 shows the dose rate dependence in the Cerenkov images averaged over 50 pixels x 50 pixels, using a 12 MeV electron beam. The

variation of the dose rate was found to be less than 1.18%. All measurements were normalised to the 1000 MU/min measurement.

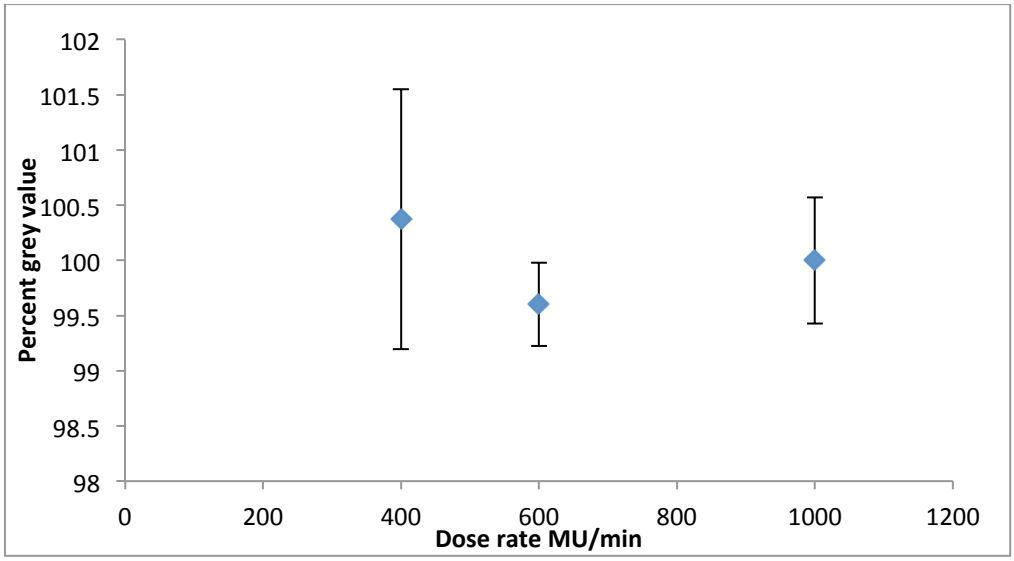

Figure 3.13 Dose rate measurements using Cerenkov-electron method for 12 MeV electron beam. The variation is less than 1.18%. All measurements normalised to the 1000 MU/min measurement. Error-bars shown are the standard deviation of 2 repeated readings.

3.2.3.3 Beam-direction profiles

The measured beam-direction profiles for different electron energies are presented in Figure 3.14. All data were normalised to the maximum value.

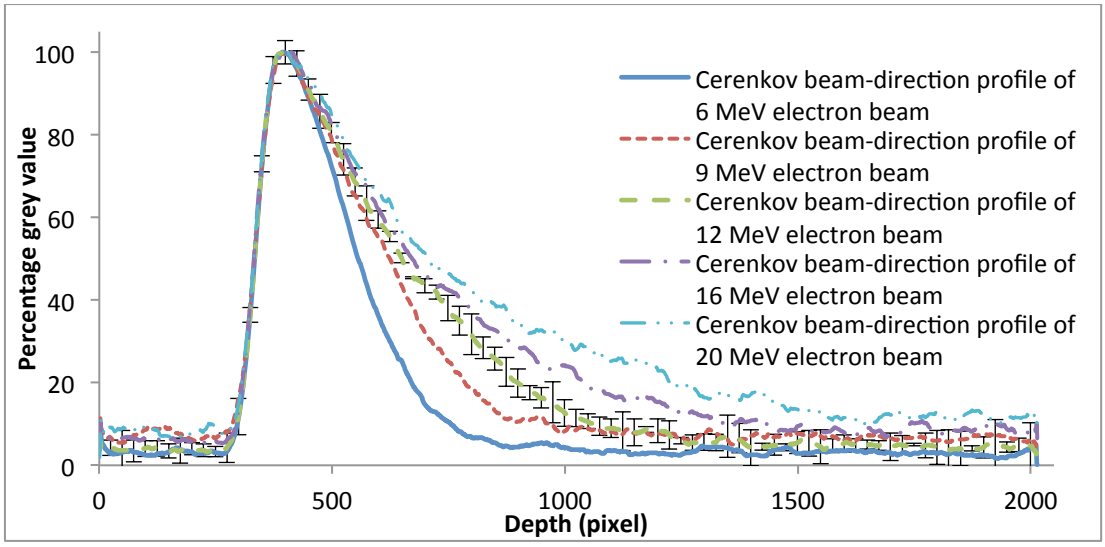

Figure 3.14 Beam-direction profiles for different electron energies. Error-bars shown are the standard deviation of 2 repeated readings of 12 MeV measurements.

3.2.3.4 Angular dependence

The angular dependence of Cerenkov measurement with the angle of the camera and the incident electron beam was measured (as explained in 3.2.2.4 and illustrated in Figure 3.10). Figure 3.15 shows the angular dependence in the Cerenkov images averaged over 50 pixels x 50 pixels, using a 12 MeV electron beam.

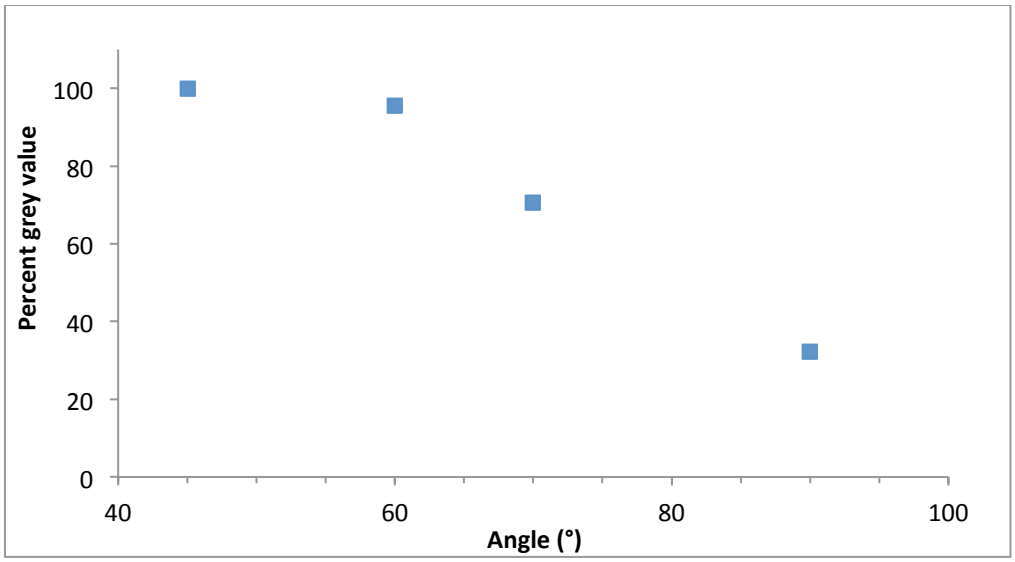

Figure 3.15 Angular dependence measurements using Cerenkov-electron method for 12 MeV electron beam. All measurements normalised to the 45 degrees measurement. The error bars (represent the standard deviation of 2 repeated readings) are smaller than the used point size.

As expected (as discussed in section 2.2.3), the maximum in light intensity found at angle 45.0° and decreases as the angle increases.

3.2.3.5 Imaging phantom with different optical properties

For each angle, the images of the inhomogeneous phantom were subtracted from the homogenous phantom images. Figure 3.16 shows images of the two phantoms for angle of 90 degrees and the subtracted image.

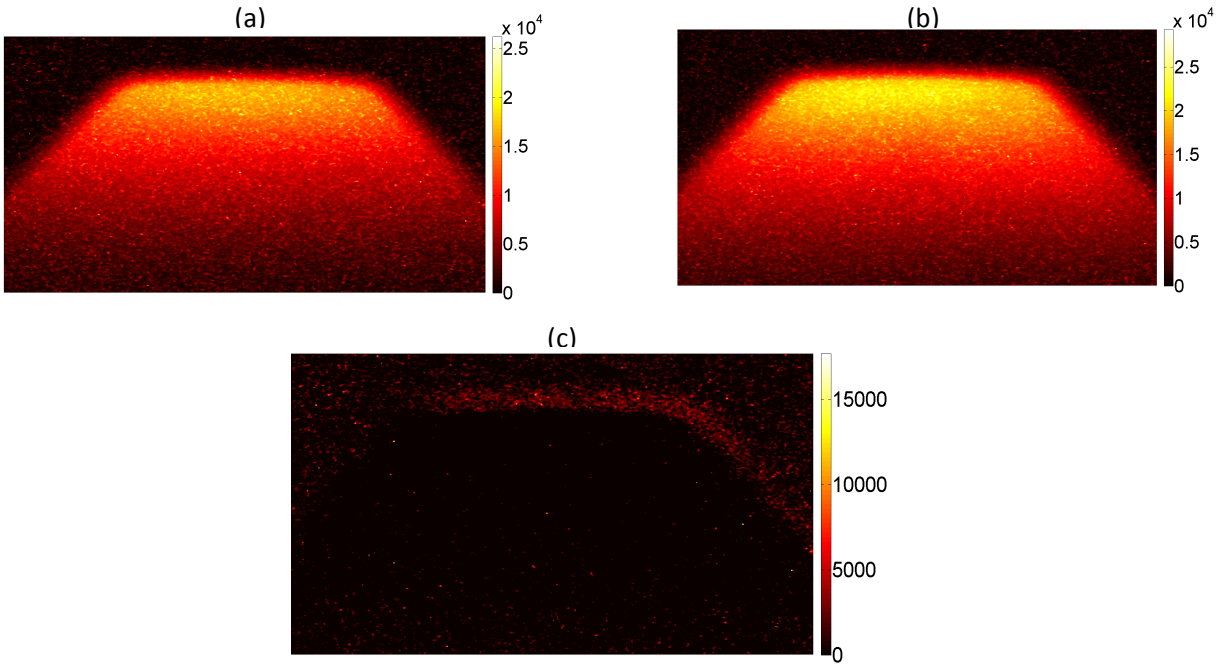

Figure 3.16 Digital images of Cerenkov light from 12 MeV electron beam, showing image of (a) homogenous phantom (b) inhomogeneous phantom (c) the subtraction between the two images.

It can be seen from Figure 3.16(c) that the inserts position couldn't be retrieved by the explained method. This due to: (i) the high absorption of the visible light inside the phantom, which confirmed by repeating the experiment and using the normal camera (with the infrared filter) and no light recorded; (ii) the high scattering pattern of the infrared radiation inside the phantom; (iii) the scattering pattern of electrons inside the phantom which is energy dependent and the angular dependency of Cerenkov production, which is also energy dependent.

3.3 Cerenkov light production during proton therapy

3.3.1 Objectives

Eye cancer patients frequently report a visual sensation during proton therapy. We believe that Cerenkov emission of visible photons is possible explanation of the observed light. Cerenkov emission takes place when charged particles move faster than the speed of light in a medium. The possibility of Cerenkov emission being the mechanism for the light sensation was investigated and the feasibility of measuring Cerenkov emission during proton therapy for monitoring the cyclotron beam output and as a dosimetry verification tool was explored.

In this work, light emission in proton therapy was examined and two different components of Cerenkov emission were identified: *(1)* a fast component, which is Cerenkov emission from prompt gamma and neutron interactions; and *(2)* a slow component, which is Cerenkov emission from positrons and electrons emitted by radioactive decay. Comparisons are made between the simulated and measured slow component of Cerenkov emission. The delivered doses and dose rates were correlated to the fast and slow components with a view to determining whether they can be used for online or offline verification. (Helo et al., 2014a)

3.3.2 Material and methods

All tests were carried out using the Douglas Cyclotron at the Clatterbridge Cancer Centre, using a proton energy of 60 MeV, with a 5 x 5 x 5 cm water phantom made from 1 mm thick Perspex; the distance between the collimator and the phantom face distance was 7.2 cm. The Cerenkov light was measured using a photomultiplier tube (PMT) (H11890-210, Hamamatsu, Japan) equipped with a 2 m optical fibre, fixed 7 mm away from the water phantom wall, where the maximum light intensity was expected (Figure 2.30). The integration time of the PMT for all measurements was 1 second in continuous mode. All measurements were subjected to a background subtraction that was obtained in the same lighting conditions but with the beam turned off. All light sources in the room were either turned off or blocked by a black, light-tight sheet during the experiments. (Helo et al., 2014a)

The PMT was remotely controlled from outside the cyclotron room by a PC and a 25 m USB cable. The PMT setup is shown in Figure 3.17. The PMT was placed at 90° with respect to the incident proton beam. (Helo et al., 2014a)

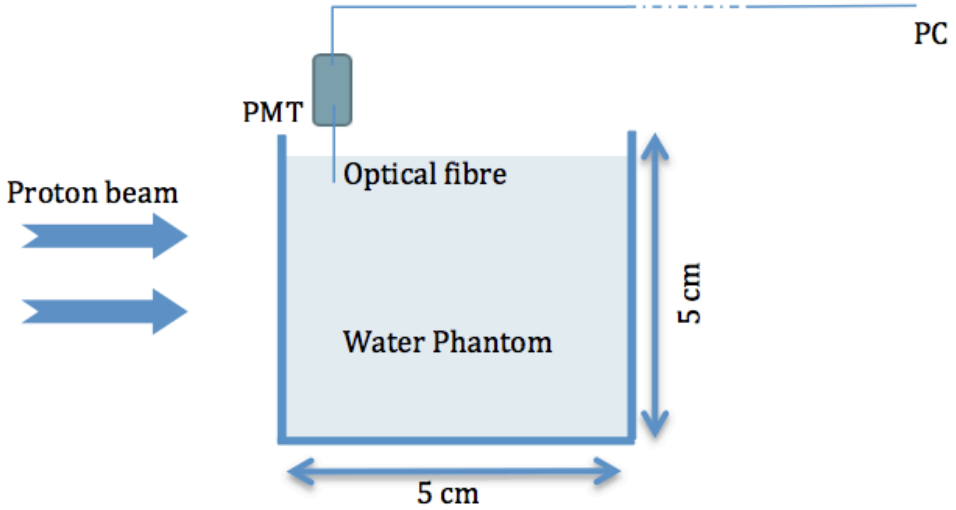

Figure 3.17 Experimental setup. (Helo et al., 2014a)

3.3.2.1 Time scale of slow component

Measurements were taken with a 20 x 20 mm^2 applicator, at a fixed dose rate of 5 Gy per minute and 60 MeV proton beam. Photons were recorded for 250 seconds after the beam was off. (Helo et al., 2014a)

3.3.2.2 Dose linearity

Measurements were taken with a 20 x 20 mm^2 applicator, at a fixed dose rate of 5 Gy per minute and 60 MeV proton beam. The dose linearity between 1.7 and 25 Gy was checked by summing the detected photons when the beam was on and by summing the detected photons for 20 seconds after the beam was off. Typical treatment fields deliver dose of about 13 Gy per fraction, depending on lesion type.

3.3.2.3 Dose rate dependence

Measurements were made with a 20 x 20 mm^2 collimator delivering 15 and 25 Gy with a 60 MeV proton beam. The dose rate dependence for 5 and 35 Gy/min was evaluated by summing the detected photons when the beam is on and by summing the detected photons after beam-off for 20 seconds. The dose rate of a typical treatment is 25 Gy/min.

3.3.3 Results and discussion

3.3.3.1 Time scale of slow component

The first 240 s of simulated (Figure 2.32) and experimental slow components of Cerenkov emissions are compared in Figure 3. 18. The simulated and experimental data are normalised to their own maximum value. (Helo et al., 2014a)

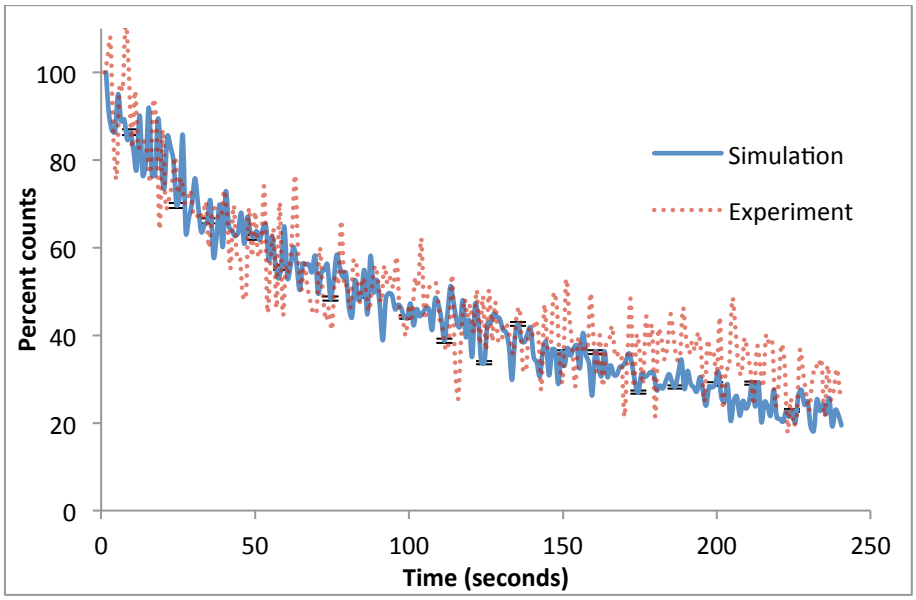

Figure 3.18 Slow component of Cerenkov emission from experimental and simulated results. The experiment delivered 15 Gy (where 15 Gy ≈ 1.95 x 10^{11} protons) at a high dose rate, whilst the simulation used 10^7 protons. (Helo et al., 2014a)

The simulated slow component was included in Figure 3.18 for reader convenience and making the comparison between the simulation and the experiment easier.

3.3.3.2 Linearity between Cerenkov measurements and dose

The relationship of the PMT response to dose was examined by delivering different doses to the water phantom and measuring the emitted Cerenkov light. Figures 3.19 and 3.20 show the dose linearity of the fast and slow component of Cerenkov measurements respectively, using a 60 MeV proton beam. (Helo et al., 2014a)

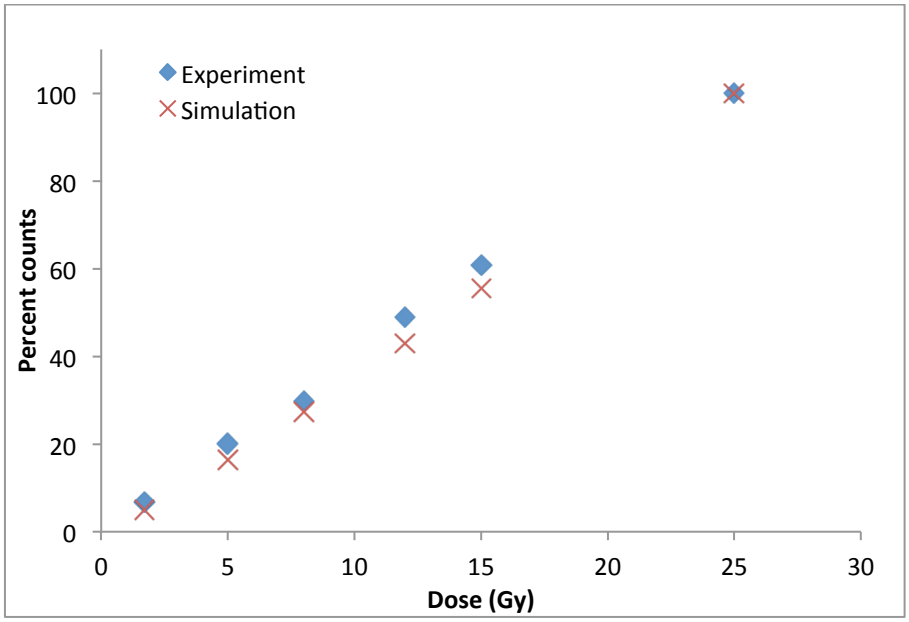

Figure 3.19 Demonstration of dose linearity from 1.7 to 25 Gy with a 60 MeV beam by measuring and simulating the fast component of Cerenkov production. All measurements were normalized to 25 Gy. (Helo et al., 2014a)

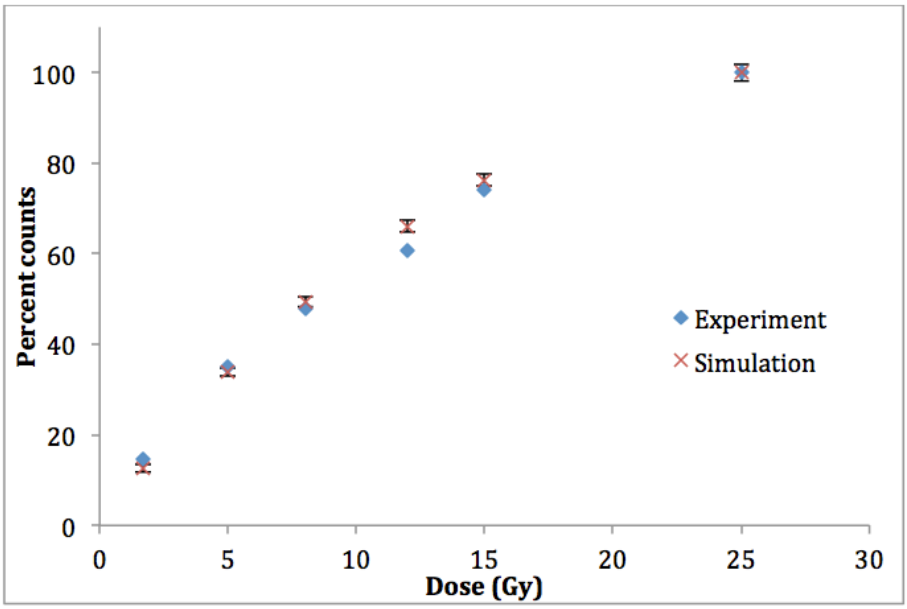

Figure 3.20 Demonstration of dose linearity from 1.7 to 25 Gy with a 60 MeV beam by measuring and simulating the slow component of Cerenkov production. All measurements were normalized to the 25 Gy. Error-bars show the standard deviation of the simulation data. (Helo et al., 2014a)

As the measurements of the fast component took place when the irradiation is on, the measured signal is a combination of the fast and slow components. The contribution of the slow component varies between 0.17% and 26.63% depends on the extended time required to deliver a given dose (as explained in section 2.3.5.1). The slight disagreement between the simulation and experiment could be due Cerenkov photons generated inside the fibre from gamma interaction and the scintillation light of the phantom walls.

It was found that the slow component is non-linear with dose arises from the extended time required to deliver a given dose. Therefore, any radionuclides, which are generated at the start of the beam delivery, will have begun to decay by the end of the irradiation time, reducing the measured count rate from higher doses (and therefore longer delivery times). The good agreement between experiment and simulation supports the suggestion that the non-linearity is due to decay rather than other potential mechanisms such as molecular diffusion. (Helo et al., 2014a)

3.3.3.3 Dependence of Cerenkov measurements on dose rate

The linearity of the detected Cerenkov emissions with dose rate was measured by delivering two different dose rates and measuring the emitted Cerenkov light. Figures 3.21 and 3.22 show the dose

rate dependence of the fast and slow components of Cerenkov measurements respectively, using a 60 MeV proton beam.

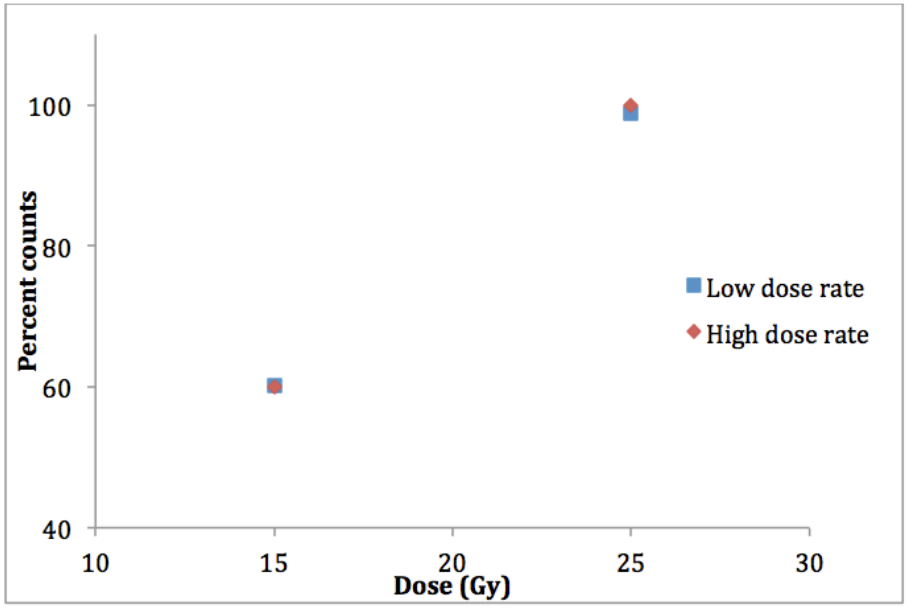

Figure 3.21 Dose rate measurements using the fast component of Cerenkov emission. The variation is less than 1.2%. All measurements are normalized to the high dose rate measurement at 25 Gy. The typical error-bars of the data are smaller than the size of the points.

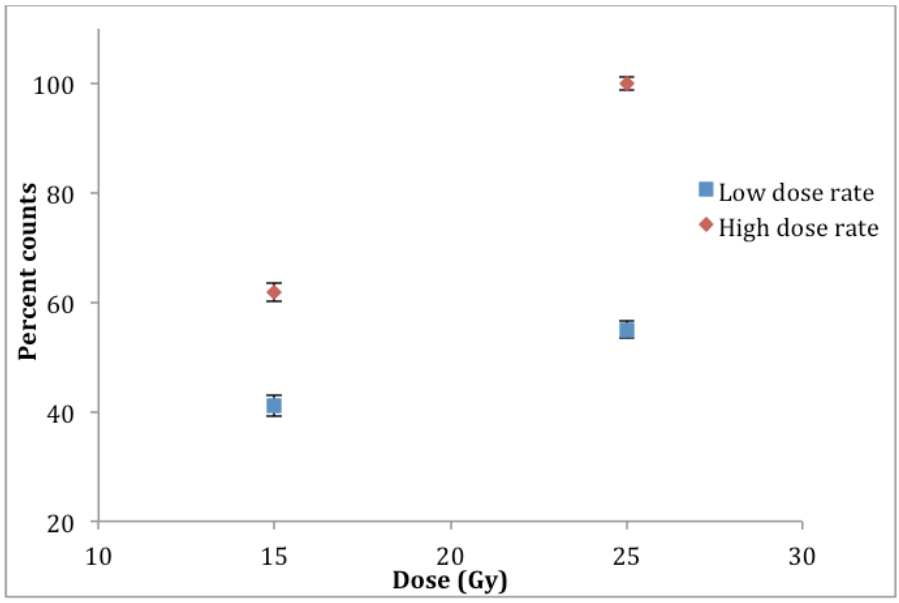

Figure 3.22 Dose rate measurements using the slow component of Cerenkov emission. All measurements are normalized to the high dose rate measurement at 25 Gy. Error-bars show the typical statistical standard deviation of the experimental data.

The variation with the dose rate was less than 1.2% for the fast component, compared to 45% with slow component due to the long time required to deliver the same amount of dose with low dose rate (257 seconds). Consequently, almost two half-lives of ^{15}O radionuclide have already passed before measurement begins.

The linearity of the dose rate was evaluated with only two points. Because 1. The time in the proton facility was very limited and 2. We were satisfied with the linearity of the dose with Cerenkov measurements (Figure 3.19 and 3.20), which showed behaviour consistent with the linearity of dose rate.

Chapter 4

CONCLUSION

4.1 Imaging Cerenkov emission as a quality assurance tool in electron radiotherapy

A new potential quality assurance (QA) method for clinical electron beams was explored by measuring Cerenkov light from a therapeutic electron beam in a water tank. The light was imaged using a commercial camera which was sensitive enough to detect Cerenkov light in electron therapy.

A clinical electron beam in a water tank was modeled using a quasi-Gaussian electron energy spectrum and beam divergence and the resulting Cerenkov emissions were simulated. The implemented pinhole code was able to reproduce the experimental Cerenkov images taken at UCLH for different energies. By scoring the Cerenkov production profile along with the deposited energy, we were able to define the relation between them.

The short term repeatability of all measurements was found to be better than 1% except when measuring very low doses. Cerenkov light measurements were linear with dose and independent of dose rate.

Cerenkov beam-direction profiles were different from the depth dose profiles due to the factors mentioned in sections 3.1.3.3 and 2.2.6.1. By applying an in-house vignetting correction factor, the range could be retrieved with a maximum discrepancy of 3mm. Since the source of the discrepancy is a known geometrical effect, the differences between Cerenkov and depth dose ranges are expected to be constant for the same set-up, so this method can still be used to monitor any changes in beam energy. The beam-direction profiles were practically independent of field size.

Similarly, there was a difference between transverse profiles measured from Cerenkov images and the ionization chamber due to the magnification effects. However, Cerenkov profiles and ionization profiles meet at 50% level, so this method can still be used to monitor any changes in beam width.

In summary we found that imaging Cerenkov light during radiotherapy QA could be a suitable tool to measure dose and dose rate constancy with high precision. Beam-direction profiles and transverse profiles could be used as a very quick routine QA tool to check range and field width constancy of electron beams. (Helo et al., 2014d)

4.2 Imaging Cerenkov emission in conical phantom with tissue-equivalent optical properties

The potential of using a standard commercial camera, which has the infrared filter removed, to image Cerenkov emission generated from electrons in breast like optical phantom for verification during breast treatment was explored. Our aim was primarily to detect infrared photons because the phantom is not transparent and visible photons don't come out.

Cerenkov light measurements were linear with dose and independent of dose rate. The maximum in light intensity found at angle 45.0° and decreases with increases the angle of the camera and the incident electron beam.

We couldn't utilize Cerenkov image to detect and identify cylinders with relative optical properties (representing cancerous cells) placed inside a conical phantom (representing human breast), primary due to the scattering of the infrared emission inside the phantom. However, imaging Cerenkov emission still useful to monitor the dose on the skin of the patient in real time

4.3 Cerenkov light production during proton therapy and its potential application as a quality assurance tool

Eye cancer patients who are being treated at the Clatterbridge proton centre frequently report the sensation of blue-ish light during treatment. We found that a therapeutic proton beam is capable of producing Cerenkov light. Cerenkov emissions during proton therapy can be divided into fast and slow components. The fast component is a result of prompt gamma ray interactions, while the slow component is a result of decay emissions of different induced radioisotopes. We propose that the dominant mechanism for the observed visual sensation is Cerenkov photons.

The fast component of Cerenkov emissions could be used to monitor the cyclotron beam output by measuring the light with a very fast PMT (in the nanosecond range). We found the fast component is linear with dose and independent of dose rate, while the slow component is less linear with dose and dependent on dose rate. However, as the Cerenkov fast signal occurs during irradiation, measuring it separately would be challenging as it is mixed with the slow component.

Nevertheless, the simulated depth profile of Cerenkov emission confirms the possibility of using the slow component to verify the range of the proton beam mainly from ^{15}O radionuclides.

Consequently, Cerenkov emissions could be used potentially as post treatment verification in certain cases of proton therapy, by imaging the light distribution of Cerenkov light, which would identify the dose localization. The possibility exists that this could be used as dosimetry verification tool during treatment. (Helo et al., 2014a)

4.3.1 Potential applications

4.3.1.1 Quality assurance

Measuring the fast component of Cerenkov production with a PMT may lead to a new way of monitoring the cyclotron beam output. Currently, an ionization chamber located in the path of the proton beam is used for this purpose. A water chamber, the same size as the ionization chamber coated from inside to reflect the light to one point to maximize the light output, connected to a PMT could be used to check the cyclotron output consistency as an independent secondary dosimeter for high energy particles. The water chamber walls can be can be a few mm thick and therefore have minimal impact on the beam characteristics. Scintillators have been proposed for similar applications in ion therapy (Archambault et al., 2008). However, unlike a Cerenkov-based system, they suffer from a Bragg peak quenching effect and are not water equivalent (Torrisi, 2000).

Proton range measurements are essential in proton therapy and are currently performed for QA by an ionization chamber scanning the water phantom. We propose that measuring Cerenkov production from mainly ^{15}O emissions, using a camera or bundle of optical fibres, could considerably reduce the time required to measure the Bragg peak range by taking advantage of the relation between radioactivity and range.

4.3.1.2 Treatment verifications

As well as providing potential new techniques for QA, measuring Cerenkov production in tissue could lead to a method for online monitoring of the dose deposited by the proton beam, potentially providing real-time verification of any changes in dose during the treatment session. The emitted intensity of Cerenkov light from tissue is less than that of water because most of the optical

photons will be absorbed by the tissue. However, the Cerenkov emission spectrum extends to the near infrared regions where more photons will penetrate tissue and could then be detected.

PET imaging of positron-emitting isotopes is being developed as a tool for post-verification treatment to confirm the irradiation field. However, there are disadvantages in using PET in proton therapy, most of them related to time in moving the patient to the PET room, the biological washout, and cost (Zhu et al., 2011). Imaging the Cerenkov emission following the introduction of positron-emitting isotopes is being developed as Cerenkov luminescence tomography of small animals (Li et al., 2010). We are investigating the possibility that in-vivo imaging of the slow component of Cerenkov production in tissue could provide a new imaging method for treatment verification.

A potential clinical application specific to proton therapy is in-vivo imaging of the slow component of Cerenkov production in the human eye for treatment verification, where penetration is low and the tissue is transparent.

Finally, measuring Cerenkov emissions in tissue in radiation therapy has been proposed as a method for measuring haemoglobin oxygen saturation by exploiting the differential absorption of the Cerenkov light as a function of wavelength, using techniques pioneered in near infrared spectroscopy (Axelsson et al., 2012). The role of tissue oxygenation in radiotherapy effectiveness is well known (Harrison and Blackwell, 2004). (Helo et al., 2014a)

Appendices

Appendix 1: Maximum energy lost by protons in Coulomb interactions

The purpose of this appendix is to calculate the maximum energy of proton can lose by colliding with an atomic electron, assuming that the binding energy of the atomic electron is negligible, comparing with the proton energy. Under this condition, electrons are considered to be initially free and at rest.

Kinetic energy conservation law:

$$\frac{1}{2}MV^2 = \frac{1}{2}MV_1^2 + \frac{1}{2}mv_1^2 \qquad (1)$$

where M: mass of proton, V: velocity of proton before collision, V_1: velocity of proton after collision, m: mass of electron, v_1: velocity of electron after collision.

Momentum conservation law,

$$MV = MV_1 + mv_1 \qquad (2)$$

from (1) and (2) we can show that,

$$V_1 = \frac{(M-m)V}{M+m} \qquad (3)$$

Maximum energy transfer in signal collision is

$$\Theta_{Max} = \frac{1}{2} MV^2 - \frac{1}{2} MV_1^2 \qquad (4)$$

considering $\frac{m}{M} = \frac{1}{1836}$. Therefore,

$$\Theta_{Max} = \frac{4mME}{(M+m)^2} \approx \frac{1}{459} E$$

Appendix 2: β⁺ decay

β^+ decay is a process by which a proton (p) in a nucleus transforms into a neutron (n), involving the spontaneous emission of positron (e^+) and neutrino (υ_e) within the nucleus as explained in equation 1.

$$p \rightarrow n + e^+ + \upsilon_e \quad (1)$$

The spectrum of beta decay is continuous, because the energy released in beta decay is randomly shared between the beta particle and the neutrino (Levin and Hoffman, 1999). The theoretical distribution of energy spectrum for beta decays is shown in equation 2,

$$N'(E)\mathrm{d}E = gF(Z,E)pE(E_{max} - E)^2\mathrm{d}E \quad (2)$$

where $N'(E)$ is the number of decays emitted at energy *E*, *g* is the coupling constant, E_{max} is the maximum energy of *β* particle in units of mc^2, *p* is the momentum of *β* particle in units of *mc*, *F(Z,E)* is Fermi function which takes into account the Coulomb interaction between beta particle and daughter nucleus. $F_{allowed}(Z,E) = \frac{2\pi\mu}{1-e^{-2\pi\mu}}$ with $\mu = -\frac{Z\alpha E}{p}$ for positron decay and $\alpha = \frac{1}{137}$ is the fine structure constant (Levin and Hoffman, 1999; Parodi et al., 2008).

The theoretical energy spectra for the three isotopes of interest (considering the target is human tissue) are shown in Figure 1.

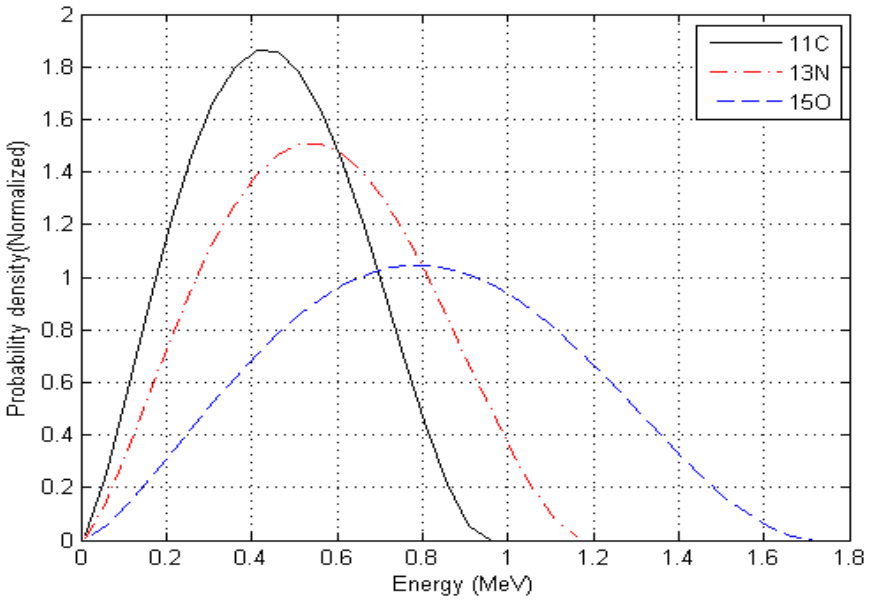

Figure 1 Theoretical positron kinetic energy spectra for ^{11}C, ^{13}N and ^{15}O (normalized to have equal area under the curves). Drawn using equation 2 in matlab.

Appendix 3: Radiation damage in CCD camera

CCTV is in operation in all linear accelerator treatment room to monitor patients during the treatment. Many researches were engaged to investigate the radiation damage to the camera in the treatment room (Kok, 2005).

Radiation damage in the CCD camera may be caused by two different methods.

Low energy radiation (photons and electrons) transfers only a small fraction of its energy to the Si atom (CCD chip). The Si atom will be ionized for a while, and then the excited electron will recoil to its position. However, the silicon oxide insulator, which covers the Si chip, can trap the excited electrons. The trapped electrons induce a permanent charge to the pixel (which called surface damage). The result of the surface damage is an increase in dark current. In the market, there are radiation-hardened CCDs which are less sensitive to the surface damage (by reducing the thickness of the silicon oxide insulator) (Kok, 2005).

Intermediate and high energy neutrons could pick out the silicon atoms from their positions within the crystal lattice. These faults (called Bulk damage) generate a large local electric field that results in hot pixels. These hot pixels have a constant high signal and can be seen as bright dots in the images (Kok, 2005).

For measuring the radiation surface damage in the camera, dark counts measurement should be carried out before the experiment day and after the experiment day. Unfortunately, we didn't record the dark counts before the experiment day, but we recorded the dark counts for the camera after one hour of the experiment and after 24 hours. The mean, the standard deviation and the number of pixels above a given threshold (20 grey values) are illustrated in the following table.

Time of measurement	Mean	STD	Pixels value>20
After 1 hour	1.45	1.98	76
After 24 hours	1.63	2.12	79

The number of pixels, which found higher than 20 grey values, is low comparing with (Kok, 2005). Which indicate there was no noticeable Bulk damage in the used camera.

References

Agostinelli, S., Allison, J., Amako, K., Apostolakis, J., Araujo, H., Arce, P., Asai, M., Axen, D., Banerjee, S., Barrand, G., Behner, F., Bellagamba, L., Boudreau, J., Broglia, L., Brunengo, A., Burkhardt, H., Chauvie, S., Chuma, J., Chytracek, R., Cooperman, G., Cosmo, G., Degtyarenko, P., Dell'Acqua, A., Depaola, G., Dietrich, D., Enami, R., Feliciello, A., Ferguson, C., Fesefeldt, H., Folger, G., Foppiano, F., Forti, A., Garelli, S., Giani, S., Giannitrapani, R., Gibin, D., Gómez Cadenas, J.J., González, I., Gracia Abril, G., Greeniaus, G., Greiner, W., Grichine, V., Grossheim, A., Guatelli, S., Gumplinger, P., Hamatsu, R., Hashimoto, K., Hasui, H., Heikkinen, A., Howard, A., Ivanchenko, V., Johnson, A., Jones, F.W., Kallenbach, J., Kanaya, N., Kawabata, M., Kawabata, Y., Kawaguti, M., Kelner, S., Kent, P., Kimura, A., Kodama, T., Kokoulin, R., Kossov, M., Kurashige, H., Lamanna, E., Lampén, T., Lara, V., Lefebure, V., Lei, F., Liendl, M., Lockman, W., Longo, F., Magni, S., Maire, M., Medernach, E., Minamimoto, K., Mora de Freitas, P., Morita, Y., Murakami, K., Nagamatu, M., Nartallo, R., Nieminen, P., Nishimura, T., Ohtsubo, K., Okamura, M., O'Neale, S., Oohata, Y., Paech, K., Perl, J., Pfeiffer, A., Pia, M.G., Ranjard, F., Rybin, A., Sadilov, S., Di Salvo, E., Santin, G., Sasaki, T., Savvas, N., Sawada, Y., Scherer, S., Sei, S., Sirotenko, V., Smith, D., Starkov, N., Stoecker, H., Sulkimo, J., Takahata, M., Tanaka, S., Tcherniaev, E., Safai Tehrani, E., Tropeano, M., Truscott, P., Uno, H., Urban, L., Urban, P., Verderi, M., Walkden, A., Wander, W., Weber, H., Wellisch, J.P., Wenaus, T., Williams, D.C., Wright, D., Yamada, T., Yoshida, H., Zschiesche, D., 2003. Geant4—a simulation toolkit. Nucl. Instrum. Methods Phys. Res. Sect. Accel. Spectrometers Detect. Assoc. Equip. 506, 250–303. doi:10.1016/S0168-9002(03)01368-8

Anderson, D.E., Skinner, P.E., 1961. Studies on Bovine Ocular Squamous Carcinoma ("Cancer Eye") XI. Effects of Sunlight. J. Anim. Sci. 20, 474–477.

Andreo, P., Huq, M.S., Westermark, M., Song, H., Tilikidis, A., DeWerd, L., Shortt, K., 2002. Protocols for the dosimetry of high-energy photon and electron beams: a comparison of the IAEA TRS-398 and previous international Codes of Practice. Phys. Med. Biol. 47, 3033. doi:10.1088/0031-9155/47/17/301

Archambault, L., Polf, J.C., Beaulieu, L., Beddar, S., 2008. Characterizing the response of miniature scintillation detectors when irradiated with proton beams. Phys. Med. Biol. 53, 1865. doi:10.1088/0031-9155/53/7/004

Avdeev, S., Bidoli, V., Casolino, M., De Grandis, E., Furano, G., Morselli, A., Narici, L., De Pascale, M.P., Picozza, P., Reali, E., Sparvoli, R., Boezio, M., Carlson, P., Bonvicini, W., Vacchi, A., Zampa, N., Castellini, G., Fuglesang, C., Galper, A., Khodarovich, A., Ozerov, Y., Popov, A., Vavilov, N., Mazzenga, G., Ricci, M., Sannita, W.G., Spillantini, P., 2002. Eye light flashes on the mir space station. Acta Astronaut. 50, 511–525. doi:10.1016/S0094-5765(01)00190-4

Axelsson, J., Davis, S.C., Gladstone, D.J., Pogue, B.W., 2011. Cerenkov emission induced by external beam radiation stimulates molecular fluorescence. Med. Phys. 38, 4127–4132. doi:10.1118/1.3592646

Axelsson, J., Glaser, A.K., Gladstone, D.J., Pogue, B.W., 2012. Quantitative Cherenkov emission spectroscopy for tissue oxygenation assessment. Opt. Express 20, 5133. doi:10.1364/OE.20.005133

Beddar, A.S., 2006. Plastic scintillation dosimetry and its application to radiotherapy. Radiat. Meas., The 2nd Summer School on Solid State Dosimetry: Concepts and Trends in Medical Dosimetry 41, Supplement 1, S124–S133. doi:10.1016/j.radmeas.2007.01.002

Bedford, J.L., Lee, Y.K., Wai, P., South, C.P., Warrington, A.P., 2009. Evaluation of the Delta4 phantom for IMRT and VMAT verification. Phys. Med. Biol. 54, N167. doi:10.1088/0031-9155/54/9/N04

Beebe-Wang, J., Vaska, P., Dilmanian, F.A., Peggs, S.G., Schlyer, D.J., 2003. Simulation of proton therapy treatment verification via PET imaging of induced positron-emitters, in: 2003 IEEE Nuclear Science Symposium Conference Record. Presented at the 2003 IEEE Nuclear Science Symposium Conference Record, IEEE, pp. 2496– 2500 Vol.4. doi:10.1109/NSSMIC.2003.1352399

Binder, K., Heermann, D., 2010. Monte Carlo Simulation in Statistical Physics: An Introduction. Berlin: Springer.

Boggula, R., Lorenz, F., Mueller, L., Birkner, M., Wertz, H., Stieler, F., Steil, V., Lohr, F., Wenz, F., 2010. Experimental validation of a commercial 3D dose verification system for intensity-modulated arc therapies. Phys. Med. Biol. 55, 5619. doi:10.1088/0031-9155/55/19/001

Bom, V., Joulaeizadeh, L., Beekman, F., 2012. Real-time prompt γ monitoring in spot-scanning proton therapy using imaging through a knife-edge-shaped slit. Phys. Med. Biol. 57, 297–308. doi:10.1088/0031-9155/57/2/297

Bonnett, D.E., Kacperek, A., Sheen, M.A., Goodall, R., Saxton, T.E., 1993. The 62 MeV Proton Beam for the Treatment of Ocular Melanoma at Clatterbridge. Br. J. Radiol. 66, 907–914. doi:10.1259/0007-1285-66-790-907

Bowmaker, J.K., Dartnall, H.J., 1980. Visual pigments of rods and cones in a human retina. J. Physiol. 298, 501–511.

Brada, M., Pijls-Johannesma, M., Ruysscher, D.D., 2007. Proton Therapy in Clinical Practice: Current Clinical Evidence. J. Clin. Oncol. 25, 965–970. doi:10.1200/JCO.2006.10.0131

Bucciolini, M., Buonamici, F.B., Casati, M., 2003. Verification of IMRT fields by film dosimetry. Med. Phys. 31, 161–168. doi:10.1118/1.1631093

Burden, D.L., Hieftje, G.M., 1998. Çerenkov Radiation as a UV and Visible Light Source for Time-Resolved Fluorescence. Anal. Chem. 70, 3426–3433. doi:10.1021/ac980016w

Caccia, B., Mattia, M., Amati, G., Andenna, C., Benassi, M., d' Angelo, A., Frustagli, G., Iaccarino, G., Occhigrossi, A., Valentini, S., 2007. Monte Carlo in radiotherapy: experience in a distributed computational environment. J. Phys. Conf. Ser. 74, 021001. doi:10.1088/1742-6596/74/1/021001

Chadwick, M.B., Herman, M., Obložinský, P., Dunn, M.E., Danon, Y., Kahler, A.C., Smith, D.L., Pritychenko, B., Arbanas, G., Arcilla, R., Brewer, R., Brown, D.A., Capote, R., Carlson, A.D., Cho, Y.S., Derrien, H., Guber, K., Hale, G.M., Hoblit, S., Holloway, S., Johnson, T.D., Kawano, T., Kiedrowski, B.C., Kim, H., Kunieda, S., Larson, N.M., Leal, L., Lestone, J.P., Little, R.C., McCutchan, E.A., MacFarlane, R.E., MacInnes, M., Mattoon, C.M., McKnight, R.D., Mughabghab, S.F., Nobre, G.P.A., Palmiotti, G., Palumbo, A., Pigni, M.T., Pronyaev, V.G., Sayer, R.O., Sonzogni, A.A., Summers, N.C., Talou, P., Thompson, I.J., Trkov, A., Vogt, R.L., van der Marck, S.C., Wallner, A., White, M.C., Wiarda, D., Young, P.G., 2011. ENDF/B-VII.1 Nuclear Data for Science and Technology: Cross Sections, Covariances, Fission Product Yields and Decay Data. Nucl. Data Sheets 112, 2887–2996. doi:10.1016/j.nds.2011.11.002

Cho, J.S., Taschereau, R., Olma, S., Liu, K., Chen, Y.-C., Shen, C.K.-F., van Dam, R.M., Chatziioannou, A.F., 2009. Cerenkov radiation imaging as a method for quantitative measurements of beta particles in a microfluidic chip. Phys. Med. Biol. 54, 6757–6771. doi:10.1088/0031-9155/54/22/001

Cleland, M., Lisanti, T., Galloway, R., 2004. Comparisons of Monte Carlo and ICRU electron energy vs. range equations. Radiat. Phys. Chem. 71, 585–589. doi:10.1016/j.radphyschem.2004.04.078

Danciu, C., B. S. Proimos, J. C. Rosenwald, and B. J. Mijnheer. 2001. Variation of Sensitometric Curves of Radiographic Films in High Energy Photon Beams. Medical Physics 28 (6): 966–74.

Fiedler, F., Dersch, U., Golnik, C., Kormoll, T., Muller, A., Rohling, H., Schone, S., Enghardt, W., 2011. The use of prompt #x03B3;-rays for in-vivo dosimetry at therapeutic proton and ion beams, in: 2011 IEEE Nuclear Science Symposium and Medical Imaging Conference (NSS/MIC). Presented at the 2011 IEEE Nuclear Science Symposium and Medical Imaging Conference (NSS/MIC), pp. 4453–4456. doi:10.1109/NSSMIC.2011.6152493

Firbank, M., Oda, M., Delpy, D.T., 1995. An improved design for a stable and reproducible phantom material for use in near-infrared spectroscopy and imaging. Phys. Med. Biol. 40, 955. doi:10.1088/0031-9155/40/5/016

Fuglesang, C., 2007. Using the human eye to image space radiation or the history and status of the light flash phenomena. Nucl. Instrum. Methods Phys. Res. Sect. Accel. Spectrometers Detect. Assoc. Equip., Imaging 2006 Proceedings of the 3rd International Conference on Imaging Techniques in Subatomic Physics, Astrophysics, Medicine, Biology and Industry 580, 861–865. doi:10.1016/j.nima.2007.06.095

Geant4 User's Guide for Application Developers. 2012. Geneva: Geant4 Publications.

Geant4 Physics Reference Manual, physics group. 2012. Geneva: Geant4 Publications.

Glaser, A.K., Davis, S.C., McClatchy, D.M., Zhang, R., Pogue, B.W., Gladstone, D.J., 2013. Projection imaging of photon beams by the Cerenkov effect. Med. Phys. 40, 012101. doi:10.1118/1.4770286

Glaser, A.K., Kanick, S.C., Zhang, R., Arce, P., Pogue, B.W., 2013. A GAMOS plug-in for GEANT4 based Monte Carlo simulation of radiation-induced light transport in biological media. Biomed. Opt. Express 4, 741–759. doi:10.1364/BOE.4.000741

Green, D., 2000. The Physics of Particle Detectors. Cambridge University Press.

Hale, G.M., Querry, M.R., 1973. Optical Constants of Water in the 200-nm to 200-µm Wavelength Region. Appl. Opt. 12, 555–563. doi:10.1364/AO.12.000555

Halperin, E.C., Brady, L.W., Perez, C.A., Wazer, D.E., 2013. Perez & Brady's Principles and Practice of Radiation Oncology. Lippincott Williams & Wilkins.

Harrison, L., Blackwell, K., 2004. Hypoxia and Anemia: Factors in Decreased Sensitivity to Radiation Therapy and Chemotherapy? The Oncologist 9, 31–40. doi:10.1634/theoncologist.9-90005-31

Hebden, J.C., Veenstra, H., Dehghani, H., Hillman, E.M., Schweiger, M., Arridge, S.R., Delpy, D.T., 2001. Three-dimensional time-resolved optical tomography of a conical breast phantom. Appl. Opt. 40, 3278–3287.

Hecht, S., Shlaer, S., Pirenne, M.H., 1942. Energy, Quanta, and Vision. J. Gen. Physiol. 25, 819–840. doi:10.1085/jgp.25.6.819

Helo, Y., 2010. Evaluation of the PTW Octavius Phantom as a Tool for VMAT Verification. MSc. Thesis. University of Surrey: UK.

Helo, Y., A. Kacperek, I. Rosenberg, G. Royle, and A. P. Gibson. 2014a. The Physics of Cerenkov Light Production During Proton Therapy. Physics in Medicine and Biology 59 (23): 7107. doi:10.1088/0031-9155/59/23/7107.

Helo, Y., Rosenberg, I., D'Souza, D., MacDonald, L., Speller, R., Royle, G., Gibson, A., 2014d. Imaging Cerenkov emission as a quality assurance tool in electron radiotherapy. Phys. Med. Biol. 59, 1963. doi:10.1088/0031-9155/59/8/1963

Helo, Y., Rosenberg, I., Kacperek, A., D'Souza, D., MacDonald, L., Dixon, E., Speller, R., Royle, G., Gibson, A., 2014e. Cerenkov optical emissions in particle radiotherapy, in: Biomedical Optics 2014, OSA Technical Digest (online). Presented at the Biomedical Optics 2014, Optical Society of America, p. BM4A.6. doi:10.1364/BIOMED.2014.BM4A.6

Hishikawa, Y., Kagawa, K., Murakami, M., Sakai, H., Akagi, T., Abe, M., 2002. Usefulness of positron-emission tomographic images after proton therapy. Int. J. Radiat. Oncol. 53, 1388–1391. doi:16/S0360-3016(02)02887-0

Jang, K.W., Yoo, W.J., Moon, J., Han, K.T., Park, J.-Y., Lee, B., 2012a. Measurements of relative depth doses and Cerenkov light using a scintillating fiber–optic dosimeter with Co-60 radiotherapy source. Appl. Radiat. Isot. 70, 274–277. doi:10.1016/j.apradiso.2011.08.005

Jang, K.W., Yoo, W.J., Shin, S.H., Shin, D., Lee, B., 2012b. Fiber-optic Cerenkov radiation sensor for proton therapy dosimetry. Opt. Express 20, 13907–13914. doi:10.1364/OE.20.013907

Jelley, J.V., 1958. Cerenkov radiation and its applications. London: Pergamon Press.

Kacperek, A., 2009. Protontherapy of eye tumours in the UK: A review of treatment at Clatterbridge. Appl. Radiat. Isot. 67, 378–386. doi:10.1016/j.apradiso.2008.06.012

Kacperek, A., Bonnett, D.E., 1990. Development of a Faraday cup for proton beam dosimetry at the MRC Cyclotron Unit at Clatterbridge Hospital. Proc. Int. Heavy Particle Therapy Workshop (PSI, 18–20 Sept. 1989) (Villigen) pp 53–6.

Kasarova, S.N., Sultanova, N.G., Ivanov, C.D., Nikolov, I.D., 2007. Analysis of the dispersion of optical plastic materials. Opt. Mater. 29, 1481–1490. doi:10.1016/j.optmat.2006.07.010

Khan, E., Maréchal, F., Dendale, R., Mabit, C., Calugaru, V., Desjardin, L., Narici, L., 2010. Anomalous phosphenes in ocular protontherapy. Adv. Space Res., Life Sciences in Space 45, 846–849. doi:10.1016/j.asr.2009.11.021

Khan, F.M., 2012. The Physics of Radiation Therapy. Philadelphia: Lippincott Williams & Wilkins.

Knoll, G.F., 1988. Radiation Detection and Measurement, Second Edition. ed. New York: John Wiley & Sons.

Knoll, G.F., 2010. Radiation Detection and Measurement. New York: John Wiley & Sons.

Kok, J.G.M., 2005. Low cost CCD camera protection against neutron radiation damage. J. Med. Eng. Technol. 29, 27–32. doi:10.1080/03091900410001701914

Kolb H, Fernandez E and Nelson R (eds) 1995 Webvision: the Organization of the Retina and Visual System (Salt Lake City, UT: University of Utah Health Sciences Center) www.ncbi.nlm.nih.gov/books/NBK11530/ (Accessed 25 March 2014)

Krane, K.S., Halliday, D., 1987. Introductory nuclear physics. New York: Wiley.

Kurosawa, S., Kubo, H., Ueno, K., Kabuki, S., Iwaki, S., Takahashi, M., Taniue, K., Higashi, N., Miuchi, K., Tanimori, T., Kim, D., Kim, J., 2012. Prompt gamma detection for range verification in proton therapy. Curr. Appl. Phys. 12, 364–368. doi:10.1016/j.cap.2011.07.027

L'Annunziata, M.F., 2007. Radioactivity: Introduction and History: Oxford, Elsevier.

L'Annunziata, M.F., 2012. Handbook of Radioactivity Analysis. Amsterdam: Academic Press.

Lambert, J., Yin, Y., McKenzie, D.R., Law, S., Suchowerska, N., 2009. Cerenkov light spectrum in an optical fiber exposed to a photon or electron radiation therapy beam. Appl. Opt. 48, 3362–3367. doi:10.1364/AO.48.003362

Lederman, M., 1981. The early history of radiotherapy: 1895–1939. Int. J. Radiat. Oncol. 7, 639–648. doi:10.1016/0360-3016(81)90379-5

Lefeuvre, G., Gorodetzky, P., Dolbeau, J., Patzak, T., Salin, P., 2007. Absolute measurement of the nitrogen fluorescence yield in air between 300 and 430 nm. Nucl. Instrum. Methods Phys. Res. Sect. Accel. Spectrometers Detect. Assoc. Equip. 578, 78–87. doi:10.1016/j.nima.2007.04.106

Levin, C.S., Hoffman, E.J., 1999. Calculation of positron range and its effect on the fundamental limit of positron emission tomography system spatial resolution. Phys. Med. Biol. 44, 781–799. doi:10.1088/0031-9155/44/3/019

Levin, W.P., Kooy, H., Loeffler, J.S., DeLaney, T.F., 2005. Proton beam therapy. Br. J. Cancer 93, 849–854. doi:10.1038/sj.bjc.6602754

Li, C., Mitchell, G.S., Cherry, S.R., 2010. Cerenkov luminescence tomography for small-animal imaging. Opt. Lett. 35, 1109–1111.

Li, G., Zhang, Y., Jiang, X., Bai, S., Peng, G., Wu, K., Jiang, Q., 2013. Evaluation of the ArcCHECK QA system for IMRT and VMAT verification. Phys. Med. 29, 295–303. doi:10.1016/j.ejmp.2012.04.005

Lomax, A.J., 2008. Intensity modulated proton therapy and its sensitivity to treatment uncertainties 1: the potential effects of calculational uncertainties. Phys. Med. Biol. 53, 1027–1042. doi:10.1088/0031-9155/53/4/014

Lomax, A.J., Boehringer, T., Coray, A., Egger, E., Goitein, G., Grossmann, M., Juelke, P., Lin, S., Pedroni, E., Rohrer, B., Roser, W., Rossi, B., Siegenthaler, B., Stadelmann, O., Stauble, H., Vetter, C., Wisser, L., 2001. Intensity modulated proton therapy: A clinical example. Med. Phys. 28, 317–324. doi:10.1118/1.1350587

Malmer, C.J., 2001. ICRU Report 63. Nuclear Data for Neutron and Proton Radiotherapy and for Radiation Protection. Med. Phys. 28, 861. doi:10.1118/1.1369116

Min, C.-H., Kim, C.H., Youn, M.-Y., Kim, J.-W., 2006. Prompt gamma measurements for locating the dose falloff region in the proton therapy. Appl. Phys. Lett. 89, 183517–183517–3. doi:10.1063/1.2378561

Newman, F., Asadi-Zeydabadi, M., Durairaj, V.D., Ding, M., Stuhr, K., Kavanagh, B., 2008. Visual sensations during megavoltage radiotherapy to the orbit attributable to Cherenkov radiation. Med. Phys. 35, 77. doi:10.1118/1.2815358

NIST Publication, 2013. ESTAR : Stopping Power and Range Tables for Electrons. National Institute of Standards and Technology, Gaithersburg MD, 20899.

Paganetti, H., 2011. Proton Therapy Physics, Series in Medical Physics and Biomedical Engineering. Boca Raton, FL: CRC Press.

Paganetti, H., 2012. Range uncertainties in proton therapy and the role of Monte Carlo simulations. Phys. Med. Biol. 57, R99. doi:10.1088/0031-9155/57/11/R99

Parodi, K., Bortfeld, T., Haberer, T., 2008. Comparison between in-beam and offline positron emission tomography imaging of proton and carbon ion therapeutic irradiation at synchrotron- and cyclotron-based facilities. Int. J. Radiat. Oncol. Biol. Phys. 71, 945–956. doi:10.1016/j.ijrobp.2008.02.033

Parodi, K., Paganetti, H., Shih, H.A., Michaud, S., Loeffler, J.S., DeLaney, T.F., Liebsch, N.J., Munzenrider, J.E., Fischman, A.J., Knopf, A., Bortfeld, T., 2007. Patient Study of In Vivo Verification of Beam Delivery and Range, Using Positron Emission

Tomography and Computed Tomography Imaging After Proton Therapy. Int. J. Radiat. Oncol. 68, 920–934. doi:10.1016/j.ijrobp.2007.01.063

Perl, J., 2003. Introduction to Geant4 Visualization.

Pflugfelder, D., Wilkens, J.J., Oelfke, U., 2008. Worst case optimization: a method to account for uncertainties in the optimization of intensity modulated proton therapy. Phys. Med. Biol. 53, 1689. doi:10.1088/0031-9155/53/6/013

Piermattei, A., Miceli, R., Azario, L., Fidanzio, A., Canne, S. delle, Angelis, C.D., Onori, S., Pacilio, M., Petetti, E., Raffaele, L., Sabini, M.G., 2000. Radiochromic film dosimetry of a low energy proton beam. Med. Phys. 27, 1655–1660. doi:10.1118/1.599032

Pimpinella, M., D. Mihailescu, A. S. Guerra, and R. F. Laitano. 2007. Dosimetric Characteristics of Electron Beams Produced by a Mobile Accelerator for IORT. Physics in Medicine and Biology 52 (20): 6197. doi:10.1088/0031-9155/52/20/008

Podgorsak, E.B., 2006. Radiation physics for medical physicists. Springer, Berlin; New York.

Polf, J.C., Panthi, R., Mackin, D.S., McCleskey, M., Saastamoinen, A., Roeder, B.T., Beddar, S., 2013. Measurement of characteristic prompt gamma rays emitted from oxygen and carbon in tissue-equivalent samples during proton beam irradiation. Phys. Med. Biol. 58, 5821. doi:10.1088/0031-9155/58/17/5821

Poppe, B., Blechschmidt, A., Djouguela, A., Kollhoff, R., Rubach, A., Willborn, K.C., Harder, D., 2006. Two-dimensional ionization chamber arrays for IMRT plan verification. Med. Phys. 33, 1005–1015. doi:10.1118/1.2179167

Portals, C. on A.S., Board, N. and R.S., Studies, D. on E. and L., Council, N.R., 2011. Evaluating Testing, Costs, and Benefits of Advanced Spectroscopic Portals for Screening Cargo at Ports of Entry: Interim Report (Abbreviated Version). National Academies Press.

Ray, S., 2002. Applied Photographic Optics: Lenses and Optical Systems for Photography, Film, Video and Digital Imaging, 3rd ed. Focal Press.

Righi, Sergio, Evis Karaj, Giuseppe Felici, and Fabio Di Martino. 2013. Dosimetric Characteristics of Electron Beams Produced by Two Mobile Accelerators, Novac7 and Liac, for Intraoperative Radiation Therapy through Monte Carlo Simulation. Journal of Applied Clinical Medical Physics 14 (1). http://www.jacmp.org/index.php/jacmp/article/view/3678.

Röntgen, W.C., 1898. Weitere Beobachtungen über die Eigenschaften der X-Strahlen. Ann. Phys. 300, 18–37. doi:10.1002/andp.18983000104

Sannita, W.G., Narici, L., Picozza, P., 2006. Positive visual phenomena in space: A scientific case and a safety issue in space travel. Vision Res. 46, 2159–2165. doi:10.1016/j.visres.2005.12.002

Schnapf, J.L., Baylor, D.A., 1987. How Photoreceptor Cells Respond to Light. Sci. Am. 256, 40–47. doi:10.1038/scientificamerican0487-40

Shortis, M.R., Robson, S., Beyer, H.A., 1998. Principal Point Behaviour and Calibration Parameter Models for Kodak DCS Cameras. Photogramm. Rec. 16, 165–186. doi:10.1111/0031-868X.00119

Smith, S.W., 2003. Digital Signal Processing: A Practical Guide for Engineers and Scientists. Newnes.

Spinelli, A.E., D'Ambrosio, D., Calderan, L., Marengo, M., Sbarbati, A., Boschi, F., 2010. Cerenkov radiation allows in vivo optical imaging of positron emitting radiotracers. Phys. Med. Biol. 55, 483–495. doi:10.1088/0031-9155/55/2/010

Spinelli, A.E., Ferdeghini, M., Cavedon, C., Zivelonghi, E., Calandrino, R., Fenzi, A., Sbarbati, A., Boschi, F., 2013. First human Cerenkography. J. Biomed. Opt. 18, 020502–020502. doi:10.1117/1.JBO.18.2.020502

Steidley, K.D., Eastman, R.M., Stabile, R.J., 1989. Observations of visual sensations produced by Cerenkov radiation from high-energy electrons. Int. J. Radiat. Oncol. 17, 685–690. doi:10.1016/0360-3016(89)90125-9

Suri, J.S., Acharya, R., Ng, E.Y.., 2008. Image Modeling of the Human Eye. 1st edn. Norwood MA: Artech House.

Taguchi, K., Frey, E.C., Wang, X., Iwanczyk, J.S., Barber, W.C., 2010. An analytical model of the effects of pulse pileup on the energy spectrum recorded by energy resolved photon counting x-ray detectors. Med. Phys. 37, 3957–3969. doi:10.1118/1.3429056

Tarasov, M.D., El'yash, S.L., Goncharova, V.F., Petrushin, O.N., Savel'ev, Y.A., Tarakanov, M.Y., Shigaev, Y.S., 2007. Efficiency of radioluminescence of water under the action of accelerated electrons. Instrum. Exp. Tech. 50, 761–763. doi:10.1134/S0020441207060085

Tearney, G.J., Brezinski, M.E., Southern, J.F., Bouma, B.E., Hee, M.R., Fujimoto, J.G., 1995. Determination of the refractive index of highly scattering human tissue by optical coherence tomography. Opt. Lett. 20, 2258–2260. doi:10.1364/OL.20.002258

Timmermann, B., Schuck, A., Niggli, F., Weiss, M., Lomax, A.J., Pedroni, E., Coray, A., Jermann, M., Rutz, H.P., Goitein, G., 2007. Spot-scanning proton therapy for malignant soft tissue tumors in childhood: First experiences at the Paul Scherrer Institute. Int. J. Radiat. Oncol. Biol. Phys. 67, 497–504. doi:10.1016/j.ijrobp.2006.08.053

Torrisi, L., 1998. Radiation damage in PVT (Polyvinyltoluene) induced by energetic ions. Radiat. Eff. Defects Solids 145, 271–284. doi:10.1080/10420159808223995

Torrisi, L., 2000. Plastic scintillator investigations for relative dosimetry in proton-therapy. Nucl. Instrum. Methods Phys. Res. Sect. B Beam Interact. Mater. At. 170, 523–530. doi:10.1016/S0168-583X(00)00237-8

Tromberg, B.J., Shah, N., Lanning, R., Cerussi, A., Espinoza, J., Pham, T., Svaasand, L., Butler, J., 2000. Non-Invasive In Vivo Characterization of Breast Tumors Using Photon Migration Spectroscopy. Neoplasia N. Y. N 2, 26–40.

Tuckwell, W., Bezak, E., 2007. Calculation of the positron distribution from ^{15}O nuclei formed in nuclear reactions in human tissue during proton therapy. Phys. Med. Biol. 52, 2483–2498. doi:10.1088/0031-9155/52/9/010

Vatnitsky, S., Moyers, M., Miller, D., Abell, G., Slater, J.M., Pedroni, E., Coray, A., Mazal, A., Newhauser, W., Jaekel, O., Heese, J., Fukumura, A., Futami, Y., Verhey, L., Daftari, I., Grusell, E., Molokanov, A., Bloch, C., 1999. Proton dosimetry intercomparison based on the ICRU report 59 protocol. Radiother. Oncol. 51, 273–279. doi:10.1016/S0167-8140(99)00060-2

Verhaegen, F., Seuntjens, J., 2003. Monte Carlo modelling of external radiotherapy photon beams. Phys. Med. Biol. 48, R107. doi:10.1088/0031-9155/48/21/R01

Vynckier, S., Derreumaux, S., Richard, F., Bol, A., Michel, C., Wambersie, A., 1993. Is it possible to verify directly a proton-treatment plan using positron emission tomography? Radiother. Oncol. J. Eur. Soc. Ther. Radiol. Oncol. 26, 275–277.

Wang, L.H., Jacques, S.L., Zheng, L.Q., 1995. MCML - Monte Carlo modeling of photon transport in multi-layered tissues. Computer Methods and Programs in Biomedicine 47, 131-146.

Willis B T M and Carlile C J 2009. Experimental Neutron Scattering, Oxford; New York: Oxford University Press.

Xu, Y., Wuu, C.-S., Maryanski, M.J., 2004. Performance of a commercial optical CT scanner and polymer gel dosimeters for 3-D dose verification. Med. Phys. 31, 3024. doi:10.1118/1.1803674

Zhang, R., Fox, C.J., Glaser, A.K., Pogue, B.W., Gladstone, D.J., 2013. Superficial dosimetry imaging of Čerenkov emission in electron beam radiotherapy of phantoms. Phys. Med. Biol. 58, 5477–5493. doi:10.1118/1.4770286

Zhu, X., España, S., Daartz, J., Liebsch, N., Ouyang, J., Paganetti, H., Bortfeld, T.R., El Fakhri, G., 2011. Monitoring proton radiation therapy with in-room PET imaging. Phys. Med. Biol. 56, 4041–4057. doi:10.1088/0031-9155/56/13/019